# X-ray-induced changes in optical properties of doped and undoped amorphous selenium

A Thesis

Submitted to the College of Graduate and Postdoctoral Studies

In Partial Fulfillment of the Requirements for the Degree of

Master of Science

In the Division of Biomedical Engineering

University of Saskatchewan

By

Yeon Hee Jung

Saskatoon, Saskatchewan

# PERMISSION TO USE

In presenting this thesis in partial fulfillment of the requirements for a Postgraduate degree from the University of Saskatchewan, I agree that the Libraries of this University may make it freely available for inspection. I further agree that permission for copying of this thesis in any manner, in while or in part, scholarly purpose may be granted by the professor or professors who supervised my thesis work or, in their absence, by the Chair of the Department or the Dean of the College in which my thesis work was done. It is understood that due recognition shall be given to me and to the University of Saskatchewan in any scholarly use which may be made of any material in my thesis.

Request for permission to Copy or to make other use of material in this thesis in whole or part should be addressed to:

Chair of the Division of Biomedical Engineering
57 Campus Drive
University of Saskatchewan
Saskatoon, Saskatchewan, S7N 5A9

OR

Dean
College of Graduate and Postdoctoral Studies
University of Saskatchewan
116 Thorvaldson Building, 110 Science Place
Saskatoon, Saskatchewan, S7N 5C9

# ABSTRACT

Amorphous selenium has been used as an important material for the flat-panel X-ray image detector. Its image quality is affected by a sensitivity which is reduced under high or long duration of X-ray exposure due to the generation of defects. Experiments were conducted to investigate the changes in optical properties of doped and undoped a-Se when the samples were exposed to two doses of X-rays, 900 Gy and 3200 Gy, at 30 and 70 kVp. The samples were: a-Se, a-Se:0.5% As, a-Se:6%As, a-Se:6% As and a-Se:6% As: ppm of Cs. After the cessation of X-ray irradiation, the recovery of the optical properties towards pre-exposure equilibrium values was also investigated. In addition, the dependence of optical properties on the temperature, alloying and doping have been studied. The transmission spectra $T(\lambda)$ of all films were scanned from 450 nm to 2000 nm, and the thickness $d$, wedge $\Delta d$, absorption coefficient $\alpha(\lambda)$, optical band gaps $Eg_T$, $Eg_U$ and refractive index $n(\lambda)$ were extracted from Swanepoel method from $T(\lambda)$.

The result shows that optical properties were influenced by the absorption of X-rays, heat and doping. The change in $n(\lambda)$ was related to densification by the Clausius-Mossotti equation. After the cessation of X-rays, the $n(\lambda)$ of the films relaxes back to the original state, after a certain amount of time. The minimum time to relax to the equilibrium state after irradiation takes about 16 hours. The maximum changes in $n(\lambda)$ and $d$ were 0.27% and −0.27%. The changes in the optical band gaps, $Eg_T$ and $Eg_U$, were within experimental errors ±0.04%. Changes in the optical constants induced by heating were measurably large. The changes in the optical constants by alloying with As and doping with ppm amounts of Cs have been also studied. Alloying with As increases $n(\lambda)$ and decreases $Eg_T$, and further doping of Cs slightly increases $n(\lambda)$.

# ACKNOWLEDGEMENTS

I would like to express appreciation towards my supervisor, Dr. S.O. Kasap, for his guidance, advices, leadership, patience and support. Without him, it would have been impossible for me to get into the right path for completing MSc. I also would like to thank Cyril Koughia, for his advices, helps for analysis of thin film transmission data. I also would like to thank Dr. George Belev, for sample preparation, for the excellent advices on experimental data, and for his patience and his insights to all my questions. I also would like to thank Analogic Canada Corp and University of Saskatchewan for financial support. I also would like to thank Farley Chicilo, Thomas Meyer, Ozan Gunes, and Jun-Yi Yang for their help on dose calculations and experimental set-up, on the experimental calculations, and instrumental problems. Finally, I would like to thank God, my family for their encouragement and full support during MSc.

# TABLE OF CONTENTS

# LIST OF FIGURES

# LIST OF TABLES

# LIST OF ABBREVIATIONS

| | |
|---|---|
| a-Se | amorphous selenium |
| AMA | active matrix arrays |
| FPD | flat panel detector |
| TFTs | thin film transistors |
| EHPs | electron-hole pairs |
| SFR | screen and film radiography |
| DOS | density of states |
| VAP | valence alternate pairs |
| IVAP | intimate valence alternate pairs |
| TOF | time of flight |
| NIR | near infrared |
| UV | ultraviolet |
| PPM | parts per million |
| NB | non-bonding |
| LP | lone pair |
| RMSE | Root mean square error |

# Chapter 1. Background

## 1.1. Introduction

Since Roentgen's discovery of X-rays in 1895, the X-ray imaging has been used as a medical diagnosis tool to image human body structures. There have been many scientific refinements in equipment and techniques in X-ray imaging over the years. Especially, the development of computers and filmless radiology introduced digital radiography in 1980s [1] where X-ray images are generated from a detector and directly recorded on a computer [2 and 3].

Digital radiography has evolved into different forms and one of the most recent and promising developments is the direct conversion flat-panel X-ray image detector (FPD) [3]. The direct conversion FPD is made by coating an X-ray photoconductor on top of a large area integrated circuit called an active-matrix-array (AMA). The AMA consist of millions of small pixels, each of which acts as a small detector to capture X-rays and convert them to charge directly [4]. The technology based on active-matrix flat-panels enables an efficient and effective method to generate an image. The FPD is the only detector today meeting a lot of requirements, such as active area, pixel size, image acquisition rate, and dynamic range for covering various applications, including general radiography, mammography, angiography and fluoroscopy [5].

The direct conversion FPD not only meets all the basic requirements for clinical use, such as cost, instant availability of the image, reduced dose, high sensitivity of X-rays [3], but also provides the highest image quality [2]. However, there are many unsolved problems and the one of problems is the lack of any information on damaging a-Se layers upon X-ray exposure. Ideally, a detector should not experience any changes in the material properties upon X-ray exposure [3]. Otherwise, its image resolution as well as image characteristics can be significantly affected. For instance, it is known that a high dose of X-rays decreases the X-ray sensitivity of

the photodetector, leading to a ghost of the previous image [6 and 7].

Therefore, we decided to study the X-ray induced optical properties of n-like a-Se layer in an a-Se detector. The current direct conversion FPD has used stabilized a-Se (0.2-0.5% As and doped with 0-20 ppm Chlorine) as an X-ray photoconductor [8]. The samples used in this study were: (a) pure a-Se, (b) a-Se: 0.5% As (c) a-Se: 6% As and (d) a-Se: 6% As doped with the 140 – 220 ppm of Cs. The photo-induced effects in a-Se has other applications in optoelectronic and photonic devices such as a grating and photoresist [24, 86].

Our research investigates the optical properties of doped and undoped a-Se under low and high doses of X-rays. We first studied if optical properties are influenced by other external stimuli or factors such as heat, thickness and doping. Then, we examined changes in optical properties for the different doping compositions of a-Se with low and high doses of X-rays. Finally, we examined changes in optical properties over time after completing X-ray irradiation to see if the properties relaxed to their original states. The objective of this research was to see if X-ray irradiation gives clear changes in the optical properties of a-Se.

A previous study showed that defects are generated during X-ray irradiation and these induced defects are annealed out over time [7]. So, we also tried to identify the X-ray induced defects upon X-ray irradiation and examined the changes over time after irradiation to see if x-ray effects are permanent or temporary. The optical properties of interests were the refractive index $n$, thickness $d$ and two optical band gaps $Eg_T$ and $Eg_U$.

## 1.2. Digital Radiography

In general, projection imaging is employed as a common X-ray imaging technique to obtain an image. This technique is based on projecting a shadow image of internal structures of the objects onto the detector [9]. In projection radiography, the procedure to obtain an image is divided into three steps: X-ray generation, attenuation of the beam and image creation, which is shown in Figure 1.1 below.

First, the special generator supplies a high-power voltage into an X-ray tube; the electrons flow from cathode to anode (i.e. tungsten target) inside the X-ray tube. The high energy electron undergoes an energy loss, which results in generating X-ray energy [10].

As X-rays pass through the patient, the variation in thickness, density or atomic composition of the different tissues causes variations in the transmission and absorption of the X-rays [11]. The dense tissues such as a bone absorbs most of X-ray beam and the soft tissues allow X-rays to penetrate relatively easier. The transmitted X-ray beams are captured by a detector and the absorbed X-rays are not captured [12]. The difference in penetration between two different mediums (i.e. two tissues) determines the X-ray contrast in the final X-ray image [9].

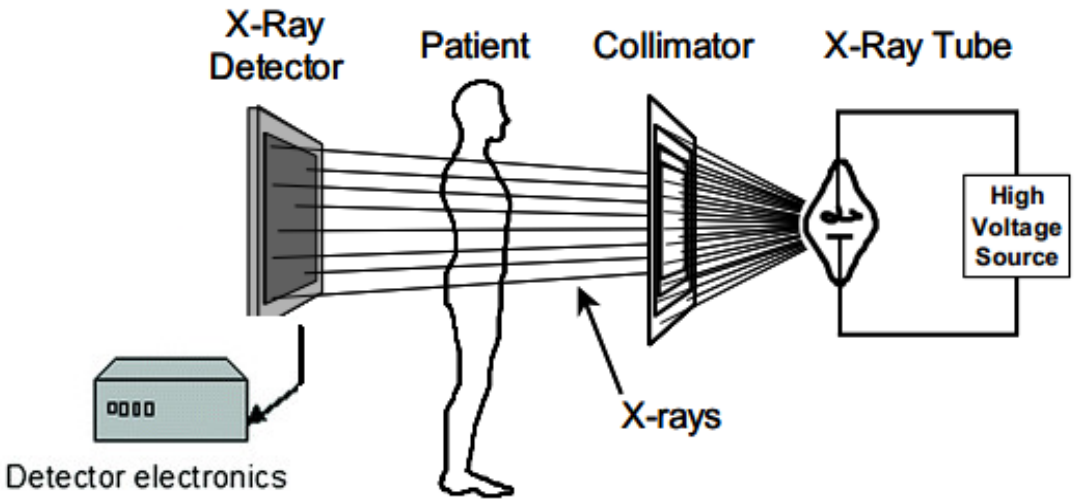


Figure 1.1. Schematic of radiography setup (from [13]).

The traditional method to obtain an X-ray image is to use a film in a close contact with a light-emitting screen. This method, so called screen and film radiography (SFR), suffers from a lot of disadvantages such as limited storage, high cost of film, film distribution, image processing, and high dose of X-rays (Fixed dose latitude). The image process in SFR is time-consuming and uses a chemical for the image development [1,2,3].

The digital radiography has replaced a lot of the disadvantages of SFR over the last thirty years [14]. First, the digital images can be expanded and shrunk in the greater details and manipulated without destroying the original, whereas in the SFR system, the images become permanent in the film once it has been processed. The manipulation of images is the great advantage for physicians who need to examine the structure and change the structure from normal to abnormal [16]. Secondly, the images are now stored in an electronic medium. This means that there is no risk of losing images and images are available at anywhere and anytime. Thirdly, it increases a dose efficiency from a larger dynamic range, which enables to reduce a high exposure to the patient [1,2].

One of the most successful developments was the FPD introduced in the end of the 1990s. The FPD integrates an electronic read out system based on AMA with an X-ray detection material (i.e. a photoconductor or phosphor) [14, 15]. This active matrix readout provides efficient and instant means to detect, store and measure the electrical charges [15]. By combining this readout with an X-ray detection material, the FPD is capable for capturing the X-ray image immediately after the exposure [3]. Its system eliminates the image creation step, the image plate reader step or the image development in the dark room, since the read out is essentially self-scanning in that no external means are required [1,3].

The FPD provides the highest spatial resolution with the best image quality and the fastest readout than with any other X-ray devices [2, 5]. The time lapse on displaying images after X-ray exposure is less than 10 seconds, allowing more patients to be examined in the same amount of time than with other radiographic devices [5]. The image generation is a real-time process [2].

## 1.3. Direct conversion flat-panel X-ray image detector

There are two types of flat-panel X-ray detectors depending on detection (conversion) types. The direct conversion uses an X-ray photoconductor (i.e. a-Se) which converts X-ray photons directly into electrical charges. The indirect conversion uses a scintillator (i.e. CsI) to convert X-rays into visible light, which in turn is converted into an electrical charge by means of an a-Si photodiode arrays [14]. Both the direct conversion and indirect conversion detectors incorporate the active matrix readout (AMA) in which each pixel element contains a sensing and storage element, a switching element (photodiode and TFT), and image processing module to detect, store and read the charges [15].

Figure 1.2 below shows a cross-sectional structure of two pixels (*i, j*) and (*i, j*+1) with TFTs for the direct-conversion flat-panel X-ray imager. Each pixel element in the AMA acts as an individual detector to detect X-rays and convert it to an amount of charge $\Delta Q$ proportional to the amount of incident X-rays. These charges are carried by a corresponding pixel capacitor $C_{ij}$ at (*i, j*) to store and then read out, when the TFT switches are on. The external electronics control the state (on and off) of TFTs switches [3, 4, 8].

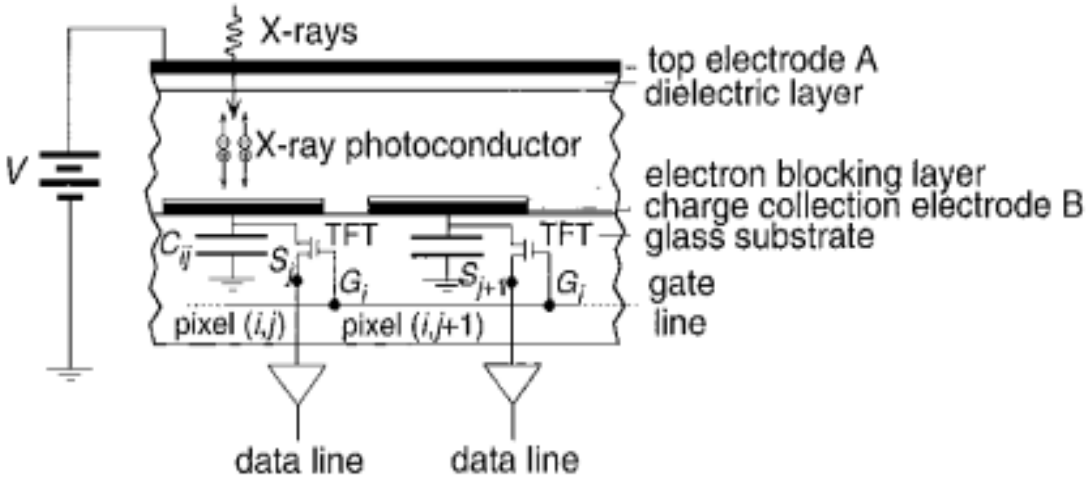


Figure 1.2. A cross sectional view of two pixels with each of TFTs, storage capacitances $C_{ij}$ and EHPs. The top electrode A is a vacuum coated metal and the bottom electrode B is the pixel charge collection electrode. There is a thin dielectric layer between the a-Se and the top electrode A and there is a doped a-Se alloy which is coated between the pixel electrode B and a-Se photoconductor to reduce the injection of electrons, and hence the dark current (from [3]).

The charges can be read by properly coordinating the gate line *i* and data line *j* of the TFT (*i, j*). The gates of all the TFTs in each row *i* and data of all TFTs in each column *j* are connected by the same gate line *i* and same data line *j*, each respectively as shown in Figure 1.3. The read-out is started when the TFT is switched on via the gate line *i* [5]. When gate line *i* is activated, then *N* data lines from the first column *j* = 1 to the last column *j* = *N* read the charges on the pixel electrode in row i. The charges are read out row by row, multiplexing the parallel columns to a series of digital signal and then sent into a computer for image. Then, the next row, next gate line *i* + 1, is activated and the same *N* data lines read the charges in row *i* +1. The whole steps are repeated until the whole matrix has been read from the first row *i* = 1 to the last row *i* = *N*. This mechanism is based on self- scanning [3].

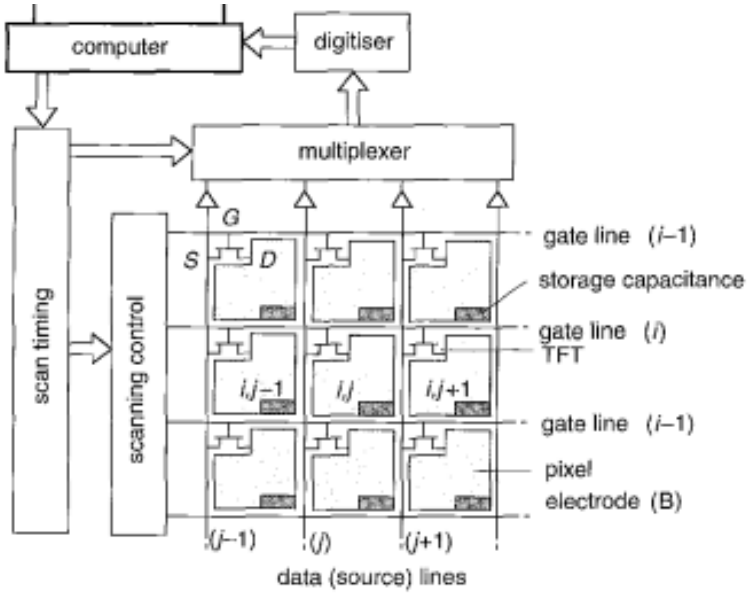


Figure 1.3. A cross sectional view of thin film transistor (TFT) layer active matrix area (AMA). The label "S" refers data (column) line, and the subscript "G" refers gate (row) line (from [3]).

## 1.4. The X-ray photoconductor requirements

The selection of the photoconductive material in the detector is critical because it greatly affects the detector performance [17]. The most important factor for X-ray photoconductors is the X-ray sensitivity. The X-ray sensitivity, which is the amount of charges collected from absorbing radiation, is controlled by three major quantities: i) the X-ray absorption, which relies on the attenuated fraction of photons $\eta_Q = [1-\exp(-\alpha L)]$, with a linear attenuation coefficient $\alpha$ with the large thickness $L$ of the photoconductor, ii) the number of charge carrier generation, which relies on the amount of photo-generated charges $\Delta Q = e\Delta E/W_{\pm}$ from the absorbed radiation of energy $\Delta E$ with $W_{\pm}$ is ionization energy of EHPs and, iii) a collection efficiency of the charge carriers [3, 4 and 5]. Above all, the ideal photoconductor should have the following material properties,

a. The photoconductor should have high intrinsic X-ray sensitivity. That means that it should have high X-ray absorption with a high absorption coefficient $\alpha$ with the large thickness $L$ of the photoconductor. Furthermore, the penetration depth $1/\alpha$ should be less than the thickness $L$, that is $1/\alpha << L$. It is because all incident X-ray radiation should be absorbed within the thickness of a detector to avoid the unnecessary exposure to patients.
b. There should be no deep trapping of EHPs, which means that the charge carrier schubweg, the distance a carrier drifts before it is trapped and becomes unavailable, $\mu\tau F$, should be greater than the thickness of detector $L$, that is $L<<\mu\tau F$. where $\mu$ is a drift mobility, $\tau$ is deep trapping time and $F$ is electric field.
c. There should be no recombination of electrons and holes.
d. The photoconductor should be coated onto the AMA panel easily (i.e. conventional vacuum deposition) over large area with uniform quality [18]. The detector needs to be larger than the body part to be imaged.
e. All the properties (a-e) above should not change with time or due to repeated and long x-ray exposure [8].

Although a high quantum efficiency requires the large thickness of the detector, the detector thickness $L$ is limited to schubweg and X-ray penetration depth, that is, $1/\alpha << L<< \mu\tau F$ from factor a and b.

## 1.5. Amorphous selenium as an X-ray photoconductor

The ideal candidate should satisfy all the requirements from a to g, and there are $PbI_2$, PbO, CdTe and $HgI_2$ with good absorption characteristics. However, these involve the small areas which are not suitable as an X-ray photoconductor [5, 18]. The a-Se seems the best candidate since it i) is easily deposited into active matrix area readout circuit and is coated over large areas (i.e. 40 cm × 40 cm or larger), ii) has an acceptable x-ray absorption coefficient, iii) it has good charge transport properties for both holes and electrons, iv) has low dark current [3] and v) has a high intrinsic spatial resolution [14].

a-Se has the inherent ability to generate charge carriers under exposure [19]. It was Willoughby Smith, who discovered the photoconductivity ability of selenium by testing a resistance of sub-marine telegraphic cables under light [8]. Since then, it has been used as a photocell, solar cell and electrical rectifier [19]. The amorphous form of selenium was used in xeroradiographic photoreceptor, then it has been replaced by FPD by replacing its toner with electronic readout [8].

The stabilized amorphous selenium (a-Se alloyed 0.3-0.5% As and doped with the ppm level of chlorine) is currently used as direct conversion FPD. The pure amorphous selenium crystallizes over time, which results in a higher dark conductivity. Hence, a small portion of As is added in a-Se to retard the crystallization rate and to increase viscosity. The As atoms (valency of three) in the structure are triply bonded [20], and linked to three free chain ends, which lead to a decrease in the number of free chain ends [21]. However, a high concentration of As introduces deep hole traps and shortens the hole range, which result in reducing the photoconductivity of a-Se. This can be compensated by doping halogen (i.e. Cl), which restores loss of hole transport [20]. Table 1.1 summarizes all important properties of the stabilized a-Se and Figure 1.4 shows the image of a hand generated by using a stabilized a-Se photoconductor.

Table 1. 1. Selected properties of stabilized a-Se for the x-ray layers for use as X-ray photoconductors (from [17]).

| Property | a-Se (0.2–0.5% As + 10–40 ppm Cl) |
|---|---|
| $E_g$ (eV) | 2.25 |
| $W_{\pm}$ (eV) | Depends on the field as $W \approx W_{\pm}^{o} + B/F$ where $B = 4.4 \times 10^6$ eV V cm$^{-1}$<br>6 eV at $F = \infty$ |
| Hole drift mobility | 0.12 cm$^2$ V$^{-1}$ s$^{-1}$ |
| Electron drift mobility | 0.003–0.006 cm$^2$ V$^{-1}$ s$^{-1}$; 0.003 cm$^2$ V$^{-1}$ s$^{-1}$ used |
| Hole lifetime | 1–500 $\mu$s. Varies with the source of Se, and depends on the substrate temperature |
| Electron lifetime | 1–1000 $\mu$s. Varies with the source of Se and depends on impurities. No significant dependence on the substrate temperature |

Figure 1.4. The image of a hand from a direct-conversion flat-panel X-ray image detector using a stabilized a-Se photoconductor (from [8]).

# Chapter 2. Properties of Amorphous Selenium

Since the development of the modern band theory in crystalline solids, amorphous solids had not been considered as a true semiconductor for many years. The early physicists proved it difficult to find the similar features in amorphous solids due to lack a long-range order. However, amorphous solids are semiconductors which possess a comparable band structure [32]. Although the short-range order in amorphous solids invalidates Bloch theorem to derive the band structure [18], it can still be derived from a similarity to crystalline band diagram and with a careful experimental observation.

## 2.1. Atomic structure of amorphous solids

In crystalline solids, the atoms are arranged in the exact same manner on a periodic lattice. This means that the same number of neighbors, same bond lengths and same bond angles exist throughout the entire network. As a result, the crystalline structure has a very high degree of symmetry, which means that the atoms in any position is exactly same as shown in Figure 2.1a. This results in a long-range order [32 and 33].

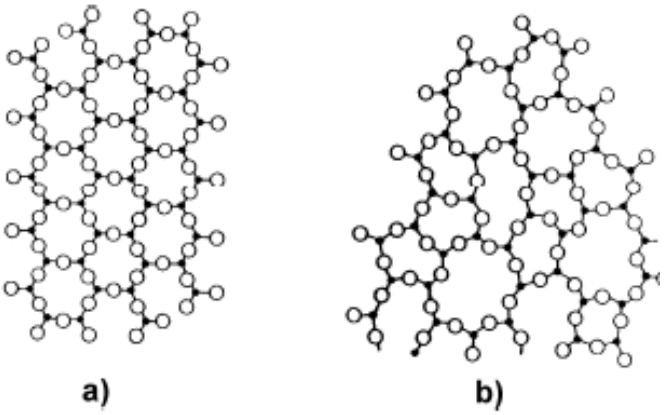


Figure 2. 1. Crystalline and amorphous structures in a hypothetical two-dimension (a) crystal of As2Se3 (b) The amorphous form of the same compound of As2Se3 cooled from the melt. The black dot is selenium atom and the white dot is arsenic atom (from [33]).

In amorphous solids, however, atoms are arranged in a broken symmetry and periodicity. Figure 2.1 (b) shows a schematic diagram of amorphous form of the $As_2Se_3$, formed by quenching from the liquid. Since the structure is not equivalent, the energy required to break and form the bond in an atom is distinct to each other. There are also variations in bond angles from atom to atom, which result in loss of periodicity and hence, losing a long-range order. This arrangement is known as a short-range order. The important point is that the presence and absence of periodicity and symmetry distinguish crystalline solids from amorphous solids [32 and 33].

## 2.2. Band theory of amorphous solids

When the atoms are brought together to form a solid, the atomic energy level is split into finely separated molecular energy levels to form a continuum, an energy band. The band theory derives these energy bands with an available energy level by applying the allowed quantum mechanical wave functions for an electron in a solid, and the density of states (DOS) $g(E)$ is used to express the number of states available per unit energy per unit volume.

In a crystalline solid, the periodic atomic arrangement results in periodic potential energy of electrons. Solving for the Schrondinger equation with the periodicity of potential energy leads to the Bloch wave and the allowed energy levels. These energies are arranged in conduction or valence bands. There are also energy ranges for which there are no Bloch wavefunctions, and hence no allowed energies from valence band to conduction band, a band gap [32]. As a result, there are well-defined conduction and valence bands which are separated by an energy gap in a crystalline solid, as shown in Figure 2.2. Between a band and a band gap, there is a sharp band edge where the DOS drops to near zero [34].

In an amorphous solid, the loss of translational periodicity does not allow to use the Bloch theorem. However, an amorphous solid still possesses an energy band with a mobility gap, and it turns out that electronic properties are similar from crystalline properties, since the band structure is generally determined by a short-range order [35]. Nevertheless, amorphous solids have slight variations in its DOS diagram resulting from the loss of the periodicity of the equivalent crystalline structure, which is shown in Figure 2.2b and 2.2c.

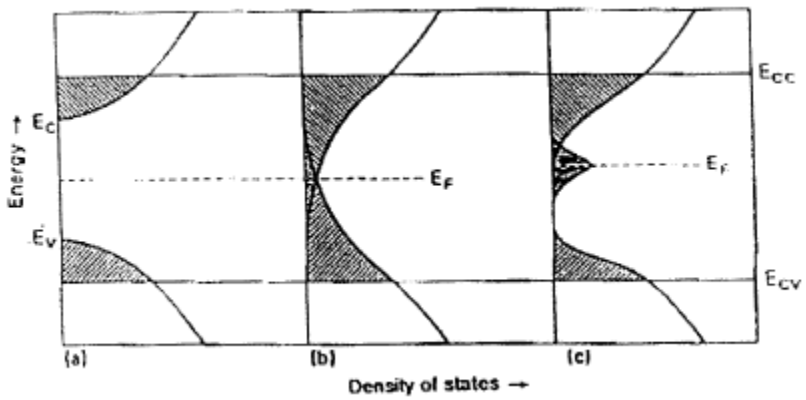


Figure 2. 2. The density of states of (a) a crystalline semiconductor (b) and (c) an amorphous semiconductor. (b) Introducing fluctuations in the bond length and angle from crystalline semiconductor (c) introducing chemical defects from (b) (from [36]).

First, the sharp band edges in a crystalline solid in figure 2.2a become smeared or broadened. This broadened state begins at the band edges $E_{cc}$ and $E_{cv}$ and extends into the forbidden gap in figure 2.2b. The wavefunction between valence band edge $E_{cv}$ and conduction band edge $E_{cc}$ forms localized states where its probability of finding the electron is "localized" at certain spatial locations. Since its electrons are trapped or confined in this localized region, this state is also known as a trap or tail state. This state arises from the deviations in bond angles and bond lengths [32, 34 and 35].

Secondly, the traps in the localized states in Figure 2.2c are attributed to the specific defects of the amorphous semiconductors [21]. These are coordination defects (valence alternate pairs), dangling bonds or dopants [32].

In addition, there is a band edge, which separates extended states from localized states, known as a mobility edge, which is $E_{cc}$ and $E_{cv}$ in Figure 2.2b and 2.2c. The name mobility edge derives from the change in the mobility of charge carriers across $E_{cc}$ or $E_{cv}$. The electrons are mobile at zero temperature in the extended states and immobile within the localized states at zero degree. The region of zero mobility leads to the concept of the mobility gap, which is energy from valence band $E_{cv}$ to conduction band mobility edges $E_{cc}$, which can be considered as a band gap in amorphous solids [14, 32].

## 2.3 Physical structure of amorphous selenium

Crystalline selenium has two types of allotropes: $\alpha$-monoclinic Se ($\alpha$-Se) and trigonal Se ($\gamma$-Se). In trigonal Se, all phases of dihedral angle are either positive (++++) or negative (---), promoting to a local helicity, whereas the phases are alternating (+-+-+-+-+-) in $\alpha$-monoclinic Se, promoting to a ring-like structure [38]. The dihedral angle is defined as the angle between the adjacent bonding planes [41].

The amorphous structure of selenium follows a random chain model, in which the two-fold coordinated atoms have the same magnitude of dihedral angle, with changing its sign in random. A random variation in phase means that a-Se consists of disordered mixture of chain fragments from $\gamma$–Se chains and ring fragments from $\alpha$–Se rings [37]. The phase of a-Se in Figure 2.3 is expressed by + + + – + – + – – –, where the front +++ and the back --- regions are chain segments which possess a helical character, and the middle -+-+ region is the ring segment. This is a chain-like structure which loses a regular helical character, and it can bend, twist, turn, or "meander" through it [38]. The evidence for the alternation of dihedral angle in phase with the ring- and chain-fragments was already proven from Raman scattering [39].

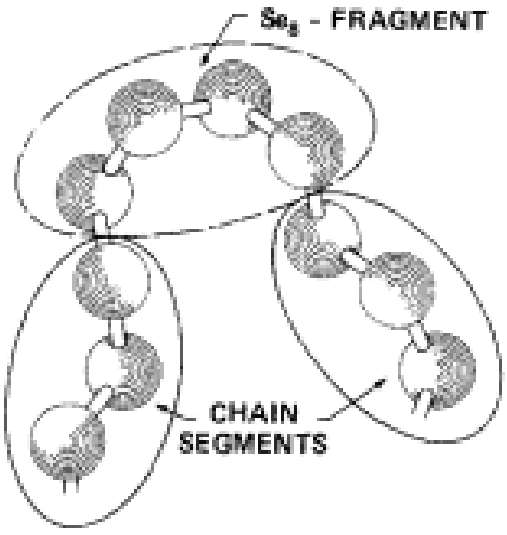


Figure 2. 3. Random chain model of amorphous selenium (from [39]).

There are potentially six types of bonding configurations in selenium. The $Se_2^0$ configuration is the lowest, most stable energy configuration, which is involved in normal bonding. There are

also a pair of charged defects, known as valence alternation pairs, which are a negatively charged selenium atom with a single valence, $Se_1^-$, and a positively charged selenium atom with a triple valence, $Se_3^+$. These defects, $Se_3^+$ and $Se_1^-$, are intrinsic defects in thermal equilibrium, free-energy derived equilibrium [21], since the formation energies of a VAP ($Se_3^+ + Se_1^-$) and the atom in the $Se_2^0$ state are estimated to be $-4E_b + U_{LP}$ and $-2E_b$, respectively, according to Kastner model [40]. This means that the VAP is more stable state than the $Se_2^0$ state, hence favourable to form. The concentration of VAP was found out to be $10^{16}$ $cm^{-3}$ in Electron spin resonance measurement [40].

If the atom in the $Se_1^-$ and $Se_3^+$ states retains one hole and one electron respectively, then these form the neutral, excited $Se_1^0$ and $Se_3^0$ states. These $Se_3^0$ and $Se_1^0$ states are in non-equilibrium that return to the original $Se_3^+$ and $Se_1^-$ states by releasing retained charged carriers, which are unstable [21]. In Figure 2.4 below, the formation energies of $Se_3^0$ and $Se_1^0$ are $-2E_b + \Delta$ and $-E_b$, respectively, which both are higher than that of the $Se_2^0$ state, $-2E_b$, hence more unstable.

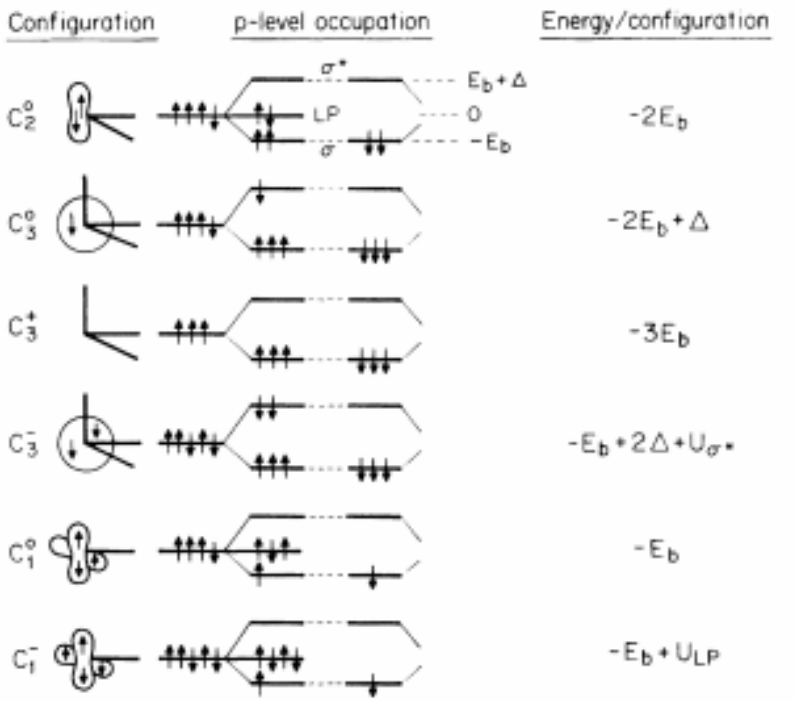


Figure 2. 4. The structure and p-level energy of bonding configurations for selenium atom (C refers to Se). Straight line represents bonding orbitals, a lobe represents a lone-pair orbital, and a circle represents an anti-bonding orbital. The energy level consists of the three states from the top: $\sigma*$, lone-pair electron, and $\sigma$ states. Energies are given as zero for LP energy (from [40]).

The $Se_2^0$ has $4s^2\ 4p^4$ valence electron configurations with two valence electrons in s-state and four electrons in p-state. The two electrons in p-state form two covalent bonding orbitals with neighbor atoms and the four remaining electrons in s- and p-states form two lone-pairs orbitals. The bonding orbitals form strong covalent bonds, whereas the two lone pair orbitals are electronically attracted to the cores of atoms in neighbors, forming van der Waals bonds [41]. The van der Waals bonds interact with neighbor atoms of the solid through lone pair electrons, holding the Se chains in a solid. The van der Waals play an important role in stabilizing the chain structure.

In the amorphous structure, the lone pairs of atoms are disoriented which is enough to cause tension between chains. The tension is so strong that it destabilizes the interactions between chains. To reduce (release) chain tension, chain breaking occurs in the structure, forming the defects, $Se_3^+$ and $Se_1^-$ [42, 45]. The $Se_3^+$ and $Se_1^-$ defects correspond to the branch points and the chain ends of the structure respectively. If $Se_1^-$ and $Se_3^+$ are separated by many atomic spacings, then this pair of defect is called a valence alternate pair, VAP, and if they belong to a single same chain and are close in proximity, these are called an intimate valence alternate pair, IVAP, as shown in Figure 2.5 below.

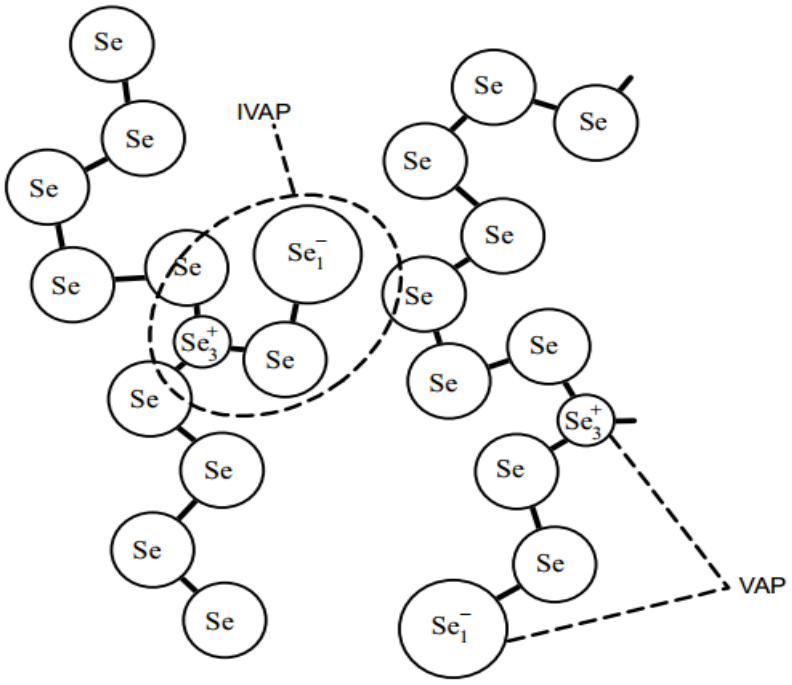


Figure 2. 5. Schematic diagram of VAP and IVAP (from [43]).

## 2.4. Density of states of amorphous selenium

The original DOS function for a-Se was first proposed by Abkowitz in 1988 [44], derived from the measurements of xerographic cycled-up residual voltage decay and xerographic dark discharge. The charge carriers in the extended states in Figure 2.6 can drift in and out of the extended states and trap in the localized states for a while, due to thermal vibrations of atoms [32]. If they drift near the band edge, these are called shallow traps, and if drift in the mid-gap, these are called deep traps. The shallow traps reduce the drift mobility, whereas the deep traps prevent the charge carriers from crossing (drifting) out. Hence, in the Abkowitz DOS diagram, the shallow traps (not deep traps) control the drift mobilities of electrons and holes [20]. The DOS diagram in Figure 2.6 has the broad tail distribution from extended states to the mid-gap with the shallow hole and electron traps at 0.28 eV above $E_v$ and at 0.35 eV below $E_c$ [44]. The cause seems to be related to structural defects (i.e. variations in the bond angles, lengths or phase of dihedral angles) [32].

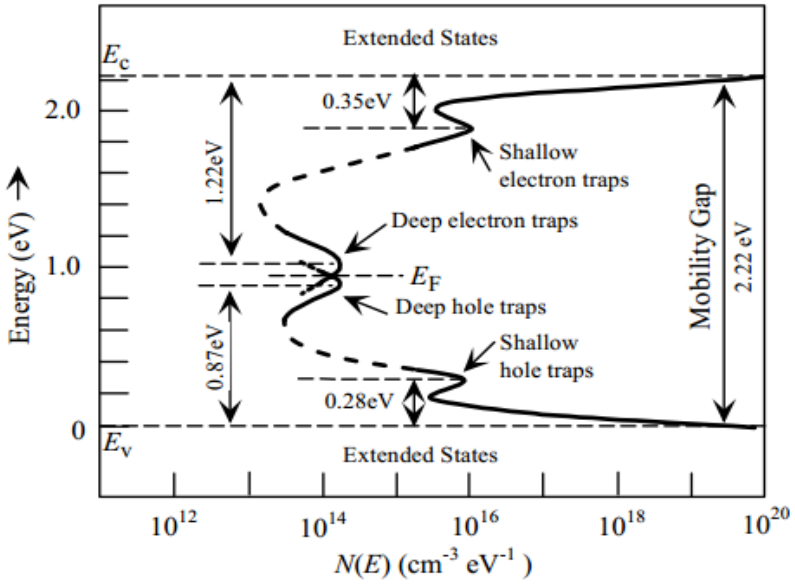


Figure 2. 6. The original DOS distribution of a-Se based on Abkowitz (from Abkowitz [44]).

Recently, Koughia [42] developed the new DOS model for a-Se, from the measurement on the interrupted field time of flight (IFTOF). In this model, the electron and hole traps are attributed to the VAP defects, $Se_3^+$ and $Se_1^-$ of a-Se, respectively [21]. The $Se_3^+$ and $Se_1^-$ defects serve as the charged trap centers of the DOS diagram.

This DOS has some features as follows: i) certain peaks occur in the conduction band localized states. It turns out that there are at least three different types of VAPs which are responsible for the various charged trap centers of the DOS, which is shown in the left diagram in Figure 2.7, and ii) there is a continuously and exponentially decreasing DOS shape from the valence band extended state, unlike the conduction band, which is shown in the right diagram in Figure 2.7. This implies that the tail of the valence band is stronger than that of the conduction band, hiding the small peaks associated with $Se_1^-$ charged trap centers [42].

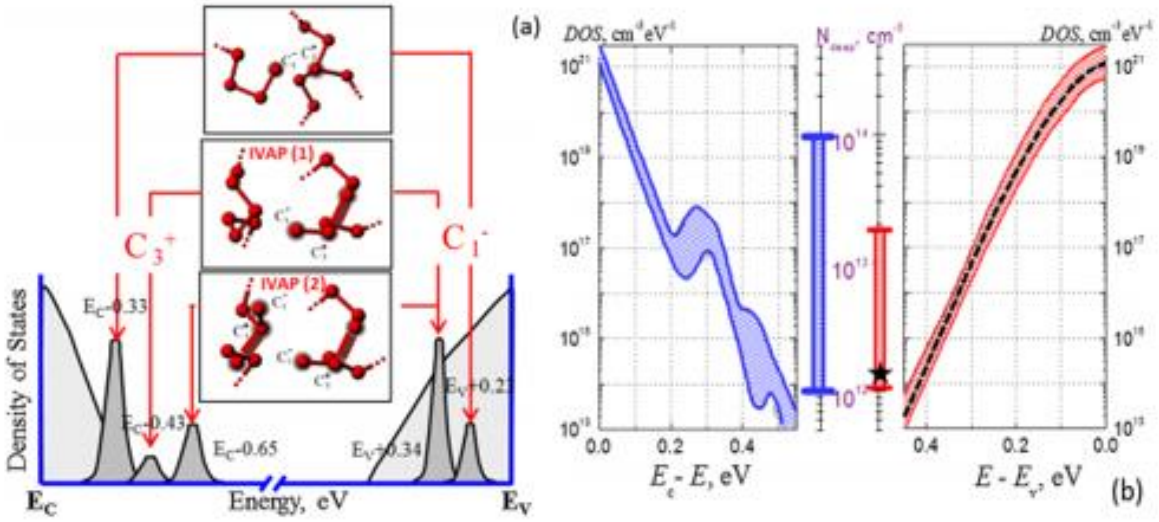


Figure 2. 7. The DOS distribution of a-Se based on reference (from [42]).

Also, the DOS distribution can be influenced by various phenomena such as doping, alloying, aging, annealing, temperature or X-rays. The concentration of deep and shallow traps in the DOS are shifted by introducing dopants (i.e. Cl in ppm), alloying elements (i.e. As) and aging and annealing [37]. In addition, it was recently found out that X-ray irradiation changes the electron lifetime, increasing the concentration of deep traps [7]. This implies that the DOS distribution a-Se is not fixed, but is rather flexible to change from the preparation, external environment or external stimuli (i.e. heat and light) [18].

The important point is that the DOS function is the main figure which determines the optical and electrical properties. In other words, when doping, heat, or X-ray exposure changes the shape of the DOS distribution, it would also influence the optical and electrical properties as well. There is a correlation between one another, since the optical constants are originally derived from the

DOS function in mathematical functions [18].

## 2.5 Optical properties of amorphous selenium

Numerous optoelectronic devices such as photodetectors or photovoltaic devices require a fundamental knowledge of optical constants, since its behavior of performance can be predicted by its optical constants [46,47] (i.e. holography [24]). The two most important optical constants are the refractive index $n$ and absorption coefficient $\alpha$. The optical properties of a material are closely related to the changes which light undergoes upon interacting with the medium [48].

The absorption coefficient $\alpha$ describes how easily the photon energy can be absorbed through the medium. Refractive index $n$ describes how easily light can propagate through a medium, which is affected by the electronic polarizability of medium, local field inside medium or density [48]. The refractive index, in general, is usually expressed by complex quantity: $N = n + iK$, where $n$ is the real part of the refractive index and $K$ is the imaginary part known as the extinction coefficient. These absorption coefficient $\alpha$ and extinction coefficient $K$ are related by $K = \lambda\alpha/4\pi$ [49].

### 2.5.1 Optical Absorption

Amorphous semiconductors possess an optical gap and absorption edge, similar from its counterpart crystal. There are, however, important distinctions to be acknowledged. First, the sharp absorption edge in the crystalline phase is broadened out in the amorphous phase, which arises from the broadened or smeared the DOS tail states. In addition, the wave vector "$k$" which used to describe an optical transition (i.e. direct and indirect) in crystalline semiconductors, is not used in amorphous semiconductor, implying that there is no direct and indirect transition [50].

In crystalline semiconductors, light is absorbed whenever electrons are excited across the band gap. The optical transition for exciting charge carriers into the conduction band is very sharp, so the threshold wavelength for the onset of optical absorption is well-defined. In amorphous semiconductors, however, it is difficult to determine such a threshold wavelength, since the absorption edge is broadened out. There is fuzziness in the bandgap in localized states which arises from variations in bond angles and lengths [34]. Because of that, the charge carriers are

now excited across the mobility gap in several different paths as shown in Figure 2.8.

There are three different optical transitions in Figure 2.8 which are connected to the three optical absorption regions (A, B and C) in the absorption spectra in Figure 2.9. First, the optical transition from VB extended state to CB extended states (blue line) in figure 2.8 is the fundamental absorption, region A in figure 2.9. Also, the transition from VB localized to CB extended states or vice versa (green line) in figure 2.8 is the Urbach edge region, region B in figure 2.9. Lastly, the transition from VB localized to CB localized state (red line) in figure 2.8 is the Urbach tail, region C in figure 2.9. The regions A, B and C are high absorption region, moderate absorption region and weak absorption tail, respectively. The absorption coefficient in region A follows Tauc's relation and region B follows the Urbach rule [51].

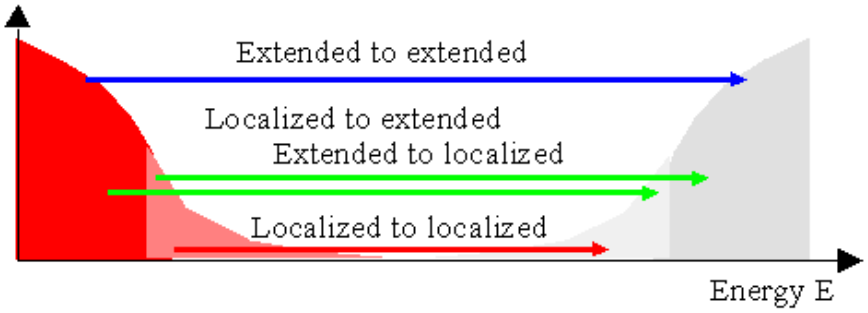


Figure 2. 8. The optical transitions in amorphous semiconductor (after [49]).

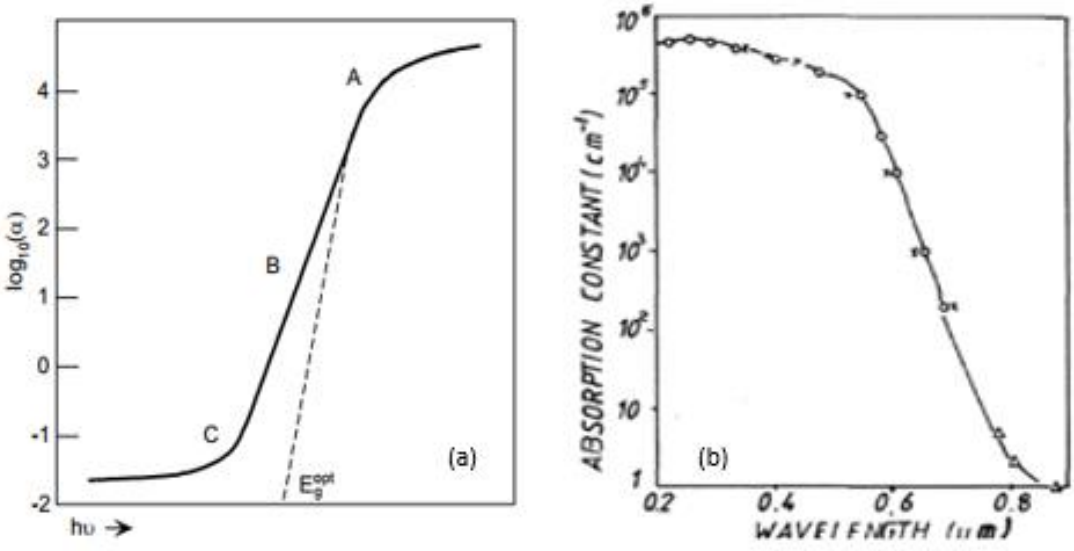


Figure 2. 9. (a) The optical absorption coefficient as function of photon energy for typical amorphous semiconductor (after [43]) and (b) The optical absorption characteristics for a-Se (after [21]).

### 2.5.1.1Tauc gap

The high absorption region A in Figure 2.9a follows a linear Tauc relationship between the absorption coefficient ($\alpha$) and photon energy ($\hbar\omega$). The description below derives a relation between $\alpha$ and $\hbar\omega$, which derives from Nessa et al [50 and 52].

The optical absorption coefficient is defined as, according to Mott and Davis [53],

$$\alpha(\omega) = B \int \frac{N_c(E)N_v(E-\hbar\omega)dE}{\hbar\omega} \tag{2.1}$$

where $N_c(E)$ and $N_v(E)$ are the DOS of conduction and valence bands which are defined,

$$N_c(E) = \text{constant}(E - E_c)^a \tag{2.1a}$$

$$N_v(E) = \text{constant}(E - E_v)^b \tag{2.1b}$$

Substituting equations (2.1a) and (2.1b) into equation (2.1) and after integrating over all energy states in the $N_c(E)$ and $N_v(E)$ yield an equation (2.2) below.

$$[\alpha\hbar\omega]^n = B'^{1/n}(\hbar\omega - E_o) \tag{2.2}$$

$$\frac{1}{n} = a + b + 1 \tag{2.2a}$$

where $B$ is a transition matrix element [51]. Let us suppose that $N_c(E)$ and $N_v(E)$ are forms of a parabolic curve [52]. With $n$ = ½ then, equation (2.2) results in,

$$[\alpha\hbar\omega]^{1/2} = B(\hbar\omega - E_o) \tag{2.3}$$

which is known as the *Tauc relation*.

Many amorphous semiconductors including $As_2S(Se)_3$ follow the Tauc relation when $n$ = ½ [54]. The plot of $\sqrt{\alpha\hbar\omega}$ versus $\hbar\omega$ leads a straight line whose intersection with the X-axis results in the energy gap $E_o$, which is known as the *Tauc optical gap*. This plot is known as *Tauc's plot* and the proportionality constant $B$ is known as *Tauc's constant*. The Tauc optical gap and Tauc constant are determined by experiments [51]. However, there is a deviation from equation (2.3) in terms of exponent $n$. Experiments from [54] have shown that exponent $n$ = 1 for amorphous selenium, which α follows a linear dependence on energy as follow,

$$[\alpha\hbar\omega] = B(\hbar\omega - E_o) \tag{2.4}$$

### 2.5.1.2 Urbach edge

In region B (Urbach edge) in Figure 2.9, the absorption coefficient $\alpha$ has an exponential dependence on photon energy, which arises from the exponential band tail states in the amorphous DOS distribution [51 and 54].

The Urbach edge in photon energy just below the optical gap ($\alpha < 10^4$ cm$^{-1}$) is given by

$$\alpha \propto \exp(\frac{\hbar\omega}{\Delta E}) \tag{2.5}$$

where $\Delta E$ is the Urbach energy characterizing the slope of the curve. The energy value at which the absorption coefficient $\alpha$ reaches $10^4$ cm$^{-1}$ is known as the Urbach band gap, $Eg_U$. The exact cause for the Urbach edge is unclear, but it seems that $\Delta E$ has to do with the width of VB or CB tail states [51] or is affected by temperature, since $\alpha \propto \exp(\frac{\hbar\omega}{kT})$. The $\Delta E$ has a positive temperature dependence in many chalcogenide glasses [54]. Figure 2.10 shows that $\Delta E$ increases from 0.05 eV and 0.06 eV, whereas $Eg_T$ decreases from 2.1 eV to 1.95 eV when temperature drops from 76 K to 300 K, and Figure 2.11 shows the $Eg_T$ decreases and $\Delta E$ increases at the same temperature axis, from 0 K to 1000 K.

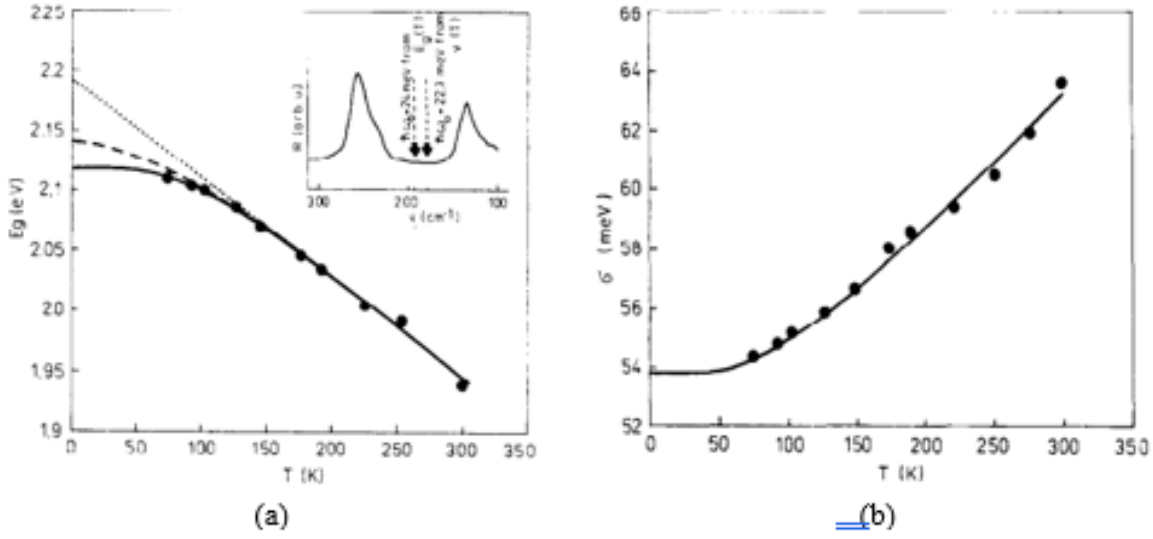


Figure 2. 10. Tempreature dependence on (a) Tauc band gap EgT and (b) Urbach energy Egu for amorphous selenium (after Ticky [55]).

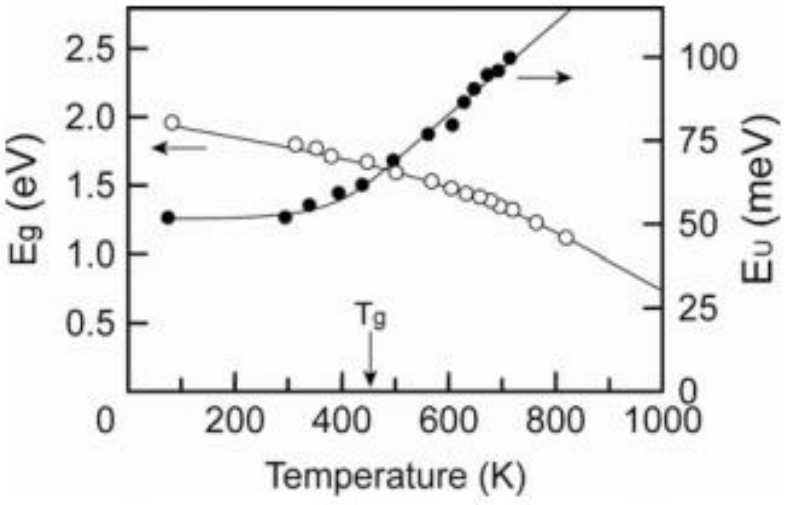


Figure 2. 11. Temperature dependence on Tauc band-gap Eg and Urbach energy Eu for As2Se3 (after [54]).

### 2.5.1.3 Weak absorption tail

Part C in Figure 2.9 represents the low absorption region in which absorption is governed by the optical transition from tail to tail state. This region usually has a small absorption coefficient $\alpha$ below 1 $cm^{-1}$, known as a weak absorption tail. Due to this very low absorption coefficient, it is difficult to discern between a true experimental measurement and noise associated with signal [54].

However, it is possible to distinguish the weak absorption tail by using sensible experimental technique (i.e. photothermal deflection spectroscopy) and study from it, things such as composition or impurity dependence. Figure 2.12 below shows the dependence of the weak absorption tail of the pure $As_2S_3$ upon the addition of different Fe concentrations. This figure shows that a high concentration of Fe increases the tail absorption [54]. Tanaka [54] suspected that the impurity could arise this absorption tails. However, it is possible that this state is more related to the density of defects, since localized tail states are generated from intrinsic structural disorders [51].

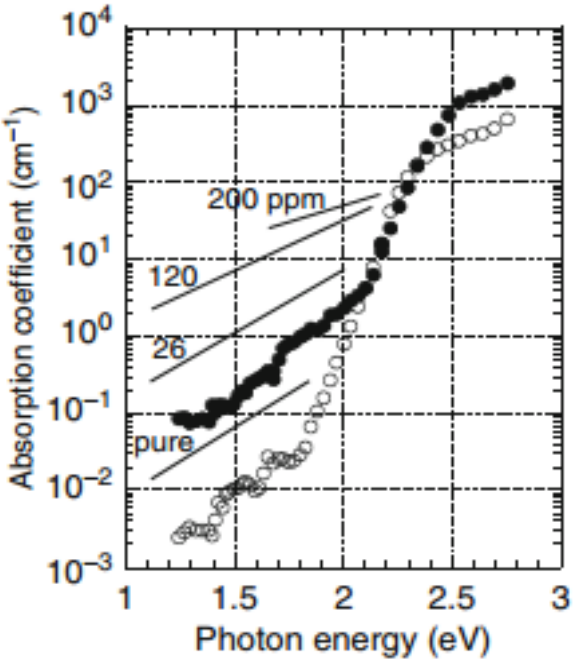


Figure 2. 12. Absorption spectra of As2S3 in a bulk sample (open circle) and as-evaporated film (solid circle) with weak absorption tails of different Fe concentration (pure, 26 ppm, 120 ppm and 220 ppm) (after Tanaka [56]).

### 2.5.2. Refractive index

The refractive index of the material is [32],

$$n = \frac{c}{v} \tag{2.6}$$

where *refractive index n* is the ratio of the speed of light in vacuum *c* to its speed in a medium *v*. Since the wave travels through a medium, the oscillating electromagnetic field polarizes the molecules. The refractive index *n* measures the ease with which the medium becomes polarized. The polarization slows down the propagation of the wave, which is the reason why *n* is always greater than one in the medium. The denser the medium is, the stronger the interaction between the field and the dipoles becomes, and then light propagates more slowly in the medium with a high refractive index. The polarization effect is represented by the refractive index *n* (relative permittivity $\varepsilon_r$) of a material [32].

$$n = \frac{c}{v} = \sqrt{\varepsilon_r} \tag{2.7}$$

Light propagation in absorbing materials is expressed by a complex relative permittivity in which the imaginary part represents the losses. Losses occur as a result of absorption by the interaction of electromagnetic waves with lattice vibrations (phonons), photo-generative absorption (creation of electron-hole pairs), and free carrier absorption. The relative permittivity is written as,

$$\varepsilon_r = \varepsilon_r' - i\varepsilon_r'' \tag{2.8}$$

where $\varepsilon_r'$ and $\varepsilon_r''$ are the real and imaginary parts of relative permittivity $\varepsilon_r$. The $\varepsilon_r'$ is related to the polarization and $\varepsilon_r''$ is related to losses in the medium. The loss depends on the frequency of the light waves, where we saw a spectrum of absorption coefficients as a function of photon energy.

Substituting complex relative permittivity $\varepsilon_r$ equation (2.8) into equation (2.7) results in the complex refractive index *N* [32],

$$N = n - iK \tag{2.9}$$

where *n* refers to real part accounting refraction and *K* refers to imaginary part accounting for amount of attenuation, that is, *K* corresponds to the amount of loss due to absorption and scattering [51].

By combining equations (2.8) and (2.9), we can express refractive index as follows [32],

$$N = n - iK = \sqrt{\varepsilon_r} = \sqrt{\varepsilon_r' - i\varepsilon_r''} \tag{2.10}$$

By squaring both sides of the equation (2.10), we can relate $\varepsilon_r'$ and $\varepsilon_r''$ in terms of *n* and *k* [32],

$$\begin{aligned} \varepsilon_r' &= n^2 - K^2 \\ \varepsilon_r'' &= 2nK \end{aligned} \tag{2.11}$$

The optical properties of materials are reported either by showing the frequency dependence of *n* and *k* or $\varepsilon_r'$ and $\varepsilon_r''$.

### 2.5.3 Kramers- Kronig dispersion relation

In *Kramers-Kronig* relationship, if we know the imaginary part of relative permittivity by frequency $\varepsilon_r''(\omega)$, then we can find the real part of relative permittivity $\varepsilon_r'(\omega)$, or vice versa. The *Kramers-Kronig* relation which connects real and imaginary part of relative permittivity, also can be extended into a relationship between absorption coefficient and refractive index. So, the relationship between absorption coefficient and refractive index by frequency is the result of the *Kramer-Kronig* relation.

The *Kramers-Kronig* relations for $\varepsilon_r = \varepsilon_r' + i\varepsilon_r''$ is given by [32],

$$\varepsilon_r'(\omega) = 1 + \frac{2}{\pi} P \int_0^{\infty} \frac{\omega' \varepsilon_r''(\omega')}{\omega'^2 - \omega^2} d\omega' \tag{2.12a}$$

and

$$\varepsilon_r''(\omega) = -\frac{2\omega}{\pi} P \int_0^{\infty} \frac{\varepsilon_r'(\omega')}{\omega'^2 - \omega^2} d\omega' \tag{2.12b}$$

where $\omega'$ is integration variable, $\omega$ is the frequency of interest, and $P$ represents the Cauchy principal value of integral where singularity at $\omega' = \omega$ is avoided. The integration is done from $\omega' = 0$ to infinity [54].

Similarly, one can determine the refractive index as a function of frequency $n_o(\omega)$ from the absorption coefficient as a function of frequency, $\alpha(\omega)$, where $c$ is the speed of light [54].

$$n_0(\omega) = 1 + \frac{c}{\pi} P \int_0^{\infty} \frac{\alpha(\omega')}{\omega'^2 - \omega^2} d\omega' \tag{2.13}$$

Due to the Kramers-Kronig relationship, the frequency dependence of the real part of the refractive index is related to absorption as a function of frequency.

### 2.5.4 Dispersion

The refractive index $n$ depends on the frequency of light, since the $\varepsilon_r$ depends on frequency too, which is known as *dispersion*. Generally, the refractive index increases as the frequency of light increases, which is called *normal dispersion*. However, there is a case that the refractive index decreases as frequency increases, which is known as *anomalous dispersion* [51]. From the

refractive index spectrum in Figure 2.13b, photon energy below 3.5 eV is the *normal dispersion* region where refractive index *n* goes up with photon energy ħω, and photon energy above 3.5 eV is the *anomalous dispersion* where *n* goes down with ħω, and the sudden peak in photon energy 3.5 eV is known as *resonance frequency* ($\omega_o$) or *resonance wavelength* ($\lambda_o$). Both $\varepsilon_r$' and *n* peak at ~3.5 eV and both $\varepsilon_r$'' and *K* peak at 3.5 eV and 4.5 eV.

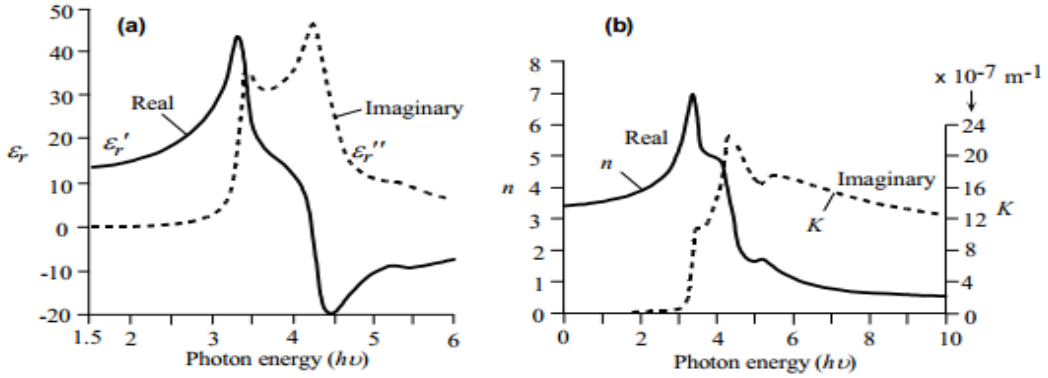


Figure 2. 13. (a) Complex relative permittivity of a silicon crystal as a function of photon energy plotted in terms of the real and imaginary parts. (b) The optical properties of a silicon crystal vs. photon energy in terms of the real (n) and imaginary (K) parts of the complex refractive index (After [51]).

If we let $\varepsilon_{dc}$ be $\varepsilon_r(0)$, the normal dispersion below $\omega_0$ can be expressed by [51],

$$n^2 \approx 1 + (\varepsilon_{dc} - 1)\frac{{\omega_0}^2}{{\omega_0}^2 - \omega^2} \quad (\omega < \omega_0) \tag{2.14a}$$

Since $\lambda = 2\pi c/\omega$, defining $\lambda_o = 2\pi c/\omega_o$ as the resonance wavelength, equation (2.14a) becomes,

$$n^2 \approx 1 + (\varepsilon_{dc} - 1)\frac{{\lambda_0}^2}{{\lambda_0}^2 - \lambda^2} \quad (\lambda > \lambda_0) \tag{2.14b}$$

However, equations (2.14a) and (2.14b) are too simple to express the multiple oscillations with different resonances. In this case, we consider an empirical formula such as *Cauchy* or *Sellmeier*, with various oscillating factors $A_1$, $A_2$, $A_3$ or *A*, *B* and *C*.

The *Cauchy* is represented as [51],

$$n = A + \frac{B}{\lambda^2} + \frac{C}{\lambda^4} \tag{2.15}$$

The *Cauchy* is usually applied in the visible region of spectrum (See the Figure 2.14) for various optical glasses. *Cauchy* has recently been replaced by the *Sellmeier* dispersion relation.

The *Sellmeier* dispersion origin is that the solid is represented by a sum of *N* Lorentz oscillators with different weighting factors ($A_1$, $A_2$, $A_3$ … etc.), and $\lambda_i$ representing different *resonance wavelengths* [51].

$$n^2 = 1 + \frac{A_1\lambda^2}{\lambda^2 - \lambda_1^2} + \frac{A_2\lambda^2}{\lambda^2 - \lambda_2^2} + \frac{A_3\lambda^2}{\lambda^2 - \lambda_3^2} + \cdots \tag{2.16}$$

where $A_1$, $A_2$, $A_3$ and $\lambda_1$, $\lambda_2$ and $\lambda_3$ constants are called *Sellmeier coefficients*, which are determined by fitting into the experimental data. The three terms i= 1, i= 2, i= 3 are commonly used in the Sellmeier equation, mostly neglecting term i = 4,5,6 … etc [51].

The Sellmeier dispersion equation works well for describing dispersion than Cauchy. As can be seen in figure 2.14 below, the Sellmeier dispersion (green dotted) is well fitted in the measured values of refractive index *n* in most of wavelength region, whereas the Cauchy dispersion is deviated from the measured values (red cross) outside of the visible range (shaded dense pattern).

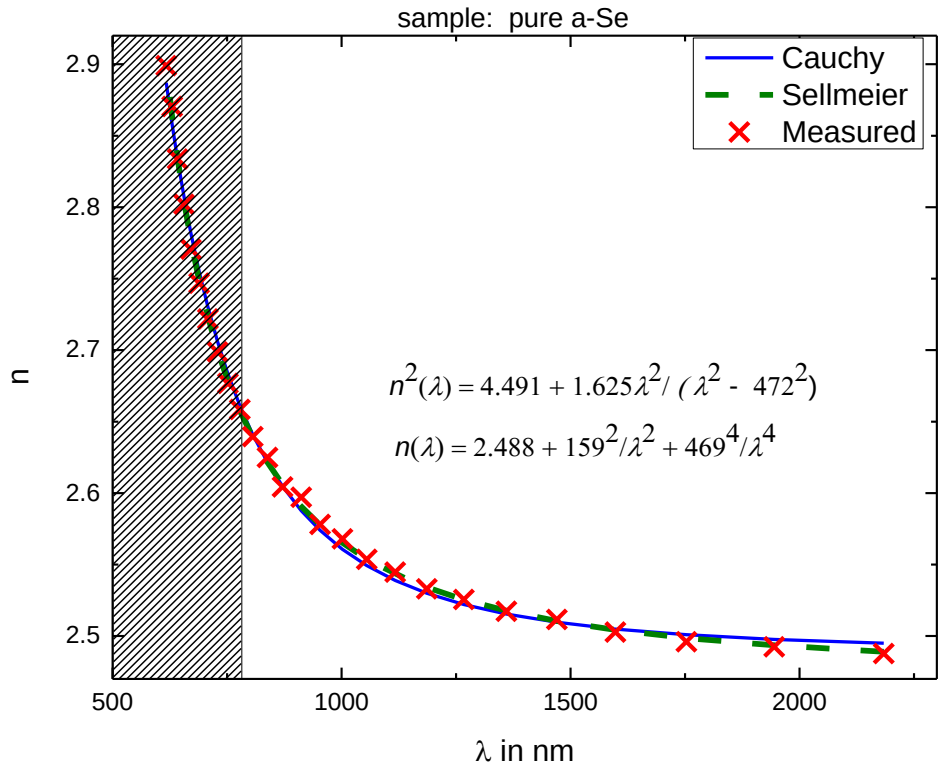


Figure 2. 14. The refractive index of pure amorphous selenium film with $\bar{d}$ = 1756nm and Δd = 11nm fitted into Cauchy (blue line) and Sellmeier (dotted green line) dispersion equations.

Furthermore, the refractive index can be fitted into another model called *Wemple-DiDominicio*, which is based on a single-oscillator model. It is used to calculate the refractive index for photon energies below the inter-band absorption edge [51],

$$n^2 = 1 + \frac{E_o E_d}{{E_o}^2 - (\hbar\omega)^2} \tag{2.17}$$

where $E_o$ is the energy of the effective dispersion oscillator, or simply single oscillator energy, which corresponds to mean transition energy (average energy gap) from VB of lone-pair state to the CB of anti-bonding state. $E_d$ is the dispersion energy which measures the average strength of optical transitions. The $E_d$ obeys other important empirical relationship as following [51],

$$E_d = \beta\, N_c\, Z_a\, N_e, \tag{2.18}$$

where $N_c$ is the coordination number of nearest-neighbor cations to the anion, $Z_a$ is the formal chemical valency of anion, $N_e$ is the effective number of valence electrons per anion, and $\beta$ is a

constant depending on whether interatomic bond is ionic or covalent, that is 0.37 ± 0.04 eV for covalent material and 0.26 ± 0.03 eV for ionic material [57].

Also, $E_o$ is related with optical band gap $E_g$ as [51],

$$E_o = C \times E_g \tag{2.19}$$

where $C$ is a constant determined by empirical fitting, and $E_g$ is the lowest direct band gap ~ $Eg_T$.

### 2.5.5 Influence of polarization and density on the refractive index

The refractive index is also affected by polarizability of medium and local field inside the material through *Lorentz-Lorentz* (or *Claudius –Mossotti)* relation as follows,

$$\frac{\varepsilon_r - 1}{\varepsilon_r + 2} = \frac{n^2 - 1}{n^2 + 2} = \sum_j \frac{N_j \alpha_j}{3\varepsilon_o} = \frac{1}{3\varepsilon_0} \sum_j \alpha_j \frac{\rho_j N_A}{M_{at,j}} \tag{2.20}$$

where $\varepsilon_o$ is the vacuum permittivity, $\varepsilon_r$ is relative permittivity, $N$ is atomic number density (number of atoms per unit volume) and $\alpha$ is the polarizability per molecule (or atom). The atomic number density $N$ in equation (2.20) is expressed by $N = \rho N_A / M_{at}$ where $\rho$ is density, $N_A$ is Avogadro number, and $M_{at}$ is the molar mass. Equation 2.20 implies refractive index $n$ is increased by both atomic concentrations (atomic number density $N$) and polarizability $\alpha$ [58], which we already discussed from Section 2.5.2 that the denser medium and the stronger polarization slow down the propagation of light, which leads to the increase in refractive index.

If polarizability is negligible in equation (2.20) and assuming $N$ is inversely proportional to the volume (or thickness) of the film, then the relationship between thickness and refractive index can be extracted as follows, [58]

$$\frac{n^2 - 1}{n^2 + 2} = \frac{C}{d} \tag{2.21}$$

where C is a constant including polarizability and material information (i.e. atomic mass).

Equation (2.21) can be re-written in terms of the change in refractive index $\Delta n$ and the change in density $\Delta\rho$ (or change in thickness) according to Gonzalez, et al [57],

$$\frac{\Delta n}{n} = \frac{(n^2 - 1)(n^2 + 2)}{(6n^2)}\frac{\Delta\rho}{\rho} \tag{2.22a}$$

$$\frac{\Delta n}{n} = \frac{-(n^2 - 1)(n^2 + 2)}{(6n^2)}\frac{\Delta\bar{d}}{\bar{d}} \tag{2.22b}$$

implies that density expansion (or thickness decrease $\Delta d/d < 0$) gives rise to an increase in refractive index ($\Delta n/n > 0$), unless affected by polarizability of molecules [54].

### 2.5.6 Moss's rule

For a semiconductor, Moss has proposed the relation (*Moss's rule*) between $n$ and $Eg_T$ as follows [59],

$$n^4 E_g = K = \text{Constant} \tag{2.23}$$

Based on the classical oscillator theory, *Hervé* and *Vandamme* have proposed the relationship between $n$ and $Eg$ in semiconductors as [60],

$$n^2 = 1 + \left(\frac{A}{E_g + B}\right)^2 \tag{2.24}$$

where $A$ = 13.6 eV, $B$ = 3.4 eV and $dB/dT = 2.5\times10^{-5}$ eV/K are constants.

# Chapter 3. Analysis of Thin Film Transmission spectrum

## 3.1 Introduction

In the thin film, it is impossible to extract optical parameters directly from the transmission or reflectance spectrum. The multiple interference makes it impossible to hold the Beer-Lambert law ($I(x)= I_o \exp(\alpha x)$). Also, the measured transmission spectrum is a complicated function relying on the other physical constants such as thickness, surface roughness or substrate [61].

In the case of multiple wavelike patterns, a model approach turns out to be useful and one of the reliable models is the Swanepoel [62]. In Swanepoel's method, we measure the transmission spectrum on the surface of the film and then extract all necessary optical constants according to a model transmission which expresses the transmission in a mathematical formula. The Swanepoel technique requires only transmission spectrum and it can generate accurate values on thickness, wedge, refractive index and absorption coefficients. The method is based on envelope construction and divided in two sections depending on the surface roughness in the films, homogenous film [46] and inhomogeneous [47] film, surface roughness is absent and present respectively.

This chapter discusses all the derivations and methods for extracting optical constants from the transmission spectra, but before discussing Swanepoel, the basic principles of the interference effects in thin film are introduced.

## 3.2 Principles of thin film optics

When the thickness of the film is thin, typically a few microns or less, wavelike patterns appear in the transmittance spectrum. It is because light waves which are reflected at internal and external interfaces interfere constructively or destructively from the superposition principle, appearing as enhancing and reducing intensity in the transmission spectrum [62].

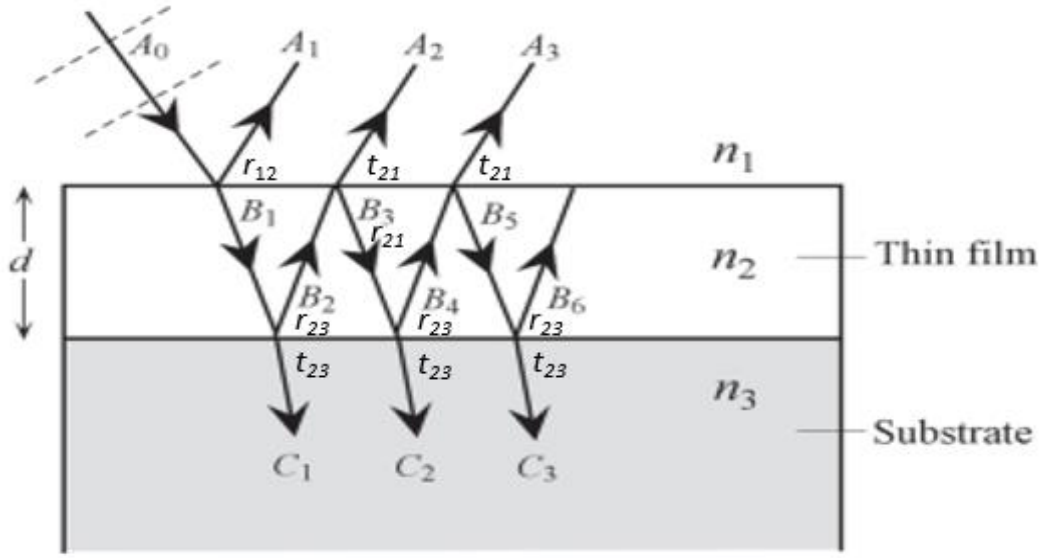


Figure 3. 1. Light travelling in a medium of refractive index n1 is incident on a thin film of index $n_2$ (after [63]).

In this context, we will derive simple equations for the transmittance and reflectance which are determined by multiple wave interference phenomena [51]. We suppose a simple system that light travelling in a medium of air (refractive index $n_1$) enters a thin film (index $n_2$) on top of thick substrate (of index $n_3$) as shown in Figure 3.1. We assume that the incident light has an amplitude of $A_0$, and $A_1, A_2, A_3$ are the amplitudes of reflected light and $C_1, C_2, C_3$ are the amplitudes of transmitted light. The incident light with amplitude $A_0$ is partially reflected with a coefficient of $r_{12}$ and partially transmitted with the coefficient of $t_{12}$ from medium 1 to medium 2. Then, $t_{12}$ is again partially transmitted with its coefficient of $t_{23}$ or reflected with coefficient of $r_{23}$ from medium 2 to medium 3. We can express it as follows [51],

$A_1 = A_0 r_{12}$

$A_2 = A_0 t_{12} r_{23} t_{21}$

$A_3 = A_0 t_{12} r_{23} r_{21} r_{23} t_{21}$

$B_1 = A_0 t_{12}$

$B_2 = A_0 t_{12} r_{23}$

$B_3 = A_0 t_{12} r_{23} r_{21}$

$C_1 = A_0 t_{12} t_{23}$

$C_2 = A_0 t_{12} r_{23} r_{21} t_{23}$

$C_3 = A_0 t_{12} r_{23} r_{21} r_{23} r_{21} t_{23}$

where the *r* and *t* refer to the reflection and transmission coefficients, each respectively.
The *r* and *t* are given by, (the derivations for its coefficients can be found in a text book [32]),

$$r_{12} = \frac{n_1 - n_2}{n_1 + n_2} = -r_{21} \qquad r_{23} = \frac{n_2 - n_3}{n_2 + n_3} \tag{3.1}$$

$$t_{12} = \frac{2n_1}{n_1 + n_2} \qquad t_{21} = \frac{2n_2}{n_1 + n_2} \qquad t_{23} = \frac{2n_2}{n_2 + n_3} \tag{3.1a}$$

where $1\text{-}t_{12}\times t_{21} = r_{12}^2$ (3.1b)

We assume normal incidence here. The phase change upon transversing the thin film thickness *d* is: $\phi = (2\pi n_2 d/\lambda)$ and this phase change must be multiplied by $\exp(-i\phi)$ in crossing the thickness twice. The intensity of all the reflected light is obtained by summing all the amplitudes of coefficients of the reflected light as below,

$$A_{reflected} = A_1 + A_2 + A_3 + A_4 + A_5 + ..$$

$$A_{reflected} / A_0 = r_{12} + t_{12}r_{23}t_{21}e^{-i2\phi} - t_{12}r_{23}r_{21}r_{23}t_{21}e^{-i4\phi} + .. = r_{12} - \frac{t_{12}t_{21}}{r_{12}} . \sum_{k=1}^{\infty} (-r_{12}r_{21}e^{-i2\phi})^k \tag{3.2}$$

The total reflection coefficient *r* and its reflectance *R* are given by,

$$r = \frac{r_{12} + r_{23}e^{-i2\phi}}{1 + r_{12}r_{23}e^{-i2\phi}} \quad \text{and} \quad R = |r|^2 \tag{3.3}$$

Similarly, the intensity of all the transmitted beam is given by,

$$C_{transmitted} = C_1 + C_2 + C_3 + C_4 + C_5 + ..$$

$$C_{transmitted} / A_0 = t_{12}t_{23}e^{-i\phi} - t_{12}t_{23}r_{12}r_{23}e^{-i3\phi} + t_{12}t_{23}r_{12}^2 r_{23}^2 e^{-i5\phi} + ... = -\frac{t_{12}t_{23}e^{i\phi}}{r_{12}r_{23}} \sum_{k=1}^{\infty} (-r_{12}r_{23}e^{-i2\phi})^k \tag{3.4}$$

The total transmission coefficient *t* and its transmittance *T* are given by [51],

$$t = \frac{t_{12}t_{23}e^{-i\phi}}{1 + r_{12}r_{23}e^{-i2\phi}} \quad \text{and} \quad T = (n_3/n_1)|t|^2 \tag{3.5}$$

We can obtain *n* and *k* by measuring *T* and *R*, which is known as "(*R*, *T*) method" [64].

## 3.3 Swanepoel method

The Swanepoel technique is divided in two sections depending on the inhomogeneous or homogeneous surfaces which have roughness ($\Delta d \neq 0$) or no roughness ($\Delta d = 0$) of thin films. We first discuss on the homogeneous method, and then inhomogeneous method.

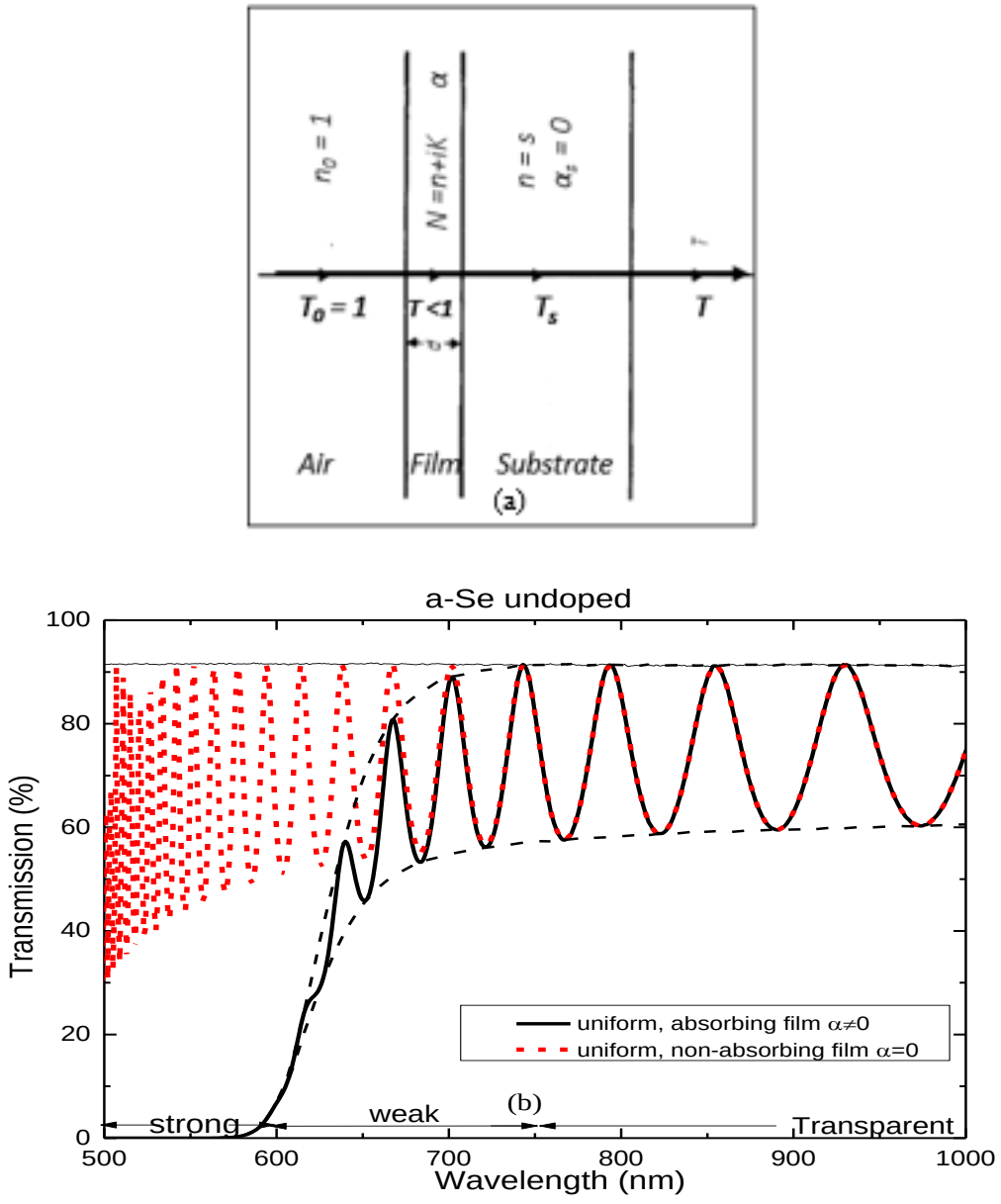


Figure 3. 2. (a): Light transmitting through an absorbing thin film (uniform thickness) on a thick finite transparent substrate [46]. (b): Transmission spectra of pure a-Se uniform film of d= 1.816μm (full curve) compared to that of simulated transmission when assuming no absorption (dotted curvy) with substrate (linear line).

When light entering from the air into the sample in Figure 3.2a, it would first go through the air with refractive index $n_o$ =1, then film ($N = n + iK$), and then finally the transparent substrate ($n = s$). We assume a thin film has a different refractive index and different absorption than its surroundings, substrate and air. We assume no absorption in substrate due to thick thickness ($d_s >> d$).

In Figure 3.2b, oscillating wavelike pattern (linear line) decays (transmission decreases) with decreasing wavelength and then at the short wavelength, all the interference effects start to destroy and finally the transmission reaches zero, merging all curves (maxima, minima and transmission) into a single curve. It is due to the significant absorption $\alpha$ at very high energy. Therefore, when assuming no absorption at all in a thin film, the simulated transmission curve (dotted-curvy line) in Figure 3.2b oscillates over all the wavelengths without decreasing or decaying. Due to the onset of absorption about 750 nm, transmission can be roughly divided into three different regions: the transparent region, where there is no absorption $\alpha \sim 0$, weak absorption region and strong absorption region where interference fringes disappear ($x << 1$). Furthermore, the transmittance is not only a function of wavelength ($\lambda$), and absorption coefficient ($\alpha$) of the thin film, but also a refractive index of the film ($n$), substrate refractive index ($s$) and thickness ($d$), that is,

$$T = f(\lambda, s, n, d, \alpha) \tag{3.6}$$

The Swanepoel technique originally assumes a uniform thickness as shown in figure 3.2, but some films possess wedge-like shapes in the spot of the film, which is referred to as non-uniform films. In non-uniform films, the thickness of surface within the incident light region is linearly varied by a wedge ($\pm\Delta d$), that is $d = \bar{d} \pm \Delta d$, as shown in Figure 3.3a, where $\Delta d$ is the change in thickness over the radius $r$ of spectrophotometer beam, so that the wedge slope is $\Delta d/r$. This wedge should be considered, otherwise it would produce errors in the values of refractive index, thickness or absorption coefficient. The presence of wedge changes the transmission spectrum of uniform film. In Figure 3.3b, the whole transmittance curve of the red line with $\Delta d = 0$ (uniform film) is shifted down to the black line with $\Delta d$ =30 nm, which causes more absorption in all regions. The transmission spectrum of non-uniform film is expressed as,

$$T = f(\lambda, n, d, x, \Delta d) \tag{3.17}$$

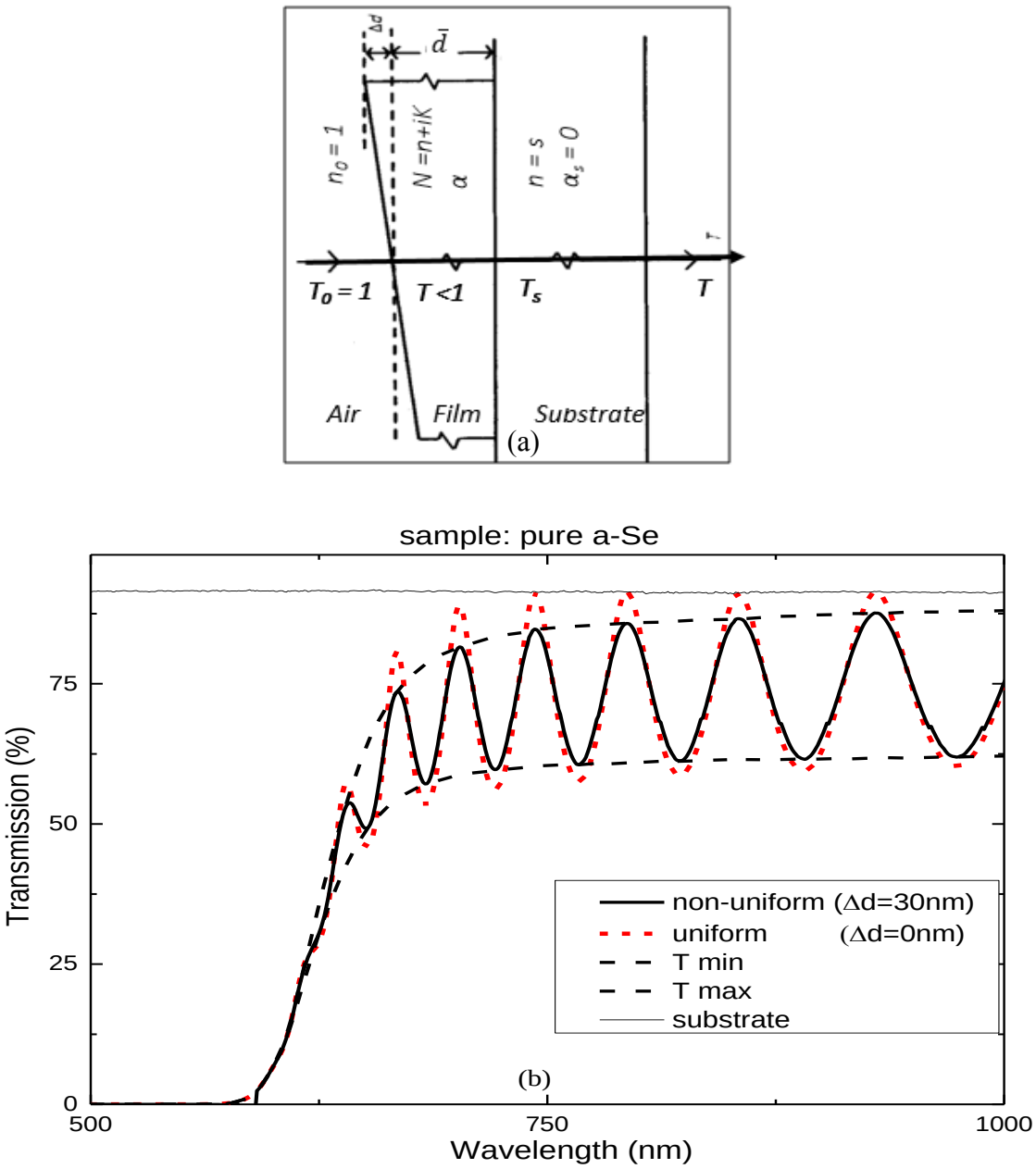


Figure 3. 3. (a): Light transmitting through an absorbing thin film with a variation in thickness (non-uniform) on a thick finite transparent substrate [47]. (b): Simulated transmission of pure a-Se film with uniform thickness of 1.816μm (dotted-curve spectrum) and transmission of the same pure a-Se film with a roughness $\Delta d$ = 30 nm (full-curve spectrum).

## 3.4 Swanepoel's uniform film technique

### 3.4.1. Transmission spectrum

As described in equation 3.6, we are aware that the transmittance of a uniform film depends on $\lambda$, $n$, $s$, $d$ and $\alpha$.

$$T = f(\lambda, s, n, d, \alpha) \tag{3.6}$$

where $s$ is scanned as a function of wavelength.

According to Swanepoel [46], transmittance in a uniform film can be expressed as below,

$$T = \frac{Ax}{B - Cx\cos\varphi + Dx^2} \tag{3.7}$$

where

$$A = 16n^2 s \tag{3.7a}$$

$$B = (n+1)^3(n+s^2) \tag{3.7b}$$

$$C = 2(n^2-1)(n^2-s^2) \tag{3.7c}$$

$$D = (n-1)^3(n-s^2) \tag{3.7d}$$

$$\varphi = \frac{4\pi n\bar{d}}{\lambda} \tag{3.7e}$$

$$x = \exp(-\alpha\bar{d}) \tag{3.7f}$$

where $n$ is the refractive index, $s$ is the substrate index, $\alpha$ is the absorption coefficient, and $d$ is the thickness.

Then, the envelop at the extremes of interference fringes ($T_M$) and ($T_m$) can be generated from the equation (3.7), by substituting $\cos\varphi = 1$ for the upper (maxima) envelop and $\cos\varphi = -1$ for lower (minima) envelop as follows,

$$T_M = \frac{Ax}{B - Cx + Dx^2} \tag{3.8a}$$

$$T_m = \frac{Ax}{B + Cx + Dx^2} \tag{3.8b}$$

### 3.4.2 Envelope construction

The basic concept behind the Swanepoel technique is on envelop construction [65].

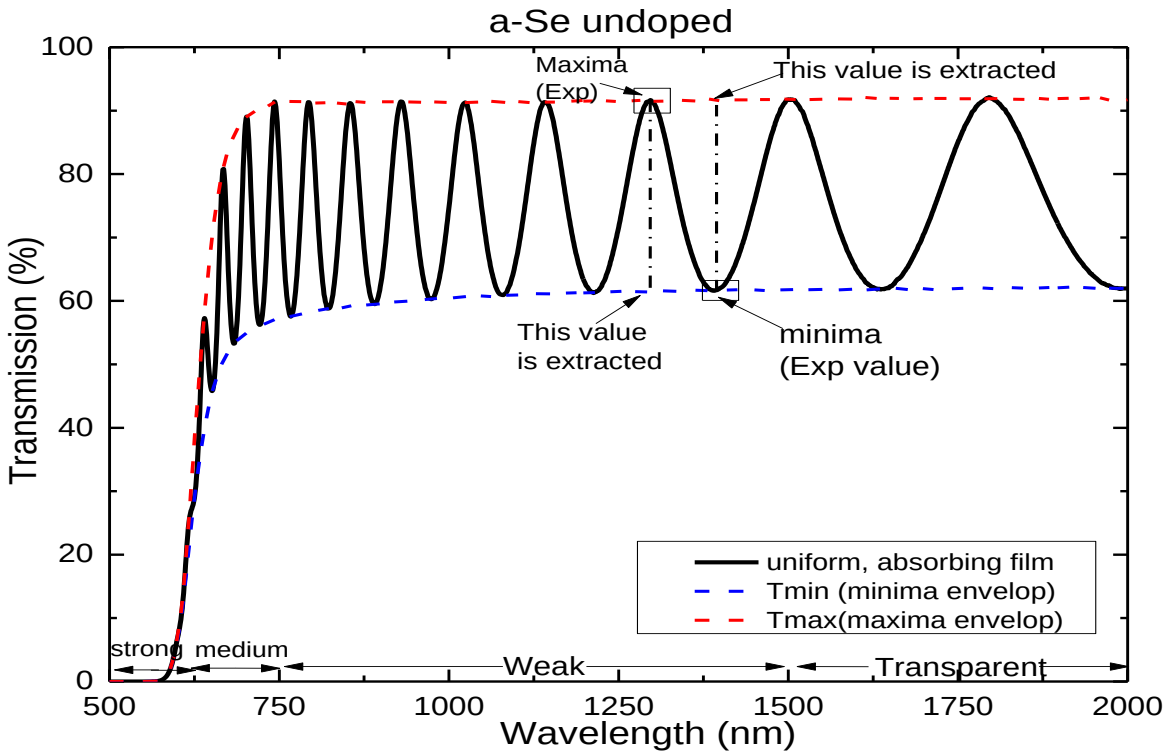


Figure 3. 4. The construction of lower and upper envelopes in the transmission spectra for a 1.816μm uniform film of a-Se. The red dashed curve is an upper envelope and blue dashed curve a lower envelope.

As shown in Figure 3.4 above, the lower (minima) and upper (maxima) envelopes are generated by passing through the minimum and maximum points tangentially using Origin 7. The envelope generation makes it possible to locate the corresponding $T_M$ value of $T_m$ (or $T_m$ values of $T_M$), which are called the interference fringes. From the envelop generation as a continuous spectrum in wavelength (i.e. $T_M(\lambda)$, $T_m(\lambda)$), the values of $T_M$, $T_m$ are used to find $n$ and $k$ at each extremum, and then generate values on $n(\lambda)$, $k(\lambda)$ at all wavelengths [64].

### 3.4.3 Determination of refractive index

We earlier described that the upper and lower envelops are simulated in equation (3.8a) and (3.8b). Subtracting the reciprocal of equation (3.8a) from the reciprocal of equation (3.8b) yields an expression which is independent of *x* as follows,

$$\frac{1}{T_{\mathrm{m}}} - \frac{1}{T_{\mathrm{M}}} = \frac{(B + Cx + Dx^2) - (B - Cx + Dx^2)}{Ax} = \frac{2C}{A}$$

$$\frac{1}{T_{\mathrm{m}}} - \frac{1}{T_{\mathrm{M}}} = \frac{4(n^2 - 1)(n^2 - s^2)}{16n^2 s} \tag{3.8c}$$

Solving for *n* results in,

$$n_{\mathrm{crude}} = [N + (N^2 - s^2)^{1/2}]^{1/2} \tag{3.9}$$

where

$$N = 2s\frac{T_{\mathrm{M}} - T_{\boldsymbol{m}}}{T_{\mathrm{M}} T_{\mathrm{m}}} + \frac{s^2 + 1}{2} \tag{3.9a}$$

This states that refractive index *n* can be determined only from the values of $T_{\mathrm{m}}$ and $T_{\mathrm{M}}$ obtained from experimental envelope generation.

The refractive index *n* in equation (3.9) in the weak absorption region is to be fitted into a dispersion from of equation (i.e. Cauchy or Sellmeier), to calculate the extrapolated values of *n* in the strong absorption region. This is because all the interference fringe patterns are destroyed in the strong absorption region.

$$\text{Sellmeier disperion form: } n = \sqrt{A + \frac{B\lambda^2}{\lambda^2 - C^2}}$$

where *A, B* and *C* coefficients are determined from the experimental fitting. Figure 3.5 shows the Sellmeier dispersion equation of *n* with $n_{\mathrm{crude}}$ from equation (3.9).

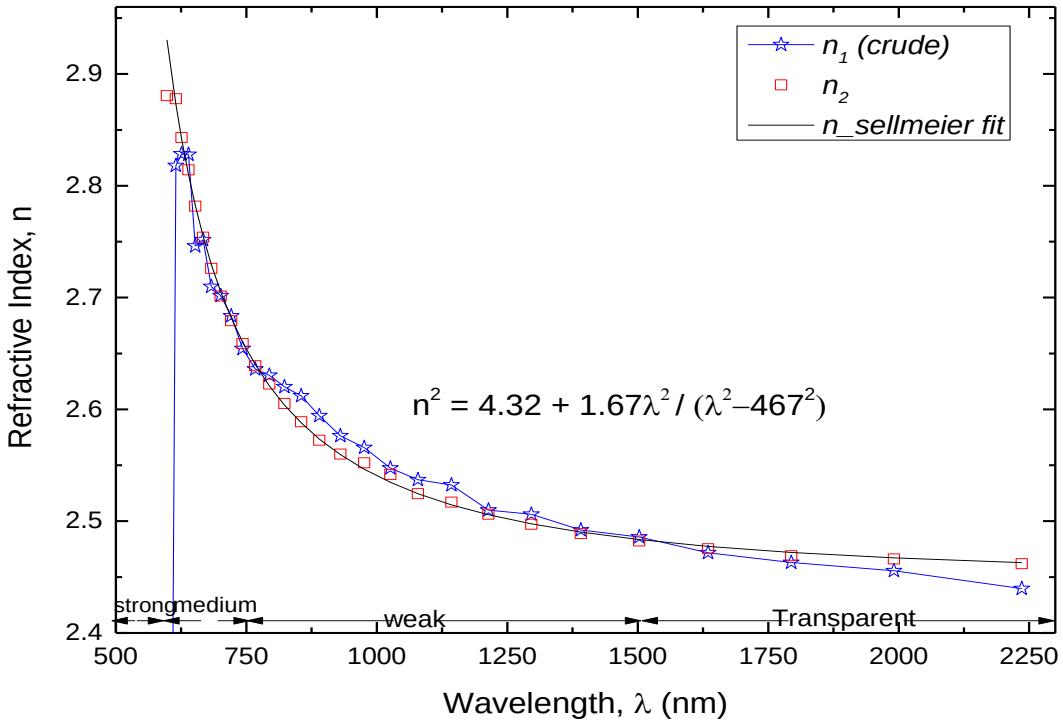


Figure 3. 5. Improvement on refractive index of pure a-Se uniform film. The crude n was obtained from equation (3.9), and n2 was obtained from improving thickness using equation (3.16c), which is a poor approximation in strong absorption, and nfit is the best dispersion curve (3.16d) without any deviations.

### 3.4.4 Substrate refractive index

The transmittance of the substrate in the absence of film $T_s(\lambda)$ gives an interference-free spectrum.

$$T_s = \frac{2s}{s^2+1} \quad \text{or} \quad s = \frac{1}{T_s} + \left(\frac{1}{T_s^{\,2}} - 1\right)^{1/2} \tag{3.10}$$

The transmission of substrate $T_s(\lambda)$ was scanned as a function of wavelength to find the substrate index $s$ as a function of wavelength.

### 3.4.5 Determination of thickness

According to Swanepoel, the basic equation for interference fringes is,

$$2nd = m\lambda \tag{3.16}$$

where *n* is obtained from Equation (3.6), and *m* is an integer for maxima and half integer for minima. The λ is the corresponding wavelength at each extremum.

Rearranging equation (3.16) in terms of *m* ( $m = \frac{2nd}{\lambda}$ ) and subtracting the two adjacent maxima (or minima) result in an equation which is independent of *m*,

$$\frac{2n_{m+1}d}{\lambda_{m+1}} - \frac{2n_m d}{\lambda_m} = (m+1) - (m) = 1 \tag{3.11}$$

$$d_{\text{crude}} = \frac{\lambda_{m+1}\lambda_m}{2(\lambda_m n_{m+1} - \lambda_{m+1} n_m)} \tag{3.12}$$

where $n_m$ and $n_{m+1}$ are the refractive indices at two adjacent maxima (or minima) and $\lambda_m$ and $\lambda_{m+1}$ are corresponding wavelengths. Equation (3.12) implies that it simply requires crude refractive indexes $n_{m+1}$ and $n_m$ (equation (3.9)) at extremum wavelengths $\lambda_{m+1}$ and $\lambda_m$ to determine the thickness.

### 3.4.6 Absorption coefficient

The maxima and minima envelope (equations (3.8a) and (3.8b)) are quadratic equations in *x* that can be solved for *x*.

By re-arranging equation (3.8a), we have,

$$(T_M D)x^2 - (T_M C + A)x + T_M B = 0 \tag{3.13}$$

Solving for *x* results in,

$$x = \frac{E_M - [E_M^2 - (n^2-1)^3(n^2 - s^4)]^{1/2}}{(n-1)^3(n-s^2)} \tag{3.14}$$

where

$$E_M = \frac{8n^2 s}{T_M} + (n^2-1)(n^2 - s^2) \tag{3.14a}$$

and

$$\alpha = \frac{\ln x}{\bar{d}} \tag{3.15}$$

It is important to remember that finding absorption coefficient $\alpha$ should be performed at the end after obtaining and optimizing all the values. Because, the refractive index value $n$ is sensitive to errors in the high absorption region where most of absorption coefficient values are determined.

### 3.4.7. Swanepoel's optimization method

The obtained values of refractive index (equation (3.9)) and thickness (equation (3.12)) are not accurate. These are crude refractive index $n_{\text{crude}}$ and crude thicknesses $d_{\text{crude}}$ which are roughly estimated, so are sensitive to errors [62]. Therefore, this section describes the method to improve and optimize all constants $d$, $n$, $m$, and $\alpha$.

Now, an improvement on the values of all the optical constants can be done by the equations of interference fringes as below,

$$2nd = m\lambda \tag{3.16}$$

First, the order number (order of interference fringe) can be improved by re-arranging the equation (3.16) in terms of $m$. This $m$ is to be determined at each of extrema $\lambda_{\text{ext}}$.

$$m_{crude} = \frac{2n_{crude}\bar{d}_{crude}}{\lambda_{ext}} \tag{3.16a}$$

The order number $m$ can increase precision, by rounding it to an integer, if $n$ and $\lambda$ were taken at maxima, or half integer, if $n$ and $\lambda$ were taken at minima. We would denote an improved order number after rounding as $m_{new}$.

The thickness $d_{\text{crude}}$ can be improved with improved $m_{\text{new}}$ at each extrema $\lambda_{\text{ext}}$, by rearranging equation (3.16a) in terms of $d$,

$$d_{new} = \frac{m_{new}\lambda_{ext}}{2n_{crude}} \tag{3.16b}$$

We would denote an improved thickness as $d_{\text{new}}$. After obtaining all the thickness at all extrema, the new thickness should be averaged, $\bar{d}_{\text{new}}$.

Once we have improved $m$ and $d$, now it is a turn to improve refractive index $n_{new}$ with improved $m_{\text{new}}$ and improved $\bar{d}_{\text{new}}$, by re-arranging equation (3.16b) in terms of $n$,

$$n_{new} = \frac{m_{new}\lambda_{ext}}{2\bar{d}_{new}} \tag{3.16c}$$

We would denote an improved refractive index as $n_{\text{new}}$.

The next step is to fit the obtained $n_{\text{new}}$ into a form of Sellmeier equation as below,

$$\text{Sellmeier disperion form: } n_{fit} = \sqrt{A + \frac{B\lambda^2}{\lambda^2 - C^2}} \tag{3.16d}$$

where the $A$, $B$, $C$ coefficients are determined from the fit. When these coefficients are determined, the refractive indexes $n$ can now be calculated at any wavelength between 450 and 2000 nm.

The transmittance values are re-generated from the equation below.

$$T_{calc} = \frac{Ax}{B - Cx\cos\varphi + Dx^2} \tag{3.16e}$$

where $A$, $B$, $C$, $D$, $\varphi$ and $x$ are given in equation (3.7), which depends on $n$. The $A$, $B$, $C$, $D$, $\varphi$ and $x$ can be easily generated at all wavelengths from 450 to 2000 nm using the coefficients of fits in equation (3.16d).

Finally, Root mean square errors (RMSE) can be evaluated from,

$$\text{RMSE} = \sqrt{\frac{\sum_{i=1}^{q}(T_{\text{exp}} - T_{\text{calc}})^2}{q}} \tag{3.16f}$$

where $T_{\text{exp}}$ refers to the experimental transmission data, and $T_{\text{calc}}$ is the transmittance of the regenerated spectrum (equation (3.16e)), and $q$ is the number of data ranges. This RMSE evaluates % errors for each chosen average thickness and constants. The ideal average thickness $\bar{d}_{\text{new}}$ should give the minimum RMSE.

A good estimation to select the $\bar{d}_{new}$ is to cross out thicknesses in the absorption region (i.e. $\lambda$ below 750 nm) and transparent region (i.e. $\lambda$ above 1900 nm) and to average $d_{new}$ in the remaining region. In Table 3.1, the thicknesses $d_{new}$ in wavelength $\lambda$ between 750 nm and 1900 nm ranges from a minimum of $d_{new,min}$ = 1800 nm to a maxmum of $d_{new,max}$ = 1820 nm with a standard deviation of 6.4 nm and an average $\bar{d}$ of 1810.9 nm. This average thickness, $\bar{d}$ of 1810.9 nm, is again plotted using equation (3.16c) to extract optical constants in equation (3.16d) then to extract its transmission spectrum (3.16e). The RMSE equation (3.16f) gives 0.49 %. Table 3.1 lists the results of the optical constants generated with a thickness $\bar{d}$ of 1810.9 nm at all extrema ($\lambda_{ext}$).

However, the RMSE can be smaller than 0.49 % by using different optical constants generated from a different average thickness $\bar{d}_{new}$. Once all optical constants and its RMSE are obtained for one thickness (i.e. $\bar{d}_{new}$ =1810.9nm), then go back to equation (3.16b), and choose a different average thickness $\bar{d}_{new}$ (i.e. from $d_{new,min}$ = 1800nm to $d_{new,max}$ =1820nm), calculate the new refractive index $n_2$ from equation (3.16c), fit into equation (3.16d), regenerate transmission from equation (3.16e), and finally calculate RMSE from equation (3.16f) at each new average thickness $\bar{d}_{new}$. This whole procedure from (3.16a) to (3.16f) are re-iterated with a series of different average thicknesses $\bar{d}_{new}$ in the selected region (i.e. from $d_{new,min}$ = 1800nm to $d_{new,max}$ =1820nm) until reaching the minimum RMSE. There is an easy method to do it in Matlab. Matlab can automatically perform and re-iterate all these steps, from (3.16a) to (3.16f), at each average thickness: 1800nm, 1801nm, 1802nm ... 1820nm, and can give a series of optical constants (Sellmeier coefficient terms: *A*, *B*, *C* of $n_{fit}$) as well as the RMSE at each given thickness. Once it generates all, we select the $\bar{d}_{new}$ which has the minimum RMSE. The average thickness $\bar{d}_{new}$ which gives the minimum RMSE (0.47%) comes up to be 1816.2nm, with its Sellmeier coefficient term: *A* = 4.32, *B* = 1.67 and *C* = 467 nm, as shown in Table 3.2. This 0.47% of RMSE is smaller than the 0.49% of RMSE which used 1810.9nm average thickness in Table 3.1. The re-iteration procedure in Table 3.2 gives a better precision in thickness and Sellmeier coefficient terms with smaller errors. Figure 3.6 is the re-generated transmission spectrum from the results of the Table 3.2.

Table 3. 1. Optical parameters of pure a-Se uniform film obtained from $\bar{d}_{new}$ of 1810.9nm. Values of $\lambda_{ext}$, $s$, $T_M$ and $T_m$ for the spectrum of figure 3.6. Calculation of $N$, $n_{crude}$, $n_{new}$, $n_{fit}$ and $d_{crude}$ and $d_{new}$. ($N$ from equation (3.9a), $n_{crude}$ from equation (3.9). $d_{crude}$ from equation (3.12). $m_{crude}$ and $m$ from equation (3.16a). $d_{new}$ from equation (3.16b). $n_{new}$ from equation (3.16c). $n_{fit}$ from equation (3.16d) with Sellmeier coefficient terms: $A = 4.35$, $B = 1.68$ and $C = 467$nm).

| $\lambda_{ext}$ nm | $s$ | $T_M$ % | $T_m$ % | $N$ | $n_{crude}$ | $d_{crude}$ nm | $m_{crude}$ | $m_{new}$ | $d_{new}$ nm | $n_{new}$ | $n_{fit}$ |
|---|---|---|---|---|---|---|---|---|---|---|---|
| **2236** | 1.522 | 0.911 | 0.627 | 3.171 | 2.440 | | 3.96 | 4 | 1833.0 | 2.470 | 2.470 |
| **1991** | 1.514 | 0.919 | 0.624 | 3.205 | 2.456 | | 4.47 | 4.5 | 1824.3 | 2.474 | 2.475 |
| **1794** | 1.514 | 0.919 | 0.621 | 3.222 | 2.463 | 1773.8 | 4.98 | 5 | 1820.9 | 2.477 | 2.480 |
| **1635** | 1.520 | 0.918 | 0.620 | 3.244 | 2.472 | 1796.2 | 5.48 | 5.5 | 1819.1 | 2.483 | 2.485 |
| **1503** | 1.526 | 0.916 | 0.617 | 3.278 | 2.486 | 1779.4 | 6.00 | 6 | 1813.8 | 2.490 | 2.491 |
| **1391** | 1.527 | 0.916 | 0.616 | 3.293 | 2.492 | 1786.8 | 6.50 | 6.5 | 1814.0 | 2.496 | 2.498 |
| **1296** | 1.532 | 0.915 | 0.612 | 3.328 | 2.506 | 1786.7 | 7.01 | 7 | 1809.9 | 2.505 | 2.505 |
| **1214** | 1.531 | 0.914 | 0.611 | 3.336 | 2.510 | 1812.3 | 7.50 | 7.5 | 1813.8 | 2.514 | 2.514 |
| **1143** | 1.545 | 0.913 | 0.608 | 3.393 | 2.532 | 1774.7 | 8.04 | 8 | 1805.4 | 2.525 | 2.522 |
| **1079** | 1.542 | 0.913 | 0.606 | 3.403 | 2.537 | 1761.8 | 8.53 | 8.5 | 1807.5 | 2.532 | 2.532 |
| **1026** | 1.541 | 0.911 | 0.602 | 3.428 | 2.547 | 1870.4 | 9.01 | 9 | 1812.4 | 2.550 | 2.543 |
| **976** | 1.545 | 0.912 | 0.598 | 3.473 | 2.566 | 1800.5 | 9.54 | 9.5 | 1806.8 | 2.560 | 2.554 |
| **930** | 1.537 | 0.911 | 0.592 | 3.497 | 2.576 | 1739.4 | 10.05 | 10 | 1804.8 | 2.568 | 2.567 |
| **890** | 1.541 | 0.911 | 0.589 | 3.541 | 2.594 | 1748.8 | 10.57 | 10.5 | 1801.1 | 2.580 | 2.581 |
| **855** | 1.548 | 0.911 | 0.586 | 3.587 | 2.612 | 1755.8 | 11.08 | 11 | 1800.3 | 2.597 | 2.596 |
| **823** | 1.547 | 0.910 | 0.583 | 3.607 | 2.620 | 1859.3 | 11.55 | 11.5 | 1806.0 | 2.613 | 2.612 |
| **794** | 1.540 | 0.911 | 0.578 | 3.631 | 2.630 | 1939.4 | 12.02 | 12 | 1811.1 | 2.631 | 2.629 |
| **767** | 1.532 | 0.911 | 0.575 | 3.643 | 2.636 | 1976.3 | 12.47 | 12.5 | 1818.5 | 2.647 | 2.648 |
| **743** | 1.535 | 0.908 | 0.569 | 3.690 | 2.654 | 1926.3 | 12.96 | 13 | 1819.5 | 2.667 | 2.668 |
| **721** | 1.544 | 0.901 | 0.561 | 3.766 | 2.684 | 1753.1 | 13.50 | 13.5 | 1813.5 | 2.688 | 2.690 |
| **701** | 1.534 | 0.890 | 0.550 | 3.811 | 2.702 | 1775.7 | 13.98 | 14 | 1816.3 | 2.710 | 2.713 |
| **683** | 1.535 | 0.855 | 0.534 | 3.832 | 2.710 | 2035.2 | 14.39 | 14.5 | 1827.3 | 2.734 | 2.738 |
| **667** | 1.532 | 0.807 | 0.505 | 3.941 | 2.752 | 1842.3 | 14.96 | 15 | 1818.0 | 2.762 | 2.763 |
| **652** | 1.530 | 0.703 | 0.463 | 3.926 | 2.746 | 2048.5 | 15.28 | 15.5 | 1840.1 | 2.790 | 2.791 |
| **639** | 1.534 | 0.574 | 0.392 | 4.146 | 2.828 | 1664.9 | 16.05 | 16 | 1807.6 | 2.823 | 2.819 |
| **626** | 1.530 | 0.393 | 0.298 | 4.147 | 2.829 | 1630.8 | 16.39 | 16.5 | 1825.9 | 2.852 | 2.851 |
| **615** | 1.531 | 0.229 | 0.194 | 4.119 | 2.818 | 3193.4 | 16.62 | 17 | 1855.0 | 2.887 | 2.882 |
| **598** | 1.533 | 0.056 | 0.056 | 1.674 | 1.533 | -255.7 | 9.30 | 17.5 | 3414.0 | 2.889 | 2.940 |

Table 3. 2. Improvements of thickness ($\bar{d}_{\text{new}}$) and optical constants ($n_{\text{new}}$ and $n_{\text{fit}}$) of pure a-Se uniform film with reduced RMSE (0.466%) using re-iteration method in Matlab. Thickness ($\bar{d}_{\text{new}}$) is 1816.2 nm and the Sellmeier coefficient terms of $n_{\text{fit}}$ is: $A = 4.32$, $B = 1.67$ and $C =$ 467nm.

| $\lambda_{ext}$ nm | $s$ | $T_M$ % | $T_m$ % | $N$ | $n_{\text{crude}}$ | $d_{\text{crude}}$ nm | $m_{crude}$ | $m_{new}$ | $d_{new}$ nm | $n_{new}$ | $n_{fit}$ |
|---|---|---|---|---|---|---|---|---|---|---|---|
| **2236** | 1.52 | 0.911 | 0.627 | 3.171 | 2.440 | | 3.96 | 4 | 1833.0 | 2.462 | 2.463 |
| **1991** | 1.51 | 0.919 | 0.624 | 3.205 | 2.456 | | 4.47 | 4.5 | 1824.3 | 2.467 | 2.467 |
| **1794** | 1.51 | 0.919 | 0.621 | 3.222 | 2.463 | 1773.8 | 4.98 | 5 | 1820.9 | 2.469 | 2.472 |
| **1635** | 1.52 | 0.918 | 0.620 | 3.244 | 2.472 | 1796.2 | 5.48 | 5.5 | 1819.1 | 2.476 | 2.478 |
| **1503** | 1.53 | 0.916 | 0.617 | 3.278 | 2.486 | 1779.4 | 6.00 | 6 | 1813.8 | 2.483 | 2.484 |
| **1391** | 1.53 | 0.916 | 0.616 | 3.293 | 2.492 | 1786.8 | 6.50 | 6.5 | 1814.0 | 2.489 | 2.491 |
| **1296** | 1.53 | 0.915 | 0.612 | 3.328 | 2.506 | 1786.7 | 7.01 | 7 | 1809.9 | 2.497 | 2.498 |
| **1214** | 1.53 | 0.914 | 0.611 | 3.336 | 2.510 | 1812.3 | 7.50 | 7.5 | 1813.8 | 2.507 | 2.506 |
| **1143** | 1.55 | 0.913 | 0.608 | 3.393 | 2.532 | 1774.7 | 8.04 | 8 | 1805.4 | 2.517 | 2.515 |
| **1079** | 1.54 | 0.913 | 0.606 | 3.403 | 2.537 | 1761.8 | 8.53 | 8.5 | 1807.5 | 2.525 | 2.525 |
| **1026** | 1.54 | 0.911 | 0.602 | 3.428 | 2.547 | 1870.4 | 9.01 | 9 | 1812.4 | 2.542 | 2.535 |
| **976** | 1.55 | 0.912 | 0.598 | 3.473 | 2.566 | 1800.5 | 9.54 | 9.5 | 1806.8 | 2.553 | 2.547 |
| **930** | 1.54 | 0.911 | 0.592 | 3.497 | 2.576 | 1739.4 | 10.05 | 10 | 1804.8 | 2.560 | 2.560 |
| **890** | 1.54 | 0.911 | 0.589 | 3.541 | 2.594 | 1748.8 | 10.57 | 10.5 | 1801.1 | 2.573 | 2.574 |
| **855** | 1.55 | 0.911 | 0.586 | 3.587 | 2.612 | 1755.8 | 11.08 | 11 | 1800.3 | 2.589 | 2.588 |
| **823** | 1.55 | 0.910 | 0.583 | 3.607 | 2.620 | 1859.3 | 11.55 | 11.5 | 1806.0 | 2.606 | 2.604 |
| **794** | 1.54 | 0.911 | 0.578 | 3.631 | 2.630 | 1939.4 | 12.02 | 12 | 1811.1 | 2.623 | 2.621 |
| **767** | 1.53 | 0.911 | 0.575 | 3.643 | 2.636 | 1976.3 | 12.47 | 12.5 | 1818.5 | 2.639 | 2.640 |
| **743** | 1.54 | 0.908 | 0.569 | 3.690 | 2.654 | 1926.3 | 12.96 | 13 | 1819.5 | 2.659 | 2.661 |
| **721** | 1.54 | 0.901 | 0.561 | 3.766 | 2.684 | 1753.1 | 13.50 | 13.5 | 1813.5 | 2.680 | 2.682 |
| **701** | 1.53 | 0.890 | 0.550 | 3.811 | 2.702 | 1775.7 | 13.98 | 14 | 1816.3 | 2.702 | 2.705 |
| **683** | 1.54 | 0.855 | 0.534 | 3.832 | 2.710 | 2035.2 | 14.39 | 14.5 | 1827.3 | 2.726 | 2.730 |
| **667** | 1.53 | 0.807 | 0.505 | 3.941 | 2.752 | 1842.3 | 14.96 | 15 | 1818.0 | 2.754 | 2.755 |
| **652** | 1.53 | 0.703 | 0.463 | 3.926 | 2.746 | 2048.5 | 15.28 | 15.5 | 1840.1 | 2.782 | 2.783 |
| **639** | 1.53 | 0.574 | 0.392 | 4.146 | 2.828 | 1664.9 | 16.05 | 16 | 1807.6 | 2.815 | 2.810 |
| **626** | 1.53 | 0.393 | 0.298 | 4.147 | 2.829 | 1630.8 | 16.39 | 16.5 | 1825.9 | 2.844 | 2.842 |
| **615** | 1.53 | 0.229 | 0.194 | 4.119 | 2.818 | 3193.4 | 16.62 | 17 | 1855.0 | 2.878 | 2.873 |
| **598** | 1.53 | 0.056 | 0.056 | 1.674 | 1.533 | -255.7 | 9.30 | 17.5 | 3414.0 | 2.881 | 2.931 |

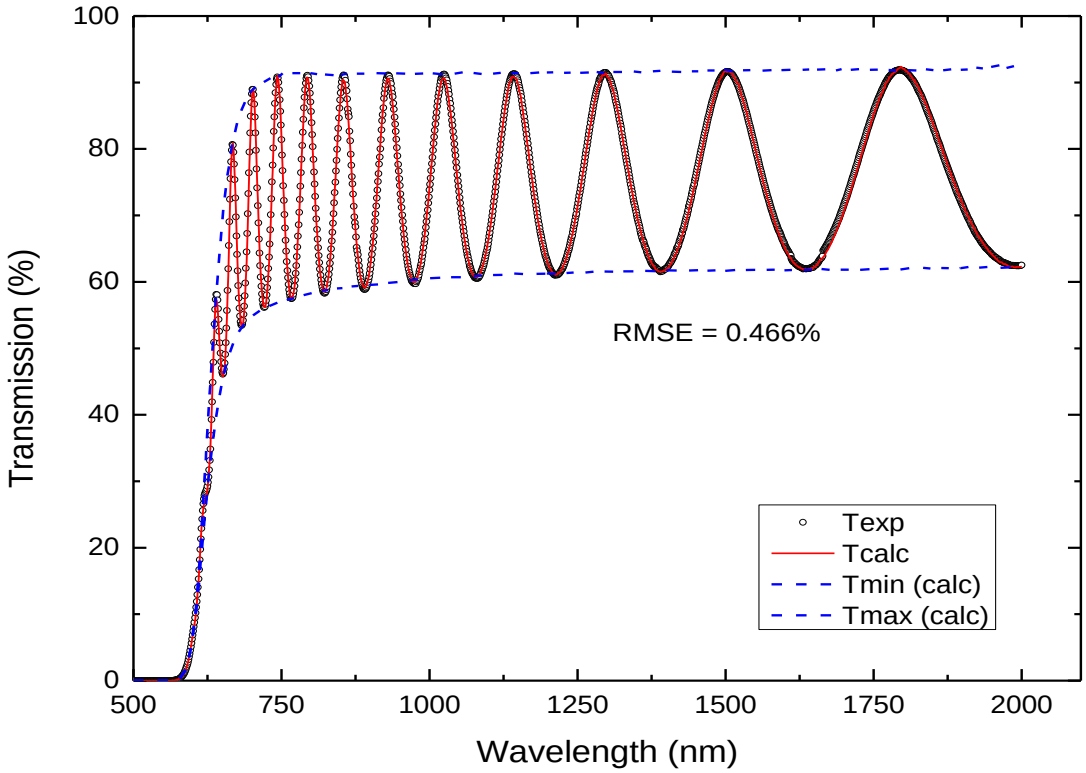


Figure 3. 6. Re-generated transmission spectrum from average thickness $\bar{d}_{new}$ of 1816.5 nm with Sellmeier coefficient terms (A = 4.32, B = 1.67 and C = 467nm), according to Table 3.2.

## 3.5 Swanepoel's non-uniform film method

### 3.5.1 Transmission of a non-uniform film

We mentioned earlier in section 3.3 that non-uniform ($d = \bar{d} \pm \Delta d$) Swanepoel transmittance is given by [47],

$$T = f(n, d, x, \Delta \mathrm{d}) \tag{3.17}$$

This implies that the previous transmittance equation for a uniform film (equation (3.7)) should be modified. This results in a slightly different formula to simulate transmission for a non-uniform film,

$$T_{\Delta d} = \frac{1}{\varphi_2 - \varphi_1} \int_{\varphi 1}^{\varphi 2} \frac{Ax}{B - Cx\cos\varphi + Dx^{\,2}} d\varphi \tag{3.18}$$

where

$$\varphi_1 = 4\pi n(d - \Delta d)/\lambda \tag{3.18a}$$

$$\varphi_2 = 4\pi n(d + \Delta d)/\lambda \tag{3.18b}$$

Now, the integral of equation (3.18) yields analytically,

$$T_{\Delta d} = \frac{\lambda}{4\pi n \Delta d} \frac{a_x}{\left(1 - {b_x}^2\right)^{1/2}} \times \left[\tan^{-1}\left(\frac{1 + b_x}{\left(1 - {b_x}^2\right)^{\frac{1}{2}}} \tan\frac{\varphi_2}{2}\right) - \tan^{-1}\left(\frac{1 + b_x}{\left(1 - {b_x}^2\right)^{\frac{1}{2}}} \tan\frac{\varphi_1}{2}\right)\right] \tag{3.19}$$

where

$$a_x = \frac{Ax}{(B + Dx^2)} \tag{3.19a}$$

$$b_x = \frac{Cx}{(B + Dx^2)} \tag{3.19b}$$

Where *A, B, C* and *D* are same as equation (3.7a) to (3.7e) as for the uniform thickness case. Although equation (3.19) is not accurate values for calculating transmission equations at minima region, it is a still good approximation to estimate the overall transmission curve. Nonetheless, the exact form of the transmission spectrum should be generated by integrating equation (3.18) numerically using Matlab.

### 3.5.2. Determination of wedge Δd in the transparent region

Assuming no absorption with $\alpha = 0$ and $x = \exp(-ad) = 1$ in the transparent region, the form of the transmission equation (3.19) becomes,

$$T_{\Delta d} = \frac{\lambda}{4\pi n \Delta d} \frac{a}{(1-b^2)^{1/2}} \times [\tan^{-1}(\frac{1+b}{(1-b^2)^{\frac{1}{2}}} \tan\frac{\varphi_2}{2}) - \tan^{-1}(\frac{1+b}{(1-b^2)^{\frac{1}{2}}} \tan\frac{\varphi_1}{2})] \quad (3.20)$$

where constants $a$ and $b$ come up by substituting $x = 1$ in equation (3.19a and 3.19b)

$$a = \frac{A}{(B+D)} \quad (3.20a)$$

$$b = \frac{C}{(B+D)} \quad (3.20b)$$

From equation (3.18b), the term $\tan(\varphi_2/2)$ in equation (3.20) can be expressed as,

$$\tan\frac{\varphi_2}{2} = \tan\frac{2\pi n(\bar{d} + \Delta d)}{\lambda} = \frac{\tan\left(\frac{2\pi n\bar{d}}{\lambda}\right) + \tan\left(\frac{2\pi n\Delta d}{\lambda}\right)}{1 + \tan\left(\frac{2\pi n\bar{d}}{\lambda}\right)\tan\left(\frac{2\pi n\Delta d}{\lambda}\right)}$$

Previously, we discussed that the basic equation of interference fringes for a uniform film was expressed as $2nd = m\lambda$ from equation (3.16) where $m$ is an integer for maxima and half integer for minima. Thus, at maxima, $\tan(\frac{2\pi n\bar{d}}{\lambda}) = 0$.

Then, at maximum, the expression for $\tan(\varphi_2/2)$ reduces to,

$$\tan\frac{\varphi_2}{2} = \tan\left(\frac{2\pi n\Delta d}{\lambda}\right)$$

Using similar arguments, the expression for $\tan(\varphi_1/2)$ in equation (3.20) at maxima becomes,

$$\tan\frac{\varphi_1}{2} = -\tan\left(\frac{2\pi n\Delta d}{\lambda}\right)$$

Substituting the two terms ($\tan\frac{\varphi_2}{2}$ and $\tan\frac{\varphi_1}{2}$) into equation (3.20) results in upper envelop $T_{\mathrm{M}\Delta\mathrm{d}}$,

$$T_{\mathbf{M}\Delta\mathrm{d}} = \frac{\lambda}{2\pi n\Delta d} \frac{a}{(1-b^2)^{1/2}} * [\tan^{-1}(\frac{1+b}{(1-b^2)^{\frac{1}{2}}} \tan\frac{2\pi n\Delta d}{\lambda})] \quad (3.21a)$$

Similarly, the lower envelope $T_{\mathrm{m}\Delta\mathrm{d}}$ is obtained by changing the sign of $b$ from equation (3.21a),

$$T_{\mathbf{m}\Delta\mathrm{d}} = \frac{\lambda}{2\pi n\Delta d} \frac{a}{(1-b^2)^{1/2}} * [\tan^{-1}(\frac{1-b}{(1-b^2)^{\frac{1}{2}}} \tan\frac{2\pi n\Delta d}{\lambda})] \quad (3.21b)$$

The maxima and minima envelopes ($T_{M\Delta d}$ and $T_{m\Delta d}$) in equation (3.21a) and (3.21b) are known from experimental envelops which were generated from Origin (this is shown as $T_M$ and $T_m$ in Table 3.3). As long as $0 < \Delta d < \frac{\lambda}{4n}$, the two unknowns ($n_1$ and $\Delta d$) with two known minima and maxima ($T_{M\Delta d}$ and $T_{m\Delta d}$) in two equations (3.21a) and (3.21b) can be solved simultaneously using an excel solver. Then, the calculated $\Delta d$ in the medium absorption region (excluding strong absorption region) is averaged and its average of wedge $\Delta\bar{d}$ is used to find the refractive index in the next section. The average of $\Delta d$ should avoid a strong absorption region, since it deviates significantly as shown in Figure 3.7 for $n_1$.

### 3.5.3 Determination of refractive index n in medium absorption region

In the weak and medium absorption region with $\alpha > 0$ ($x \neq 1$), we discussed that the integration of the transmission for the non-uniform film yields an equation (3.19) as below.

$$T_{\Delta d} = \frac{\lambda}{4\pi n\Delta d}\frac{a_x}{\left(1-{b_x}^2\right)^{1/2}} \times \left[\tan^{-1}\left(\frac{1+b_x}{\left(1-{b_x}^2\right)^{\frac{1}{2}}}\tan\frac{\varphi_2}{2}\right) - \tan^{-1}\left(\frac{1+b_x}{\left(1-{b_x}^2\right)^{\frac{1}{2}}}\tan\frac{\varphi_1}{2}\right)\right] \quad (3.19)$$

where

$$a_x = \frac{Ax}{(B+Dx^2)} \quad (3.19a)$$

$$b_x = \frac{Cx}{(B+Dx^2)} \quad (3.19b)$$

In the region of weak and medium absorption, the maximum and minimum envelops from equation (3.21a) and (3.21b) should include both $\Delta d$ and $x$, that is equation (3.22a) and (3.22b)

$$T_{\mathbf{MX}} = \frac{\lambda}{2\pi n\Delta d}\frac{a_x}{\left(1-{b_x}^2\right)^{1/2}} * \left[\tan^{-1}\left(\frac{1+b_x}{\left(1-{b_x}^2\right)^{\frac{1}{2}}}\tan\frac{2\pi n\Delta\bar{d}}{\lambda}\right)\right] \quad (3.22a)$$

$$T_{\mathbf{mx}} = \frac{\lambda}{2\pi n\Delta d}\frac{a_x}{\left(1-{b_x}^2\right)^{1/2}} * \left[\tan^{-1}\left(\frac{1+b_x}{\left(1-{b_x}^2\right)^{\frac{1}{2}}}\tan\frac{2\pi n\Delta\bar{d}}{\lambda}\right)\right] \quad (3.22b)$$

These $T_{MX}$ and $T_{mx}$ in equation (3.22a) and (3.22b) are again two equations with two unknowns, this time $n$ and $x$. When $x$ be in the range $0 < x < 1$, these $n$ and $x$ can be solved simultaneously by using $\Delta\bar{d}$ from equation (3.21) and the experimental envelopes ($T_M$ and $T_m$) generated from Origin. This can be done in an excel solver. The obtained $n$ is denoted as $n_2$ in Table 3.3.

In here, $n_2$ was calculated from equation (3.22) using obtained $\Delta\bar{d}$ from equation (3.21), and then these $n_2$ at every extremum were fitted into Sellmeier dispersion relation, to extrapolate $n$ into the strong absorption region, which is same procedure as the uniform film case.

$$\text{Sellmeier dispersion form: } n_{\text{fit}} = \sqrt{A + \frac{B\lambda^2}{\lambda^2 - C^2}}$$

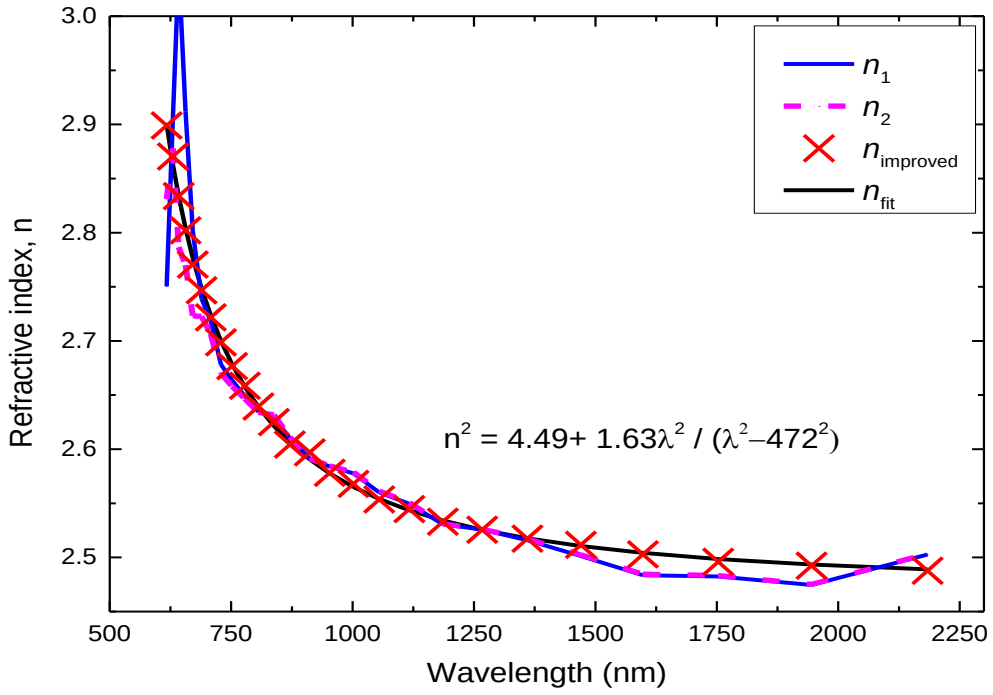


Figure 3. 7. The spectral dependence of the refractive index of pure a-Se non-uniform film. The $n_{\text{fit}}$ value is obtained from the fit of the Sellmeier dispersion with coefficients (A = 4.49, B = 1.63 and C = 472 nm) of $n_{\text{measured}}$. (The $n_1$ and $n_2$ are from equations (3.21) and (3.22) respectively)

### 3.5.4 Determination of thickness

We earlier mentioned in section (3.4.5) that in uniform film, the determination of the thickness can be derived from the integerference fringe equation, that is, $2nd = m\lambda$. This applies to the thickness of non-uniform film.

$$d_1 = \frac{\lambda_{m+1}\lambda_m}{2(\lambda_m n_{m+1} - \lambda_{m+1} n_m)} \tag{3.12}$$

where $n_m$, and $n_{m+1}$ are the refractive indices $n_2$ (obtained from equation (3.22a) and (3.22b)) at two adjacent maxima (or minima) at $\lambda_m$ and $\lambda_{m+1}$.

### 3.5.5 Determination of absorption coefficient

The $x$ (or $\alpha$) obtained from equations (3.22a) and (3.22b) is not accurate in the strong absorption region. The derivation of $\alpha$ is done in the same way as in the case of the uniform film. We add reciprocals of equations (3.8a) and (3.8b) of uniform film to solve for $x$,

$$\frac{1}{T_{\mathrm{M}}}+\frac{1}{T_{\mathrm{m}}}=\frac{2(B+Dx^2)}{Ax} \tag{3.23}$$

Simplifying the equation (3.23) results in,

$$(T_i D)x^2 - Ax + T_i B = 0 \tag{3.24}$$

Solving for $x$ results in,

$$x = \frac{A-(A^2-4T_{\mathrm{i}}^2BD)^{1/2}}{2T_{\mathrm{i}}D} \tag{3.25}$$

where $A$, $B$, $C$ and $D$ are the same as in equation (3.3) and $T_{\mathrm{i}}$ represents a curve passing through the inflection points of the fringes, which must be determined from minima and maxima envelopes in the experimental transmission spectrum.

$$T_{\mathrm{i}}=\frac{2T_{\mathrm{M}}T_{\mathrm{m}}}{T_{\mathrm{M}}+T_{\mathrm{m}}} \tag{3.25a}$$

Thus, finally, we have,

$$\alpha=\frac{-\ln x}{\bar{d}}$$

As same as the uniform film, determination of $\boldsymbol{\alpha}$ must be done in final step after optimizing all optical constants including $n$ and $\bar{d}$ and after fitting $n$ into dispersion form.

### 3.5.6 Improvement in the extraction of optical constants

The improvement of optical constants follows the same protocols of uniform film as described in Section 3.4.7. This time, we improve optical constants $n_2$ and $d_1$ instead of $n_{crude}$ and $d_{crude}$ by performing steps from (3.16a) to (3.16f). However, we use equation (3.18) instead of (3.16e) to re-generate the transmission spectrum. We re-iterate steps (3.16a) to (3.16f) until the RMSE reaches its minimum.

$$T_{\Delta d,calc} = \frac{1}{\varphi_2 - \varphi_1}\int_{\varphi 1}^{\varphi 2} \frac{Ax}{B - Cx\cos\varphi + Dx^{\,2}}\,d\varphi \tag{3.18}$$

However, since the integral of transmission for non-uniform film relies on the values on wedge $\Delta d$ and not only thickness $\bar{d}$, it should involve improvement on the wedge $\Delta d$, as well as average thickness $\bar{d}$. Therefore, the determination of RMSE depends on two degrees of freedoms: the average thickness $\bar{d}$ and wedge $\Delta d$. The iteration method in Matlab evaluates 1755.8nm and 10.7nm as ideal average thickness $\bar{d}$ and ideal wedge $\Delta\bar{d}$ , respectively, with a minimum RMSE of 0.64%.

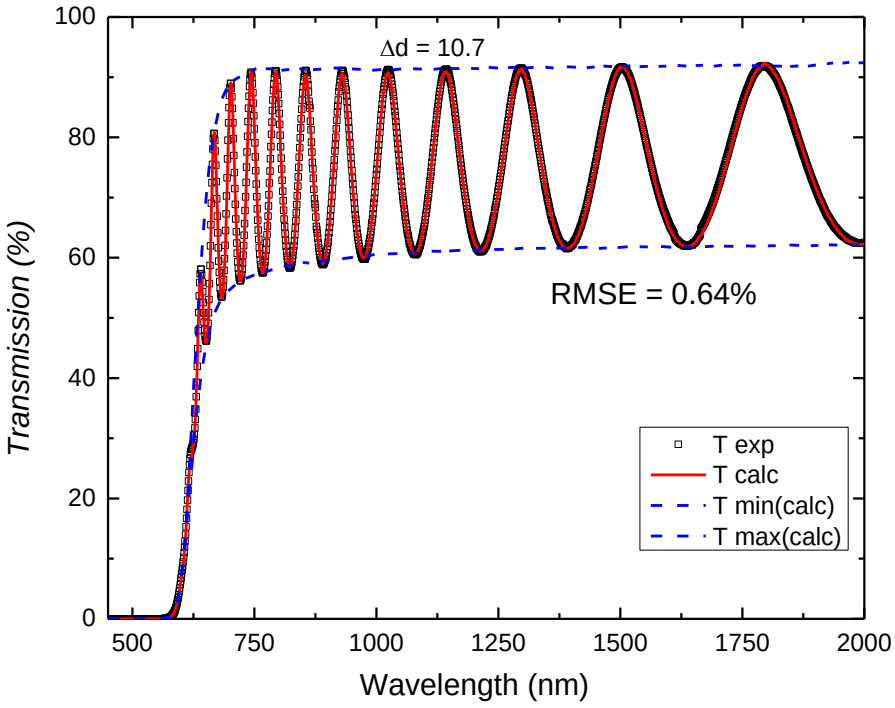


Figure 3. 8. Re-generated transmission spectra of a pure a-Se non-uniform film obtained from $\overline{d_2}$ = 1755.8 nm and $\Delta\bar{d}$ = 10.7 nm according to Table 3.3.

Table 3. 3. Optical parameters of non-uniform pure a-Se film, obtained from $\overline{d}$ of 1755.8nm with $\Delta\overline{d}$ = 10.7 with 0.64% RMSE, and Values of $\lambda_{ext}$, $s$, $T_M$ and $T_m$ are for the spectrum of figure 3.8. Calculation of $n_1$, $\Delta d$ and $n_2$, $x$ and $d_1$, $d_2$ and $n_3$, $n_{fit}$. ($n_1$ and $\Delta d$ from equation (3.21), $n_2$ and $x$ from equation (3.22). $d_1$ from equation (3.12). $m_{crude}$ and $m$ from equation (3.16a). $d_2$ from equation (3.16b). $n_3$ from equation (3.16c). $n_{fit}$ from equation (3.16d)). Sellmeier coefficient terms for $n_{fit}$ is: A = 4.49, B = 1.62 and C = 472 nm.

| $\lambda_{ext}$ nm | $s$ | $n_1$ | $\Delta d$ nm | $n_2$ | $x$ | $d_1$ nm | $m_{crude}$ | $m$ | $d_2$ nm | $n_3$ | $n_{fit}$ |
|---|---|---|---|---|---|---|---|---|---|---|---|
| **2184** | 1.52 | 2.503 | 0.0 | 2.503 | 1 | | 4.1 | 4 | 1744.9 | 2.488 | 2.489 |
| **1945** | 1.51 | 2.475 | 0.2 | 2.475 | 1 | | 4.5 | 4.5 | 1768.0 | 2.492 | 2.493 |
| **1753** | 1.52 | 2.482 | 0.0 | 2.483 | 1 | 1849.0 | 5.0 | 5 | 1764.8 | 2.496 | 2.499 |
| **1598** | 1.52 | 2.484 | 0.0 | 2.485 | 1 | 1772.0 | 5.5 | 5.5 | 1768.7 | 2.503 | 2.504 |
| **1470** | 1.52 | 2.501 | 0.0 | 2.502 | 1 | 1749.9 | 6.1 | 6 | 1762.3 | 2.512 | 2.511 |
| **1360** | 1.53 | 2.516 | 2 | 2.517 | 1 | 1688.7 | 6.6 | 6.5 | 1755.9 | 2.517 | 2.518 |
| **1267** | 1.53 | 2.526 | 8.8 | 2.526 | 1 | 1715.7 | 7.1 | 7 | 1755.5 | 2.526 | 2.525 |
| **1186** | 1.53 | 2.531 | 9.2 | 2.531 | 1 | 1765.2 | 7.6 | 7.5 | 1757.2 | 2.533 | 2.534 |
| **1117** | 1.54 | 2.549 | 6.9 | 2.551 | 1 | 1725.7 | 8.1 | 8 | 1751.7 | 2.545 | 2.543 |
| **1055** | 1.54 | 2.560 | 6.9 | 2.561 | 1 | 1702.6 | 8.6 | 8.5 | 1750.6 | 2.554 | 2.554 |
| **1002** | 1.55 | 2.578 | 7.9 | 2.579 | 1 | 1723.6 | 9.2 | 9 | 1748.5 | 2.568 | 2.565 |
| **953** | 1.54 | 2.584 | 9.4 | 2.585 | 1 | 1758.8 | 9.7 | 9.5 | 1751.4 | 2.578 | 2.578 |
| **912** | 1.53 | 2.591 | 11 | 2.591 | 1 | 1868.8 | 10.1 | 10 | 1759.9 | 2.597 | 2.591 |
| **871** | 1.54 | 2.610 | 8.8 | 2.611 | 1 | 1749.4 | 10.7 | 10.5 | 1751.2 | 2.604 | 2.606 |
| **838** | 1.55 | 2.630 | 7.1 | 2.632 | 1 | 1670.4 | 11.2 | 11 | 1751.3 | 2.625 | 2.621 |
| **806** | 1.55 | 2.635 | 7.5 | 2.634 | 1 | 1851.5 | 11.6 | 11.5 | 1759.5 | 2.640 | 2.639 |
| **778** | 1.54 | 2.649 | 8.3 | 2.647 | 1 | 1913.7 | 12.1 | 12 | 1763.8 | 2.659 | 2.658 |
| **752** | 1.54 | 2.664 | 9.4 | 2.658 | 0.99 | 1874.4 | 12.6 | 12.5 | 1768.2 | 2.677 | 2.678 |
| **729** | 1.53 | 2.678 | 10 | 2.670 | 0.99 | 1917.0 | 13.0 | 13 | 1774.7 | 2.699 | 2.700 |
| **708** | 1.54 | 2.718 | 10.7 | 2.706 | 0.98 | 1736.7 | 13.6 | 13.5 | 1765.8 | 2.722 | 2.723 |
| **689** | 1.54 | 2.739 | 0.0 | 2.723 | 0.96 | 1729.4 | 14.1 | 14 | 1771.4 | 2.747 | 2.749 |
| **671** | 1.53 | 2.802 | 19.3 | 2.723 | 0.91 | 2119.5 | 14.5 | 14.5 | 1786.4 | 2.771 | 2.777 |
| **656** | 1.53 | 2.912 | 22.6 | 2.770 | 0.84 | 1845.4 | 15.0 | 15 | 1776.1 | 2.802 | 2.804 |
| **642** | 1.53 | 3.044 | 26.1 | 2.787 | 0.72 | 1772.5 | 15.5 | 15.5 | 1785.5 | 2.834 | 2.834 |
| **630** | 1.53 | 2.905 | 35.5 | 2.878 | 0.56 | 1448.0 | 16.3 | 16 | 1751.3 | 2.870 | 2.863 |
| **617** | 1.53 | 2.750 | 47.9 | 2.831 | 0.34 | 2016.7 | 16.3 | 16.5 | 1798.0 | 2.899 | 2.900 |

## 3.6 Error analysis of all optical parameters

It is important to analyze errors in the Swanepoel technique for the precise extraction of optical constants in the experiment, since there are a lot of errors associated with a sample such as damaged spot, dust, substrate, aging, room light, or stimuli and with an instrument, related to noise or signal, scattering, or an ambient temperature.

In this set-up, the nine measurements were made at different spots of the same a-Se film on the same date to estimate the experimental errors associated with one film. We minimized aging effects on the optical properties by taking measurement in the same day. The sample was at the room temperature, covered with the aluminum foil to reduce any illumination. Table 3.4 is the mean standard deviation of errors. The relative percent errors for $n$ was 0.091%, for $Eg_U$ was 0.04%, for $Eg_T$ was 0.03%, for $\Delta E$ was 1.0%, for $E_o$ was 0.25%, and for $E_d$ 0.4%. This relative error was used as an experimental error for X-ray irradiation, heat induced, alloying and doping effects to check and compare if induced changes are within error or out of errors, and therefore if the effects are real or false.

Table 3. 4. Analysis of a-Se alloyed with 0.5% As film in terms thickness $d$, refractive index $n$ and two optical band gaps $Eg_T$ and $Eg_U$, using nine different measurements on different spots on the film surface.

| Trial # | $d$ (nm) | $n$ (at 2000nm) | $Eg_U$ (eV) | $Eg_T$ (eV) | $\Delta E$ (meV) | $E_o$ (eV) | $E_d$ (eV) |
|---|---|---|---|---|---|---|---|
| 1st | 1838.42 | 2.46407 | 2.0458 | 2.03499 | 66.012 | 3.7769 | 18.460 |
| 2nd | 1778.29 | 2.46142 | 2.04740 | 2.03705 | 67.017 | 3.7693 | 18.355 |
| 3rd | 1815.09 | 2.46212 | 2.04573 | 2.03601 | 65.677 | 3.7874 | 18.488 |
| 4th | 1692.58 | 2.45850 | 2.04634 | 2.03668 | 66.266 | 3.7811 | 18.384 |
| 5th | 1824.62 | 2.46120 | 2.04592 | 2.03556 | 65.506 | 3.7928 | 18.505 |
| 6th | 1799.01 | 2.46513 | 2.04684 | 2.03629 | 66.675 | 3.7884 | 18.530 |
| 7th | 1837.41 | 2.46545 | 2.04468 | 2.03739 | 64.866 | 3.7673 | 18.383 |
| 8th | 1801.81 | 2.46452 | 2.04591 | 2.03575 | 65.897 | 3.7787 | 18.483 |
| 9th | 1705.70 | 2.46310 | 2.04543 | 2.03593 | 65.658 | 3.7935 | 18.526 |
| average | n/a | 2.46284 | 2.04600 | 2.03618 | 65.953 | 3.78 | 18.457 |
| S.D. | n/a | 0.00225 | 0.00079 | 0.00065 | 0.00064 | 0.0096 | 0.0709 |
| Relative% error | n/a | 0.091% | 0.039% | 0.032% | 0.97% | 0.254% | 0.384% |
| | | ±0.00225 | ±0.0008 | ±0.0007 | ±0.0006 | ±0.010 | ±0.071 |

# Chapter 4. Experimental Procedure

## 4.1 Introduction

This chapter provides an outline for the experimental protocols and instruments used to fabricate films and to acquire the experimental data. Section 4.2 explains the thermal evaporation technique used to fabricate a thin film. The next section explains an X-ray faxitron cabinet system used to expose selenium films and ion chamber to acquire exposure. Section 4.4, 4.5 and 4.6 discuss the experimental and theoretical techniques to calculate dose. In section 4.7, UV-visible spectrophotometer is described for the analysis of transmission spectrum.

## 4.2 Thin film deposition by thermal evaporation technique

The vacuum chamber was pumped down to $10^{-6}$ Torr to remove impurities. Vitreous selenium pellets were placed in a molybdenum boat inside a Norton NRC3117 stainless steel vacuum system. For starting material, four types of glassy pellets were used: (1) nominally pure (99.999%) a-Se, (2) a-Se alloyed with 0.5 wt% of As, (3) a-Se alloyed with 6 wt% of As, and (4) a-Se alloyed with 6 wt% of As and doped with 140 ppm of Cs. At this state, the shutter is closed to prevent any Se vapour condensing on the substrates. The shutter is used to start and terminate the deposition process. The boat containing Se pellets is heated until starting to melt and evaporate. The boat temperature $T_b$ is set around 170 – 230 °C range, depending on the melting temperature of substance used. The temperature of substrate $T_s$ is set to stay around 40 – 81 °C, near the glass transition temperature $T$g of substance used. The $T_b$, $T_s$ and evaporation rate all must be stabilized to prepare steady deposition condition [58].

Now when the system is stabilized, the shutter is opened, the Se vapor from the heated molybdenum boat reaches the surface of the substrates and condenses on the substrate surface to form a continuous film, changing from vapor to liquid state. The deposition rate of a-Se was

monitored by a quartz crystal oscillator, “Sigma Instruments SQM-160 rate monitor”, with a pinhole to control deposited film thickness.

When the desired thickness has been reached, the shutter is closed, the current passing through the boat is turned off, the chamber temperature goes down, the pressure comes back to the original, and then the films coated on top of substrates are removed [58, 18]. The a-Se film remains at the substrate temperature until evaporation processes have ended. The thickness of the films ranges from 1.81 μm to 3.39 μm. Table 4.1 is the all the features and conditions in which all films were fabricated. Figure 4.1 is a typical temperature- time profile (temperature of the boat $T_b$ and temperature of the substrate $T_s$) from the start to end as a function of time. However, figure below is not necessarily the exact profile used in this work. Figure 4.2 below is the Norton NRC 3117 vacuum system to be used for vacuum deposition.

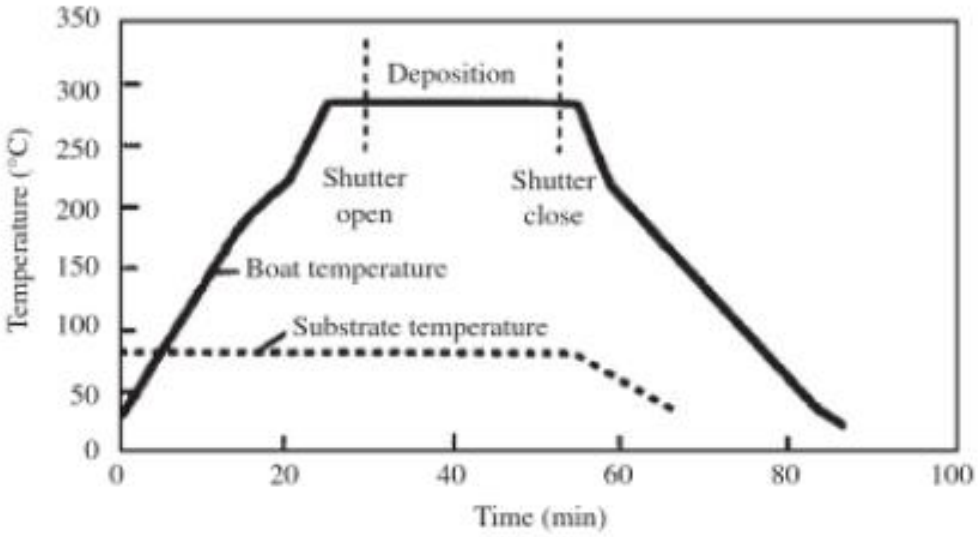


Figure 4. 1. Typical boat and substrate temperature vs. time profile. During the deposition, boat and substrate temperature are constantly controlled and monitored (after [25]).

Table 4. 1. Typical fabrication conditions for the thermal deposition of a-Se (pure/0.5% As/6% As/6% As + Cs) films during the deposition, which was used for X-ray irradiation experiments. *P* is chamber pressure, $T_b$ is the boat temperature, $t_{evap}$ is the time duration of deposition, *Ts* is the substrate temperature and *d* is the thickness of film.

| Date | Run # | Sample | $P$ ($\times 10^{-6}$) Torr | $T_b$ °C | $t_{evap}$ sec | $T_s$ °C | $d$ µm |
|---|---|---|---|---|---|---|---|
| 02/24/2016 | R789 | Pure a-Se | 1.9 | 172 | 30 | 43 | 1.81 |
| 02/26/2016 | R790 | Se-0.5% As | 1.8 | 181 | 35 | 51 | 1.49 |
| 07/06/2016 | R810 | Se-6% As | 3.0 | 219 | 80 | 71 | 3.39 |
| 03/24/2016 | R796 | 6% As + Cs 140ppm | 2.5 | 195 | 60 | 60 | 3.35 |
| 11/16/2016 | R818 | 6% As + Cs 140ppm | 2.8 | 216 | 60 | 81 | 2.99 |

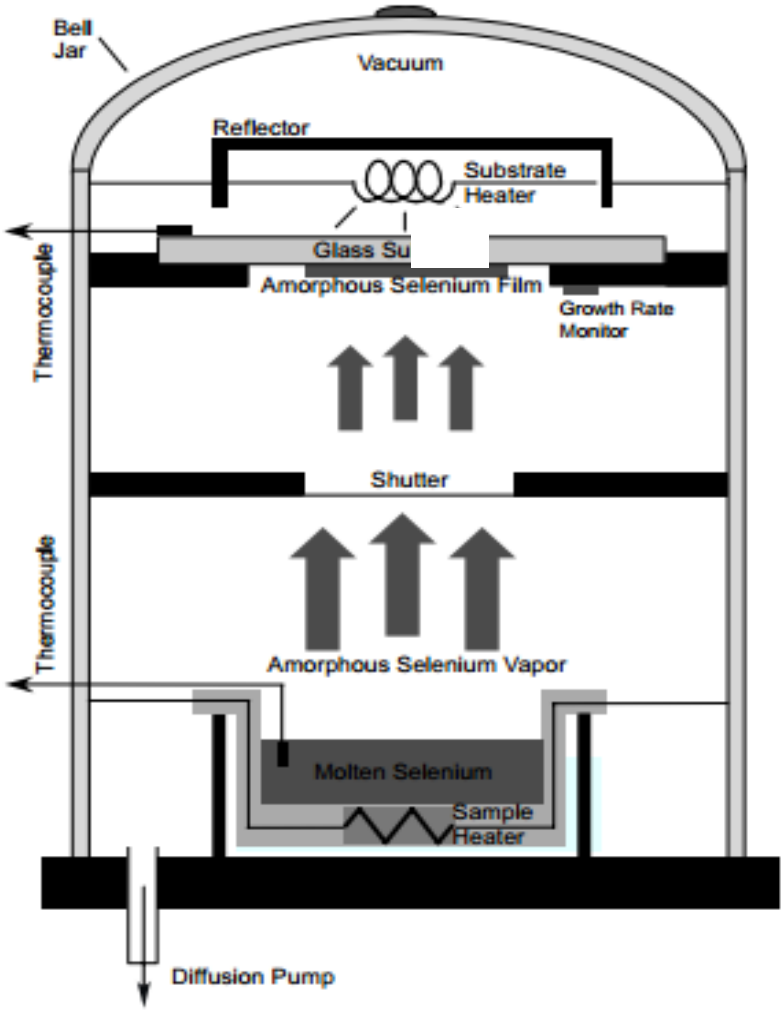


Figure 4. 2. A schematic of the evaporation assembly inside the vacuum chamber (after [43]).

## 4.3 X-ray Faxitron chamber

The equipment used to expose the samples to X-rays is the Faxitron Cabinet X-ray system as shown in Figure 4.3 below. The Faxitron Cabinet X-ray system has a tungsten target tube with a beryllium window to heat up and release a wide range of X-ray energy. The operating anode voltage ranges from 30 kVp up to 140 kVp. It has a maximum irradiation time of 60 minutes.

Before irradiation, the Faxitron went through two warm-up cycles (zero and 30 kVp) in 5 minutes interval for 30 kVp use, and four warm-up cycles (zero, 30, 60, and 70 kVp) in 5 minutes interval for 70 kVp use. All a-Se films were irradiated for the same duration of 20 minutes and were placed at the very top position, where there is a 303mm from the X-ray source to the film, when in use.

Figure 4. 3. Faxitron Cabinet X-ray system (after [66]).

## 4.4 Dose calculation

When X-rays pass through an object or body, three phenomena can happen with each photon: i) it penetrates objects without interaction, ii) it is completely absorbed by depositing its energy, or iii) it is scattered by spreading its energy away from the original direction of the beam and depositing a part of the energy. There are two types of major interactions in which photons deposit their energy with electrons in the medium: the photoelectric effect and Compton scattering. In the photoelectric effect, the electron is ejected from an atom and photon energy is completely absorbed by the electron. Most of its energy is used to overcome the binding energy of the electron and the rest is converted to kinetic energy of the electron. In Compton scattering, some portion of the photon's energy is absorbed by an electron, but the other portion of the energy is carried by the photon which is deflected in a different direction [67].

The dose in unit of Gray is defined as the absorbed energy (J) per unit mass (kg) of the object of interest (1 Gy = 1 J/kg): $D$ (dose) = $E_{\text{absorbed}}$ /$M$ (mass). In the unit of Roentgen, one Roentgen (R) is equivalent to depositing 0.00877J per kg of air. Therefore, 1 R = 0.00877Gray. The calculation of dose ($D$) requires absorbed energy $E_{\text{absorbed}}$, which depends on the mass attenuation coefficient $\mu/\rho$, mass energy absorption coefficient $\mu_{\text{en}}/\rho$, quantum efficiency 1-exp (-$\mu L$) and fluence $\Phi(E)$.

The actual absorbed energy $E_{\text{absorbed}}$ for each of photons with its energy $E$ is given by [3],

$$E_{\text{absorbed}} = E\frac{(\mu_{\text{en}}/\rho)}{(\mu/\rho)} \tag{4.1}$$

where $\mu_{\text{en}}/\rho$ is the mass energy absorption coefficient of the medium and $\mu/\rho$ is the mass attenuation coefficient. The energy absorption coefficient $\mu_{\text{en}}$ is the fraction of coefficient $\mu$, transferred from the incident photons to the kinetic energy of electrons (i.e. through photoelectric and Compton interactions) and lost by radiation (Bremsstrahlung) as electrons decelerate. The linear attenuation coefficient $\mu$ which describes the fraction of an x-ray beam lost by absorbing or scattering per unit thickness of the object (in this case, photoconductor) depends on energy $E$, density $d$, and atomic number $Z$, that is $\mu = \mu\ (E, d, Z)$.

The linear attenuation coefficient $\mu(E)$ at photon energy $E$ is given by [3],

$$\mu(E) = -\frac{1}{N(E)} \cdot \frac{dN(E)}{dz} \tag{4.1a}$$

where $N(E)$ is the number of photons each with energy $E$. If we integrate equation (4.1a), the number of photons at $z$ becomes

$$N = N_0 \exp(-\mu z) \tag{4.1b}$$

Then, the fraction $(N_o(E)\text{-}N(E))/N_o(E))$ of incident photons that are attenuated (i.e. absorbed or scattered) by a photoconductor depends on the linear attenuation coefficient $\mu$ of the photoconductor and its thickness $L$.

$$\eta_Q = 1 - \exp(-\mu L) \tag{4.2}$$

which is known as attenuated fraction or quantum efficiency $\eta_Q$.

By combining equations (4.1) and (4.2), the actual energy absorbed up to a maximum $E_{max}$ is given by [3],

$$E_{absorbed} = \int_0^{E_{max}} \Phi(E) E \frac{\mu_{en}/\rho}{\mu/\rho} [1 - \exp(-\mu L)] dE \tag{4.3}$$

where $\Phi(E)$ is the photon concentration per unit area per unit energy, the energy spectrum of fluence, which is shown in figure 4.6. The $\mu/\rho$, $\mu_{en}/\rho$, $\Phi(E)$ and $1\text{-}\exp(-\mu L)$ are all a function of photon energy, so the absorbed dose $(E_{absorbed}/M)$ is a function of photon energy.

An ideal X-ray fluence $\Phi(E)$ was obtained from the Siemens website [68]. The ideal fluence needs to be adjusted to fit the exposure conditions. Since we do not know the experimental X-ray tube fluence used in the laboratory, we need to estimate it by finding a calibration factor. This can be done by measuring exposure rates in air $D_{air\ exp}$ (i.e. 30 kVp) from the ion chamber and then dividing it by the ideal dose in air $D_{air\ ideal}$ (i.e. 30 kVp). This factor $(D_{air\ exp}/ D_{air\ ideal})$ is used as a calibration factor to normalize the ideal X-ray fluence to the lab condition as given below,

$$\Phi(E)_{exp} = \frac{D_{air,exp}}{D_{air,ideal}} \times \Phi(E)_{ideal} \tag{4.4}$$

where $\Phi(E)_{\text{ideal}}$ is the simulated X-ray fluence of tungsten, $\Phi(E)_{\text{exp}}$ is the experimental X-ray fluence and the $D_{\text{air, ideal}}$ and $D_{\text{air, exp}}$ are given by,

$$D_{air,ideal} = \frac{E_{\text{absorbed, air}}}{M_{air}} = \int_0^{E_{\max}} \Phi(E) E \frac{\mu_{\text{en,air}} / \rho_{air}}{\mu_{air} / \rho_{air}} [1 - \exp(-\mu_{air} L_{air})] dE / M_{air} \qquad (4.4a)$$

$$D_{\text{air,exp}} = R \qquad (4.4b)$$

The *ideal* dose in air ($D_{\text{air, ideal}}$) in equation 4.4a refers to a dose with an *ideal* fluence $\Phi(E)_{\text{ideal}}$ and the *experimental* dose in air ($D_{\text{air, exp}}$) in equation 4.4b refers to a dose with an *experimental* fluence $\Phi(E)_{\text{exp}}$. In equation 4.4b, $R$ is the readout from a dosimeter in units of Roentgen.

Once we know the experimental fluence $\Phi(E)_{\text{exp}}$ from the equation (4.4), then we can obtain the deposited dose in selenium, by substituting experimental fluence $\Phi(E)_{\text{exp}}$ into $\Phi(E)$ of equation (4.3) as follows,

$$D_{Se,\text{exp}} = \frac{E_{\text{absorbed, Se}}}{\text{M}_{\text{Se}}} = \int_0^{E_{\max}} \left(\frac{D_{air,\text{exp}}}{D_{air,ideal}} \times \Phi(E)_{ideal}\right) E \frac{\mu_{\text{en},Se} / \rho_{Se}}{\mu_{Se} / \rho_{Se}} [1 - \exp(-\mu_{Se} L_{Se})] dE / M_{Se}$$

$$= \frac{D_{air,\text{exp}}}{D_{air,ideal}} \times \int_0^{E_{\max}} \Phi(E)_{ideal} E \frac{\mu_{\text{en},Se} / \rho_{Se}}{\mu_{Se} / \rho_{Se}} [1 - \exp(-\mu_{Se} L_{Se})] dE / M_{Se}$$

Therefore, the absorbed dose in selenium is,

$$D_{Se,\text{exp}} = D_{air,\text{exp}} \times \frac{D_{Se,ideal}}{D_{air,ideal}} \qquad (4.5)$$

where

$$D_{Se,ideal} = \int_0^{E_{\max}} \Phi(E)_{ideal} E \frac{\mu_{\text{en},Se} / \rho_{Se}}{\mu_{Se} / \rho_{Se}} [1 - \exp(-\mu_{Se} L_{Se})] dE / M_{Se} \qquad (4.5a)$$

The measurement of dose in air ($D_{\text{air, exp}}$) in equation (4.4b) was done by using a calibrated dosimeter in Section 4.5. Section 4.6 discusses the method to obtain the ideal dose in air and selenium and each of parameters including $\Phi(E)_{\text{ideal}}$, $\mu/\rho$ and $\mu_{\text{en}}/\rho$, and sample parameters such as thickness and density. Table 4.2 below is the experimental dose of selenium with different compositions.

Table 4. 2. Absorbed dose in 20 minutes for listed samples which were placed at shelf No.8 (303cm) in the X-ray chamber, using total incident dose 15.93 Gy of air at 30 kVp in 20 minutes.

| Sample types | Thickness of film (μm) | Dose (Gy) |
|---|---|---|
| Pure a-Se | 1.815 | 949 |
| a-Se:0.5% As | 1.797 | 950 |
| a-Se: 6% As | 3.398 | 934 |
| a-Se: 6% As +140ppm Cs | 2.994 | 938 |

## 4.5 Experimental air dose and dose measurement system

The device used to measure exposure rate is the Keithley 35050 dosimeter, and the device used to detect the exposure of air is Keithley Ion Chamber, as shown in Figure 4.4 below. The ion chamber collects ionized charges of air in the whole volume of the enclosure under X-rays and measures the exposure in unit of Roentgen. For instance, 1 Roentgen produces $2.58\times10^{-4}$ Coulombs of ionization per kg of air. Since the amount of ionization (Coulombs) produced by X-rays is converted to the energy released in the air, the ion chamber is used to measure air dose [69].


Figure 4. 4. Keithley 35050 dosimeter (left) and the air-filled detection device, the Keithley ion chamber (right) (after [66]).

The ion chamber features a volume of 15 $cm^3$ and a thickness of 1.2 cm. The Keithley dosimeter has been pre-calibrated with a calibration factor of 0.7 Roentgen/volt. A digital voltmeter was attached to the Keithley dosimeter to read the output voltage and this was converted from voltage

to Roentgen using a calibration factor. The ion chamber and dosimeter were placed inside the X-ray chamber at each shelf level to measure exposure rates of air in voltage and second at each shelf. However, the rates from levels 5 to 8 were saturated ("n/a" in bare rate). This problem was resolved by finding its correction factor. The correction factor was found by bare rate divided by reduced rates of air ("*filtered rate*" in Table 4.3) in the ion chamber which was measured by covering with a piece of aluminum sheet (8.2mm) per minutes. Then, this correction factor (34.36) is multiplied with the filtered rate to convert it back to "*corrected* bare rate" at each shelf level, which then is converted to R/m using 0.7 R/V, and converted to Gy/m using 0.00877 Gy/R.

Since all the experimental samples were placed at Shelf No. 8 to be exposed, the incident rate of 2.27 Gy/min was used to find the deposited dose in Se ($D_{\text{Se, exp}}$) for the 70 kVp exposure. For the 30 kVp exposure, incident rate of 0.797 Gy/min was used.

Table 4. 3. The incident dose rate in air at 70 kVp by using a correction factor 34.36 (The correction factor was found by dividing bare rate of 98.28 V/m from filtered rate of 2.86 V/m at shelf number of two).

| Shelf No. | Distance to source (mm) | Bare rate (V/m) | Filtered rate (V/m) | *Corrected* bare rate (V/m) | Corrected bare rate (R/m) | Corrected bare rate (Gy/m) |
|---|---|---|---|---|---|---|
| 8 | 304 | n/a | 10.75 | 369.41 | 258.59 | 2.27 |
| 7 | 356 | n/a | 7.61 | 261.51 | 183.06 | 1.61 |
| 6 | 406 | n/a | 6.2 | 213.05 | 149.14 | 1.31 |
| 5 | 457 | n/a | 4.93 | 169.41 | 118.59 | 1.04 |
| 4 | 508 | 148.90 | 4.05 | 139.17 | 97.42 | 0.85 |
| 3 | 559 | 122.67 | 3.33 | 114.43 | 80.10 | 0.70 |
| 2 | 610 | 98.28 | 2.86 | 98.28 | 68.80 | 0.60 |
| 1 | 669 | 84.13 | 2.59 | 89.00 | 62.30 | 0.55 |

## 4.6 Calculation of ideal dose in air and selenium

We had looked up the equation of theoretical dose of air $D_{\text{air, ideal}}$ as below,

$$D_{air,ideal} = \frac{E_{\text{absorbed, air}}}{M_{air}} = \int_0^{E_{\max}} \Phi(E) E \frac{\mu_{\text{en,air}} / \rho_{air}}{\mu_{air} / \rho_{air}} [1 - \exp(-\mu_{air} L_{air})] dE / M_{air} \qquad (4.4a)$$

$$D_{Se,ideal} = \int_0^{E_{\max}} \Phi(E)_{ideal} E \frac{\mu_{en,Se} / \rho_{Se}}{\mu_{Se} / \rho_{Se}} [1 - \exp(-\mu_{Se} L_{Se})] dE / M_{Se} \quad (4.5a)$$

The calculation of the ideal dose in air and Se was performed by downloading the energy spectrum of tungsten X-ray fluence $\Phi(E)_{ideal}$ at 30 kVp and 70 kVp from Siemens [68] and its mass coefficients $\mu/\rho$ and $\mu_{en}/\rho$ from NIST website [70]. The density of air was obtained from the NIST [70] as $\rho_{air} = 1.205 \times 10^{-3}$ g/cm$^3$ and its thickness $L_{air}$ was taken as the length of the ion chamber (i.e. $L$ = 1.2cm), and the density of amorphous selenium was taken as $\rho_{Se}$ = 4.3 g/cm$^3$ with its thickness $L_{se}$ ranging from 1 µm to 3 µm. The mass of air $M_{air}$ and Selenium $M_{Se}$ was calculated by multiplying its density $\rho$ (g/cm$^3$) by its thickness $L$, resulting in units of gram per cm$^2$. The units of mass coefficients is cm$^2$/g, and of energy is keV and of fluence is cm$^{-2}$. The energy spectra of ideal X-ray photon fluences at 30 and 70 kVp are shown in Figure 4.5 and the energy spectra of mass coefficients in air and selenium are shown in Figure 4.6. The ideal dose in air ($D_{air, ideal}(E)$) and ideal dose in selenium ($D_{Se, ideal}(E)$) as a function of energy were shown in Table 4.4 and plotted in Figure 4.7. The experimental absorbed dose in selenium ($D_{Se, exp}(E)$) was plotted as a function of energy in Figure 4.8.

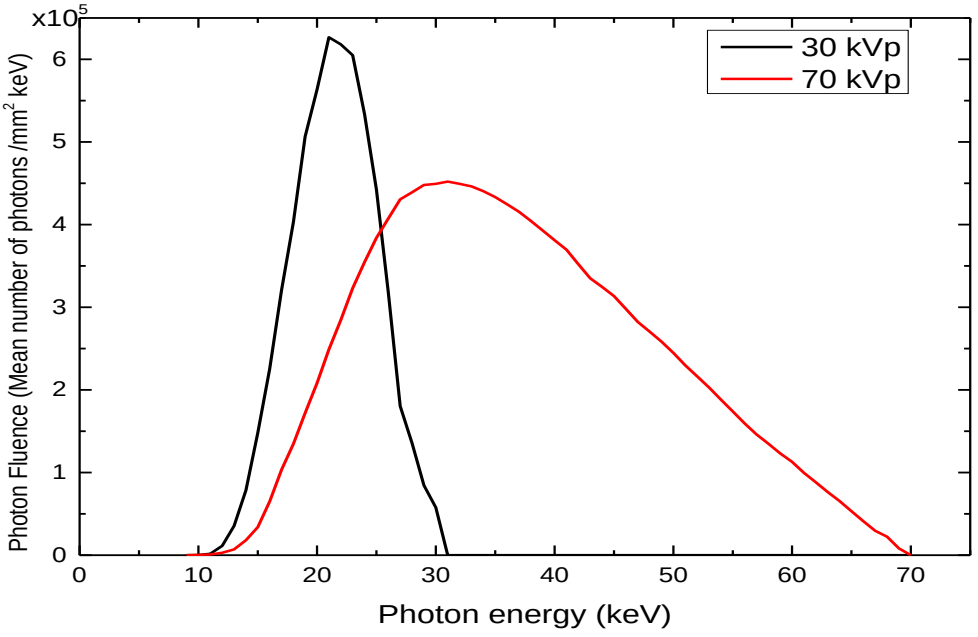


Figure 4. 5. The simulated X-ray spectrum of fluence at 30 kVp and 70 kVp (from Siemens [68]).

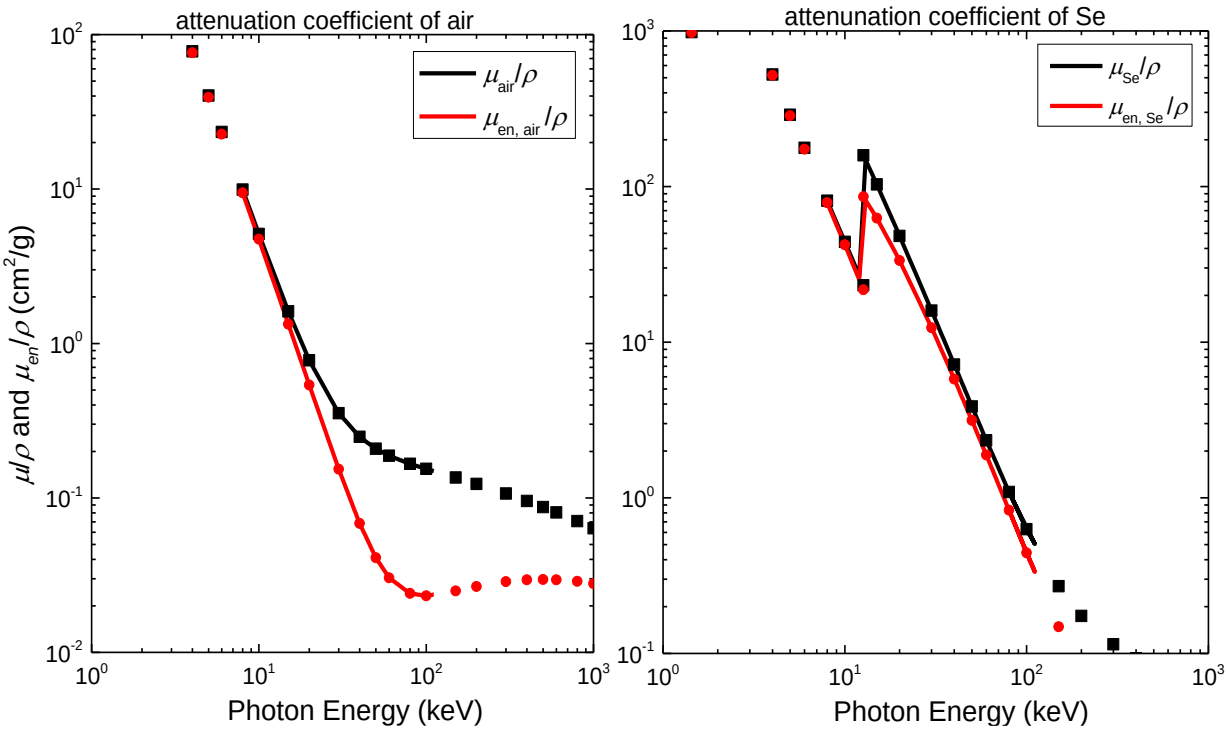


Figure 4. 6. Mass Attenuation coefficients $\mu/\rho$ (black) and mass energy absorption coefficients $\mu_{en}/\rho$ (red) of air (left) and Se (right). The data point is obtained from NIST [70], and linear curve data was obtained by taking logarithmic interpolation both in photon energy and in mass coefficients (after [70]).

Table 4. 4. Theoretical deposited dose of air and pure a-Se (thickness 1756nm) at photon energy (keV). Values of $\mu/\rho$, $\mu_{en}/\rho$ and $\Phi(E)$ are from the spectrum of figure 4.5 and 4.6. Calculation of $D_{absorbed}$ and $D_{absorbed}$ of air and Se ($D_{absorbed}$ of air from equation (4.4a), and $D_{absorbed}$ of Se from equation (4.5a) in unit of Gray).

| $E$ keV | $\mu/\rho$ (Air) ($cm^2/g$) | $\mu_{en}/\rho$ (Air) ($cm^2/g$) | $\mu/\rho$ (Se) ($cm^2/g$) | $\mu_{en}/\rho$ (Se) ($cm^2/g$) | $\Phi(E)$ 30kVp (unitless) | $E_{absorbed}$ at E (air) (keV) | $D_{absorbed}$ at E (air) (Gy) | $E_{absorbed}$ at E (Se) (keV) | $D_{absorbed}$ at E (Se) (Gy) |
|---|---|---|---|---|---|---|---|---|---|
| 8 | 9.92 | 9.45 | 81.16 | 78.65 | 0 | 0 | 0 | 0 | 0 |
| 9 | 7.00 | 6.57 | 58.85 | 56.63 | 0 | 0 | 0 | 0 | 0 |
| 10 | 5.12 | 4.74 | 44.14 | 42.21 | 1.1E+02 | 1.3E-06 | 1.4E-16 | 5.9E-06 | 1.3E-15 |
| 11 | 3.90 | 3.52 | 34.02 | 32.27 | 1.8E+03 | 1.7E-05 | 1.9E-15 | 7.9E-05 | 1.7E-14 |
| 12 | 3.05 | 2.68 | 26.82 | 25.26 | 1.1E+04 | 8.8E-05 | 9.8E-15 | 4.3E-04 | 9.1E-14 |
| 13 | 2.43 | 2.09 | 148.51 | 81.83 | 3.5E+04 | 2.4E-04 | 2.6E-14 | 4.5E-03 | 9.7E-13 |
| 14 | 1.96 | 1.66 | 123.06 | 71.29 | 7.9E+04 | 4.5E-04 | 4.9E-14 | 9.5E-03 | 2.0E-12 |
| 15 | 1.61 | 1.33 | 103.30 | 62.70 | 1.5E+05 | 7.3E-04 | 8.0E-14 | 1.7E-02 | 3.6E-12 |
| 16 | 1.37 | 1.09 | 87.05 | 54.48 | 2.3E+05 | 9.6E-04 | 1.1E-13 | 2.4E-02 | 5.2E-12 |
| 17 | 1.17 | 0.90 | 74.13 | 47.75 | 3.2E+05 | 1.2E-03 | 1.3E-13 | 3.2E-02 | 6.9E-12 |
| 18 | 1.02 | 0.75 | 63.71 | 42.16 | 4.0E+05 | 1.3E-03 | 1.5E-13 | 3.8E-02 | 8.1E-12 |
| 19 | 0.89 | 0.63 | 55.20 | 37.48 | 5.1E+05 | 1.5E-03 | 1.7E-13 | 4.5E-02 | 9.6E-12 |
| 20 | 0.78 | 0.54 | 48.18 | 33.52 | 5.6E+05 | 1.5E-03 | 1.7E-13 | 4.7E-02 | 1.0E-11 |
| 21 | 0.71 | 0.46 | 42.18 | 29.74 | 6.3E+05 | 1.5E-03 | 1.7E-13 | 4.9E-02 | 1.1E-11 |
| 22 | 0.65 | 0.40 | 37.16 | 26.53 | 6.2E+05 | 1.3E-03 | 1.5E-13 | 4.5E-02 | 9.7E-12 |
| 23 | 0.59 | 0.35 | 32.92 | 23.79 | 6.0E+05 | 1.2E-03 | 1.3E-13 | 4.2E-02 | 8.9E-12 |
| 24 | 0.55 | 0.31 | 29.32 | 21.43 | 5.3E+05 | 9.6E-04 | 1.1E-13 | 3.5E-02 | 7.4E-12 |
| 25 | 0.50 | 0.27 | 26.23 | 19.39 | 4.4E+05 | 7.3E-04 | 8.1E-14 | 2.7E-02 | 5.8E-12 |
| 26 | 0.47 | 0.24 | 23.57 | 17.61 | 3.2E+05 | 4.9E-04 | 5.4E-14 | 1.8E-02 | 3.9E-12 |
| 27 | 0.43 | 0.21 | 21.27 | 16.06 | 1.8E+05 | 2.5E-04 | 2.8E-14 | 9.9E-03 | 2.1E-12 |
| 28 | 0.40 | 0.19 | 19.26 | 14.69 | 1.4E+05 | 1.8E-04 | 2.0E-14 | 7.1E-03 | 1.5E-12 |
| 29 | 0.38 | 0.17 | 17.50 | 13.48 | 8.5E+04 | 1.0E-04 | 1.1E-14 | 4.2E-03 | 8.9E-13 |
| 30 | 0.35 | 0.15 | 15.96 | 12.40 | 5.8E+04 | 6.5E-05 | 7.2E-15 | 2.7E-03 | 5.8E-13 |
| sum | | | | | 5896004 | 1.5E-02 | 1.64E-12 | 4.6E-01 | 9.78E-11 |

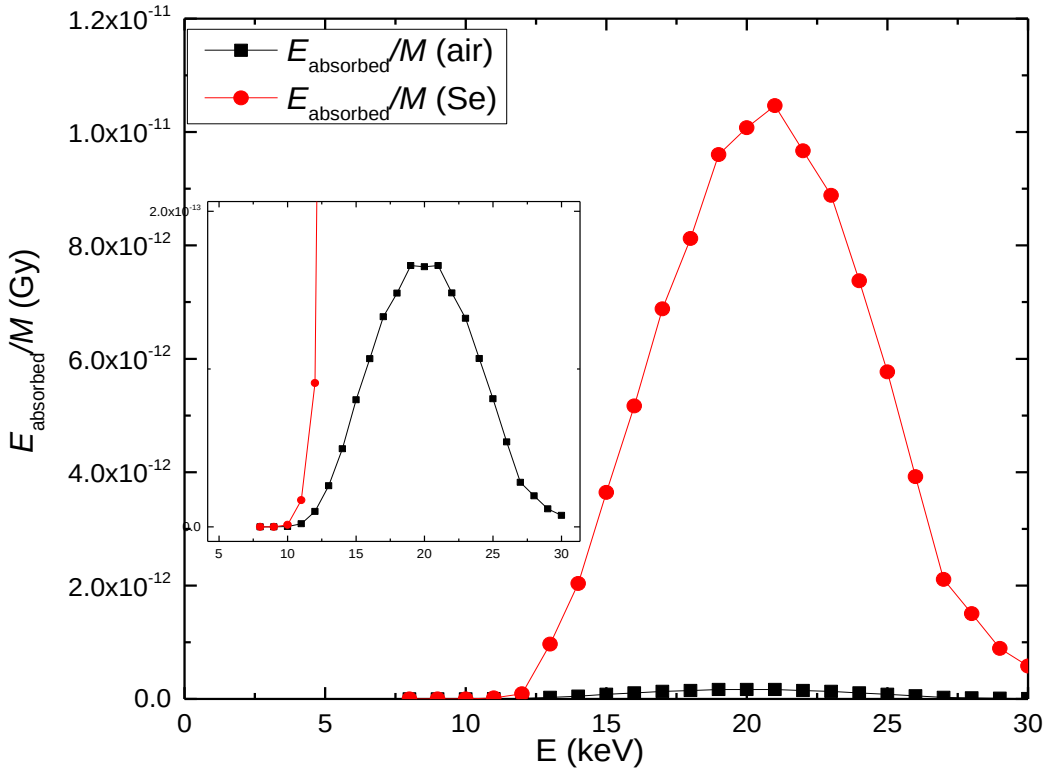


Figure 4. 7. Energy spectrum of theoretical dose of air (black) and pure a-Se (red) at 30 kVp from Table 4.4 (The inset of the figure is expanded to show the dose of air).

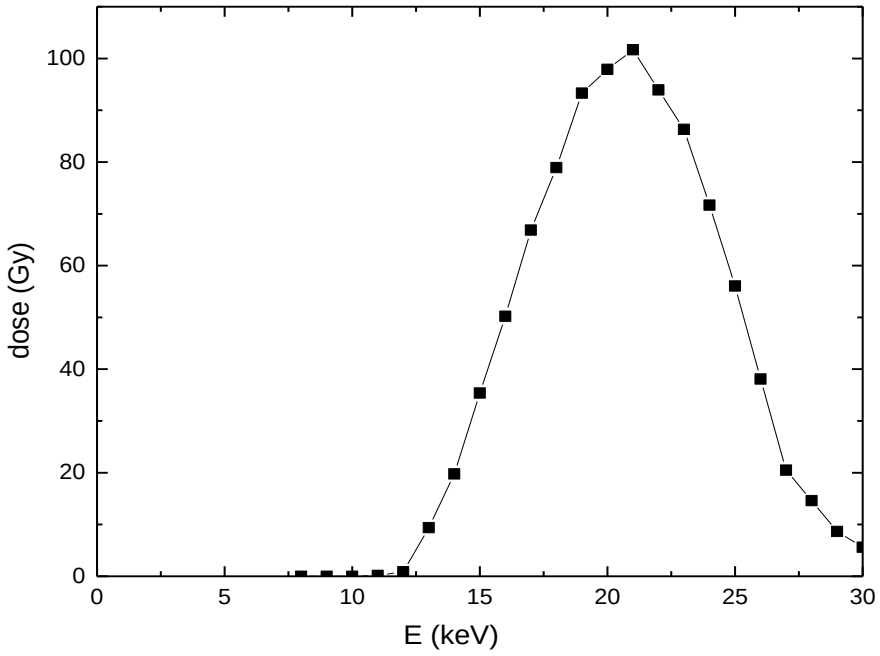


Figure 4. 8. Energy spectrum of absorbed dose in 20 minutes for pure a-Se with its thickness 1756 nm, using incident dose 15.93 Gy at 30 kVp.

## 4.7 UV-VIS spectrophotometer

A Perkin Elmer Lambda 900 UV/VIS/NIR spectrometer was used to measure the transmission spectra in the wavelength range 450 – 2500 nm. Figure 4.9 below is a schematic diagram of the spectrophotometer assembly.

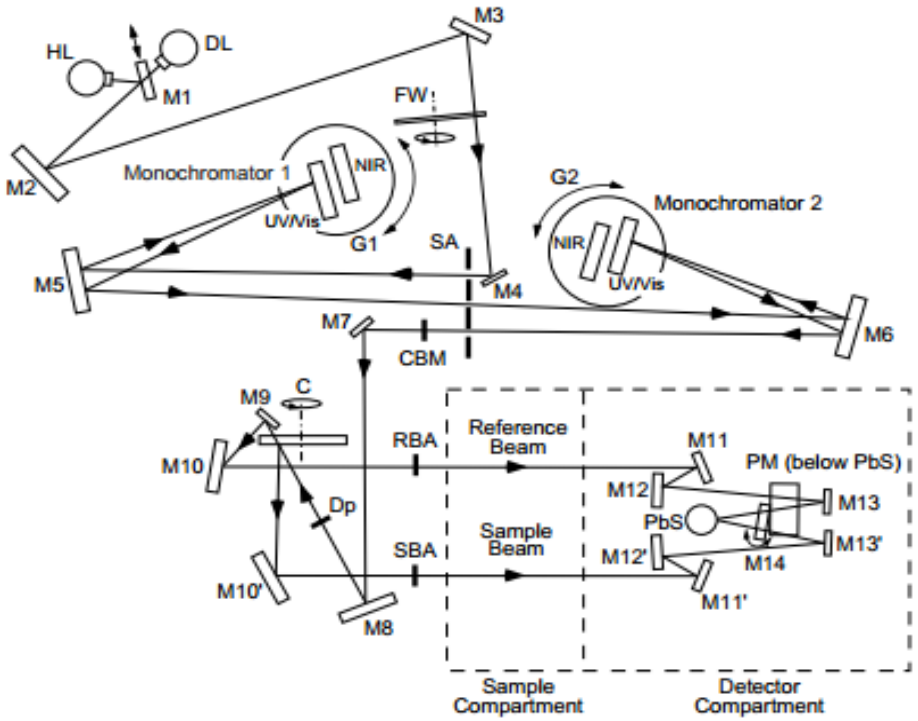


Figure 4. 9. A schematic diagram of the spectrophotometer assembly (after [71]).

A brief description of the light path in the UV-visible spectrometer instrument is following. First, the light is generated from a deuterium (DL) or halogen lamp (HL) as the radiation source. A deuterium lamp range spans into the ultraviolet region, whereas a halogen lamp's range spans the near IR and visible regions. Only the halogen lamp was used, since the experimental wavelength ranges from 450 to 2000 nm. Thus, the deuterium lamp range is not needed. The M1 mirror switches between the deuterium and halogen lamps and Mirrors M2 to M6 guide light towards monochromators 1 and 2. These have two diffraction gratings for the UV-visible range and the near infrared range [71].

The light beam with the selected wavelength is guided towards a chopper assembly (C) through the slit assembly (SA), a common beam mask (CBM) and mirrors (M6 – M8). When the chopper is not actuated, the beam is guided to the reference compartment through mirrors (M9 and M10)

to create the reference beam, which is detected by the photomultiplier (PMT) tube, which is used to measure the light intensity in the UV/VIS range. But when the chopper is rotating, the beam is guided to the sample compartment through mirrors M9 and M10 to create a transmitted light beam which is detected by the photomultiplier tube in the UV/VIS range. Then, the reference and transmitted beams are alternatively measured at each wavelength so that the transmission spectra are obtained in a wide range of wavelengths [71]. Figure 4.10 below shows a photograph of the spectrophotometer system used.

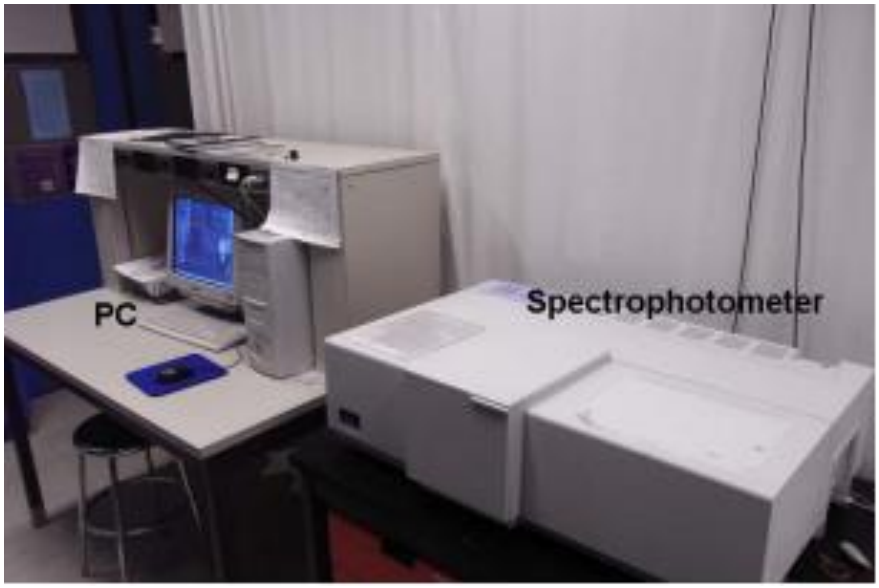


Figure 4. 10. The workstation for UV-Visible spectrophotometer (after [72]).

# Chapter 5. Results and Discussion

This chapter is divided into five sections. The first section deals with changes on the optical properties on heating. The second section examines whether thickness influences on optical properties. The third section examines influences on doping and/or alloying on films. The fourth sections investigate how a-Se films are influenced by X-ray exposure and whether these properties return to original states after exposures. The different composition a-Se samples used were: pure a-Se, a-Se 0.5% As, a-Se 6% As, a-Se 6% + ppm of Cs.

All films were fabricated by thermal evaporation technique as described in Section 4.2 and were exposed by X-rays for 20 minutes inside Faxitron. Then, transmission spectra were scanned from the UV visible spectrophotometer and the optical properties were extracted using Swanepoel technique as discussed in chapter 3. Between measurements, all films were kept in the dark and at room temperature to reduce light illumination or any external stimuli.

## 5.1 Optical properties of amorphous selenium influenced on heating

In this experiment, a-Se film was heated on an in-situ, custom-made sample holder inside the spectrophotometer, and this custom-made holder was connected to the temperature controller called Cryo controller unit T-2000. The film temperature was regulated by manually pressing power percent and temperature in degree Celsius on the Cryo controller. The sample temperature was increased from 24 °C to 55 °C, 59 °C, 72 °C, and 74 °C for pure a-Se, a-Se:0.3% As, a-Se:6% As and a-Se:6% As doped with 220 ppm Cs, each respectively. These temperatures are above the glass transition temperature $T_g$ which is 49°C, 85°C, and 75°C for pure a-Se, a-Se:6% As and a-Se:6% As doped with 220 ppm Cs of a-Se respectively, as observed on DSC measurements at a heating rate of 5 °C/min [58]. Table 5.1 summarizes all the essential optical properties ($n$, $d$, $Eg_U$, $Eg_T$, $\Delta E$) before and after heating above $T_g$ and Table 5.2 features the Wemple Di-Dominicio optical constants ($n_{WD}$, $E_o$ and $E_d$).

The transmittance values were decreased, and the entire transmission spectra were shifted to a

longer wavelength, that is "red shift" as shown in Figure 5.1. These red shifts of transmission affected all optical properties such as a decrease in refractive index $n$, an expansion in thickness, a decrease in two optical gaps $Eg_U$ and $Eg_T$, and an increase in Urbach slope $\Delta E$.

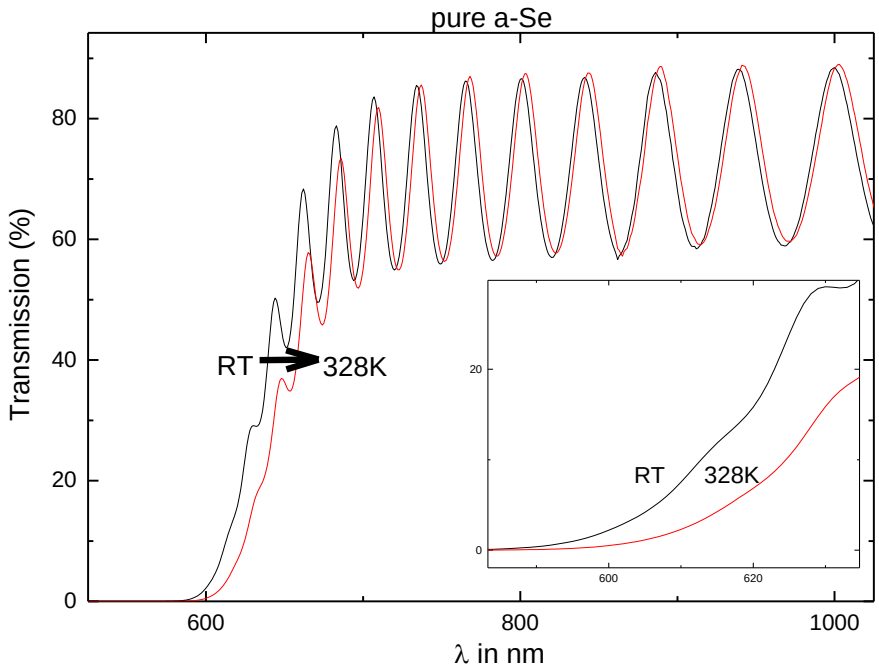


Figure 5. 1. The transmission spectra of pure a-Se film at room temperature and at 328 K (55 °C).

Table 5. 1 The influence of the heating at $T$g on optical properties for different composition a-Se films: pure a-Se, a-Se: 0.3% As, a-Se: 6% As and a-Se: 6% As: 220ppm Cs (RT refers a sample well-aged and relaxed at room temperature). (Note that $T_g$ is 49°C for pure a-Se, 85°C for a-Se:6% As, and 75°C for a-Se:6% As + 220ppm Cs).

| Sample | $\Delta d$ nm | $d$ nm | $n$ λ= 2000nm ±0.0011 | $Eg_T$ (eV) ±0.0007eV | $Eg_U$ (eV) ±0.0008eV | $\Delta E$ (meV) ±0.5meV | RMSE (%) |
|---|---|---|---|---|---|---|---|
| Pure a-Se RT | 14 | 2733.6 ± 1.2 | 2.4836 | 2.0072 | 2.0475 | 67.83 | 0.52 |
| Pure a-Se 55 °C | 11 | 2769.9 ± 1.2 | 2.4599 | 1.9708 | 2.0138 | 72.79 | 0.61 |
| % change | | 1.33% | -0.96% | -1.81% | -1.64% | 7.3% | |
| 0.3% As RT | 19 | 2672.1 ± 1.2 | 2.4820 | 2.0087 | 2.0463 | 67.34 | 0.46 |
| 0.3% As 59 °C | 19 | 2712.5 ± 1.2 | 2.4527 | 1.9711 | 2.0129 | 74.81 | 0.37 |
| % change | | 1.51% | -1.18% | -1.87% | -1.63% | 11.1% | |
| 6% As RT | 7 | 2057.1 ± 0.9 | 2.5041 | 2.0203 | 2.0450 | 69.33 | 0.46 |
| 6% As 72 °C | 2 | 2102.1 ± 0.9 | 2.4626 | 1.9665 | 1.9926 | 78.48 | 0.24 |
| % change | | 2.18% | -1.66% | -2.67% | -2.56% | 13.2% | |
| 6% As 220ppm RT | 9 | 3631.9 ± 1.6 | 2.4764 | 1.9805 | 2.0364 | 67.39 | 0.73 |
| 6% As 220ppm 74°C | 0 | 3710.2 ± 1.7 | 2.4354 | 1.9317 | 1.9915 | 73.44 | 0.58 |
| % change | | 2.16% | -1.65% | -2.46% | -2.21% | 8.97% | |

The $T_g$ is analogous to melting temperature of amorphous solids in a sense that a-Se transforms from glassy solid form to glassy liquid state at $T_g$. When transforming at $T$g, structural rearrangements occur and the thermal expansion coefficient $\alpha_L$ exhibits an increase as the sample is heated through its $T_g$ [73, 74]. The structural relaxation at in the Tg-region results in a structure with more voids and hence larger specific volume [75]. Therefore, there is an increase in the film thickness. As heating near Tg, the thickness increase is maximum 78 nm (2.2%) with heating at 74 °C and minimum 36 nm (1.3%) at 55 °C in Table 5.1.

The thickness increase is also related to a decrease in refractive index $n$, which are expected from the Clausius-Mossotti equation. When assuming polarizability is negligible and $N$ is inversely proportional to the thickness of the film in Clausis-Mossotti equation (2.20), it can describe the change in refractive index $\Delta n$ and the change in density $\Delta\rho$ (or change in thickness) according to Gonzalez, et al [57], which is given in equation (2.22b) below.

$$\frac{n^2-1}{n^2+2} = \sum_j \frac{N_j \alpha_j}{3\varepsilon_o} = \frac{1}{3\varepsilon_0}\sum_j \alpha_j \frac{\rho_j N_A}{M_{at,j}} \tag{2.20}$$

$$\frac{\Delta n}{n_o} = \frac{-(n_o^2 - 1)(n_o^2 + 2)}{(6n_o^2)}\frac{\Delta d}{d_0} \tag{2.22b}$$

If we apply equation (2.22b) to a-Se: 0.3% As sample, the experimental change in thickness ($\Delta d/d_o$) of 1.51 % (±0.091%) results in a drop of refractive index $(\Delta n/n_o)_{calc}$ of -1.72 % (±0.1%), which is close to the experimental change ($\Delta n/n_o$) of -1.2 %. This means that polarizability is almost constant (no change) on heating, and an increase in refractive index is caused by the density, which is atomic concentration.

This phenomenon applies to other samples too. The relative changes in $\Delta n/n_o$ and $\Delta d/d_o$ are plotted by different compositions of a-Se films in Figure 5.3 and it shows there is a matching relationship between $\Delta n/n_o$ and $\Delta d/d_o$. Figure 5.2 shows the downshift of refractive index with an increase in temperature due to the decrease in the density (increase in $\Delta d/d$).

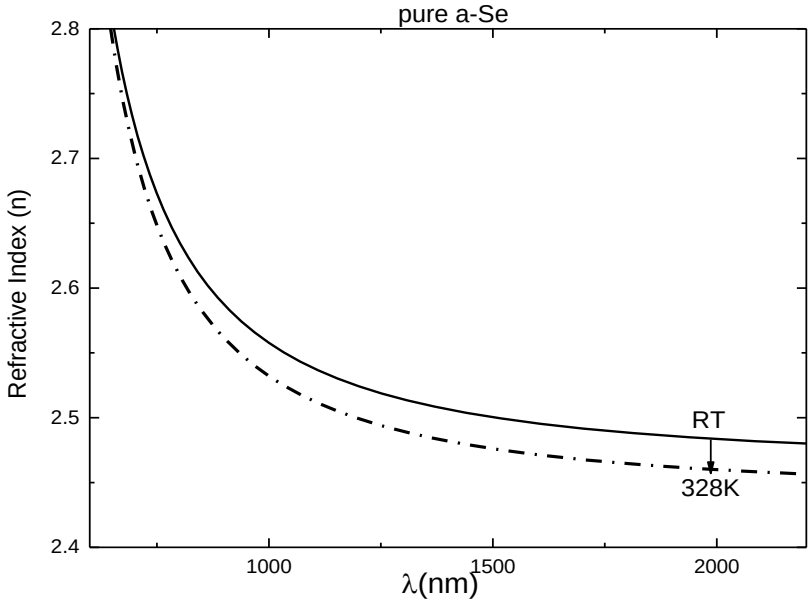


Figure 5. 2. Sellmeier refractive index dispersion for an a-Se film after heating. The solid line represents the dispersion at room temperature and dotted line is the dispersion after heating at 328K.

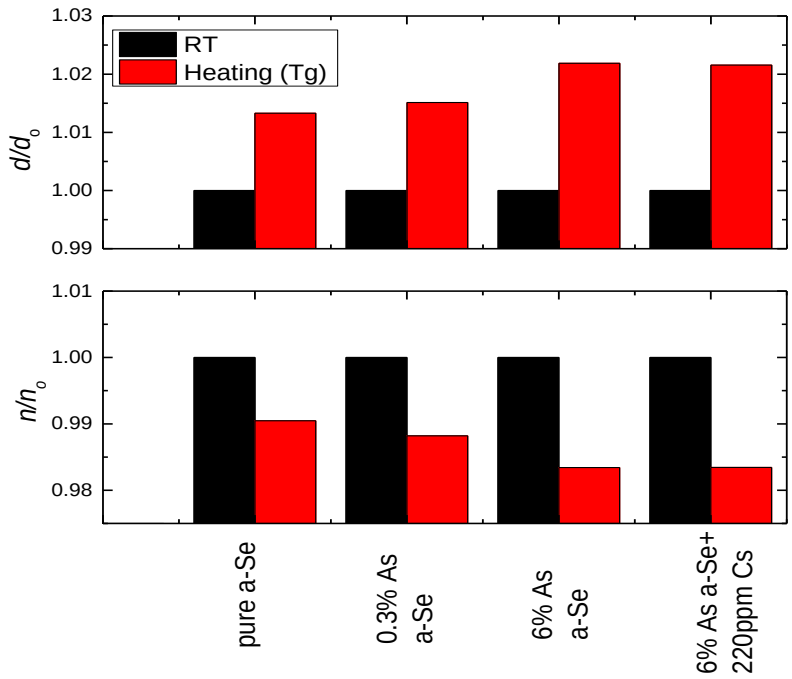


Figure 5. 3. The normalized changes in thickness ($d/d_o$) (black curve) and refractive index ($\Delta n/n_o$) (red curve) as a function of compositions in a-Se: pure a-Se, a-Se 0.3% As, a-Se 6% As, a-Se 6% As + 220ppm Cs after heating to glass transition temperature Tg. The shaded area corresponds to statistical errors in $\Delta d/d$ and $\Delta n/n$ determination and is based on assigning $2\sigma$ to the full width of error region.

The refractive index which was fitted in the Sellmeier in Figure 5.2 was re-fitted into the Wemple-DiDominico relationship as follows: $n_{WD}{}^2 = 1 + \frac{E_o E_d}{E_o{}^2 - (hv)^2}$ to extract the characteristic parameters $E_o$ and $E_d$. Typical results are summarized in Table 5.2 below.

Table 5. 2 The optical parameters of curve fitting *n* to the *Wemple-DiDominicio* relationship ($n_{WD}$ is the *Wemple-DiDominicio* refractive index at 2000nm).

| | | $n_{WD}{}^2 = 1 + \frac{E_o E_d}{E_o{}^2 - (hv)^2}$ | | | |
|---|---|---|---|---|---|
| Sample | Temperature | $n_{WD}$ (at 2000nm) | $E_o$ (eV) ±0.0096eV | $E_d$ (eV) ±0.066eV | RMSE of fit (%) |
| Pure a-Se | Room temperature | 2.4733 | 3.7773 | 18.809 | 2.6 |
| | 55C° (328K) | 2.4490 | 3.7468 | 18.203 | 2.4 |
| | % change | -0.99% | -0.81% | -3.22% | |
| 0.3% a-Se | Room temperature | 2.4717 | 3.7793 | 18.790 | 2.92 |
| | 59C° (332K) | 2.4421 | 3.7253 | 17.980 | 2.72 |
| | %change | -1.19% | -1.43% | -4.31% | |
| 6% As 2-3um | Room temperature | 2.4922 | 3.7630 | 19.077 | 2.75 |
| | 72C° (345K) | 2.4515 | 3.6984 | 18.008 | 2.60 |
| | %change | -1.63% | -1.72% | -5.60% | |
| 6% As Cs 220ppm | Room temperature | 2.4669 | 3.7702 | 18.655 | 2.6 |
| | 74C° (347K) | 2.4260 | 3.7045 | 17.591 | 2.4 |
| | %change | -1.66% | -1.74% | -5.7% | |

In Table 5.2, the heating results in a decrease in oscillator energy $E_o$ with a decrease in dispersion energy $E_d$. The decrease in $E_d$ is related to other physical parameters through the following empirical relationship of $E_d$: $E_d = \beta N_c Z_a N_e$ in equation (2.18), where $Z_a$ is the formal chemical valency of anion, $N_e$ is the effective number of valence electrons per anion, $\beta$ is constant either ionic or covalent, and $N_c$ refers to the effective coordination number of cation nearest-neighbor to the anion.

We had discussed in Chapter 2 that in a-Se, there are intrinsic pairs of charge defects, which are $Se_1^-$ and $Se_3^+$. In a-Se, the $N_c$ is related to coordination number of positively charged defect, $Se_3^+$ of the VAP. The decrease in $E_d$ is related to drop in $N_c$ of $Se_3^+$. In heated samples in $T_g$ region, we had discussed that the rearrangement in structure occurs by the addition of heat to the structure. This leads to an increase in the intermolecular distance between atoms, decreasing an effective coordination number $N_c$ of $Se^{3+}$, resulting in a decrease in $E_d$. Table 5.2 shows the

change in $E_d$ from –3.2 % for pure a-Se sample (heating at 55 °C) up to maximum –5.7% for the a-Se:6% As with Cs (heating at 74 °C), and the change in $E_o$ is minimum –0.81% and maximum –1.74%. This implies that as heating the samples more, interatomic distances increases more, with decreasing $N_c$ more.

The drop in $E_o$ is related to the decrease in $Eg_T$. The $E_o$, which is considered as an average energy gap, varies in proportion to Tauc gap [51]. When comparing values of $E_o$ from Table 5.2 and $Eg_T$ from Table 5.3, it comes to $E_o \approx 1.89\times Eg_T$. This relation is close to that observed by Tan [43] $E_o \approx 1.9\times Eg_T$, and other authors (Gonzalez-Leal *et al* [57] and E.R. Shaaban [76]) who reported that $E_o \approx 2.0\times Eg_T$.

Table 5. 3 Fitting parameters of two optical band gaps of films at RT and $T_g$. The Tauc band gap: $\alpha h\upsilon = A(h\upsilon - Eg_T)$ and Urbach gap: $\alpha = C\times\exp(h\upsilon/\Delta E)$, where $A$ = Tauc constant, $Eg_T$ = Tauc band-gap, $\alpha$ refers to the absorption coefficient ($cm^{-1}$), $Eg_U$ = Urbach band-gap and $\Delta E$ refers to Urbach energy. RT refers to a film kept at room temperature (aged) just before heating.

| Sample | Temperature | $d$ (nm) | $A$ ($cm^{-1}$) | $Eg_T$ (eV) ±0.0007eV | $C$ x$10^{-9}$ ($cm^{-1}$) | $Eg_U$ (eV) ±0.0008eV | $\Delta E$ (meV) ±0.5meV | $\alpha$ ($cm^{-1}$) at 2.05eV |
|---|---|---|---|---|---|---|---|---|
| Pure a-Se | RT | 2733.6 ± 1.2 | 423074 | 2.0072 | 0.778 | 2.0474 | 67.83 | 10065 |
| | 55 °C | 2769.9 ± 1.2 | 390671 | 1.9708 | 9.641 | 2.0138 | 72.79 | 14633 |
| | %change | 1.33% | -7.66% | -1.81% | 91.9% | -1.64% | 7.3% | 45% |
| 0.3% a-Se | RT | 2672.1 ± 1.2 | 429225 | 2.0087 | 0.637 | 2.04626 | 67.34 | 10031 |
| | 59 °C | 2712.5 ± 1.2 | 393045 | 1.97 | 20.63 | 2.01292 | 74.81 | 15046 |
| | %change | 1.51% | -8.43% | -1.93% | 96.9% | -1.63% | 11.1% | 50% |
| 6% As 2-3um | RT | 2057.1 ± 0.9 | 495839 | 2.02 | 1.55 | 2.04503 | 69.33 | 10256 |
| | 72 °C | 2102.1 ± 0.9 | 434957 | 1.9664 | 93.99 | 1.99259 | 78.48 | 17798 |
| | %change | 2.18% | -12.28% | -2.67% | 98.4% | -2.56% | 13.2% | 74% |
| 6% As Cs:220 ppm | RT | 3631.9 ± 1.6 | 330493 | 1.9805 | 0.753 | 2.03644 | 67.39 | 11235 |
| | 74 °C | 3710.2 ± 1.7 | 297972 | 1.9317 | 16.72 | 1.99145 | 73.44 | 17187 |
| | %change | 2.16% | -9.84% | -2.46% | 95.5% | -2.21% | 9.0% | 53% |

The decrease in $Eg_T$ and $Eg_U$ upon heating in Table 5.3 is related to transmittance decreases, we saw in Figure 5.1. The transmission intensity is lost by absorbing and less radiation is penetrated through the sample, which means that absorption coefficient is shifted up and results in a band gap decrease at a given wavelength. The increases in Urbach width and decreases in band-gap are agreement with the experimental results from Tichy [55]. Figure 5.4 and 5.5 show a determination on $Eg_U$ and $Eg_T$ from fitting lines.

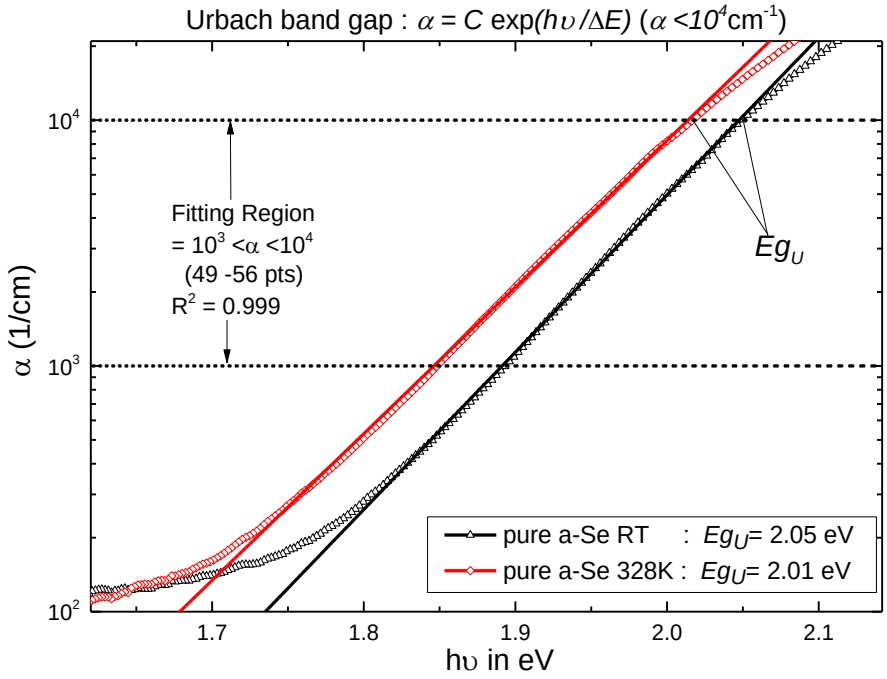


Figure 5. 4. Absorption coefficient of a pure a-Se film at room temperature (RT) and after heating at 328K for the determination of Urbach band-gap $Eg_U$ in the low absorption region ($\alpha < 10^4$ $cm^{-1}$).

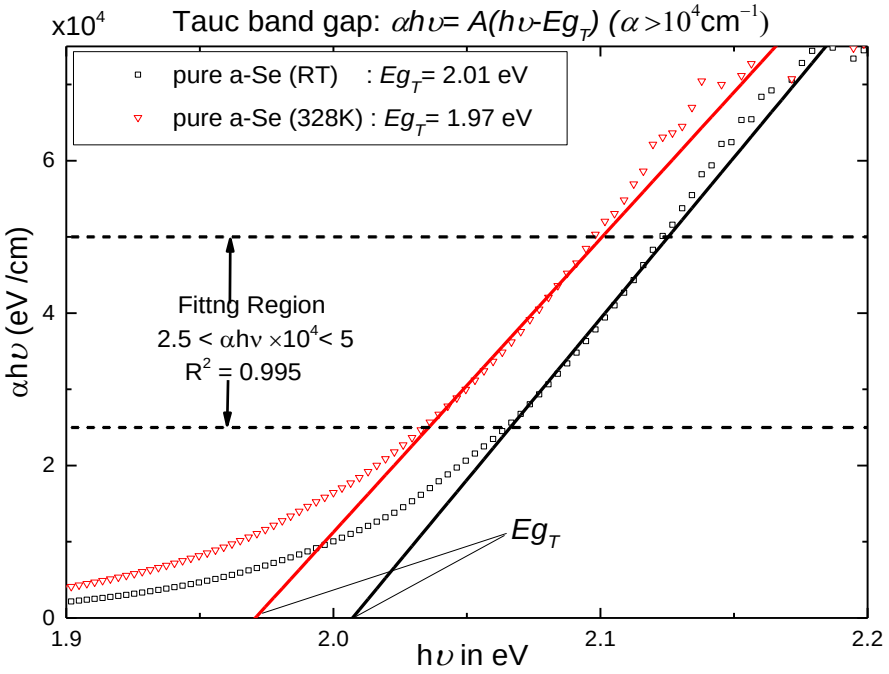


Figure 5. 5. Absorption coefficient of a pure a-Se at room temperature and after heating at 328K for the determination of Tauc band-gap $Eg_T$ in the high absorption region ($\alpha > 10^4$ $cm^{-1}$).

## 5.2 Influence of thickness on amorphous selenium

The purpose of this section serves as a control experiment to check whether the material properties extracted depend on the sample thickness. Table 5.4 lists the optical properties of two different thicknesses for the a-Se:0.5%As (the first two rows) and a-Se:6%As (the last two rows) films. The films were aged sufficiently long for their properties to stabilize. It should be remembered however that these films were prepared at different times and there may be some small differences in the compositions of the two films due to fractionation effects during deposition. The quoted values are nominal (values in the bulk material in the evaporation boat).

Table 5. 4. The influence of thickness on optical properties for the a-Se:0.5%As film (thickness difference between the two ~0.4 μm) and a-Se:6% As film (thickness difference ~0.3 μm).

| *d* (nm) | Sample (unirradiated) | Δ*d* (nm) | *n* at 2000nm ±0.0012 | $Eg_T$ (eV) ±0.0007eV | $Eg_U$ (eV) ±0.0008eV | Δ*E* (meV) ±0.5meV | Aged (hrs) |
|---|---|---|---|---|---|---|---|
| 1495.5 | a-Se:0.5% As | 12.2 | 2.4753 | 2.0505 | 2.0454 | 65.76 | 1152 |
| 1859 | | 0.01 | 2.4668 | 2.0321 | 2.0401 | 67.79 | 1656 |
| diff ~ 0.4μm | % change | | -0.34% | -0.90% | -0.26% | 3.09% | |
| 3261.2 | a-Se:6% As | 21.5 | 2.4734 | 2.0040 | 2.0437 | 65.64 | 1336 |
| 3552.1 | | 5.4 | 2.4705 | 1.9966 | 2.0426 | 65.59 | 2104 |
| diff ~ 0.3μm | % change | | -0.12% | -0.37% | -0.05% | -0.08% | |

In Table 5.4 above shows that there are small differences in the refractive index for different thickness films, but the differences are within experimental errors. There are small differences in $Eg_T$ values. However, this difference could be due to fitting into the high absorption region for the thick film, which could give errors (artifacts) for Tauc band-gap $Eg_T$ as shown in the high absorption region in the Figure 5.6 below. There is an upper absorption limit for the spectrophotometer as well. Figure 5.7 is the determination of $Eg_U$ for two different thicknesses. The change in $Eg_U$ and $\Delta E$, therefore, are within experimental errors. In conclusion, there are no significant changes in the extracted optical properties that depend on thickness.

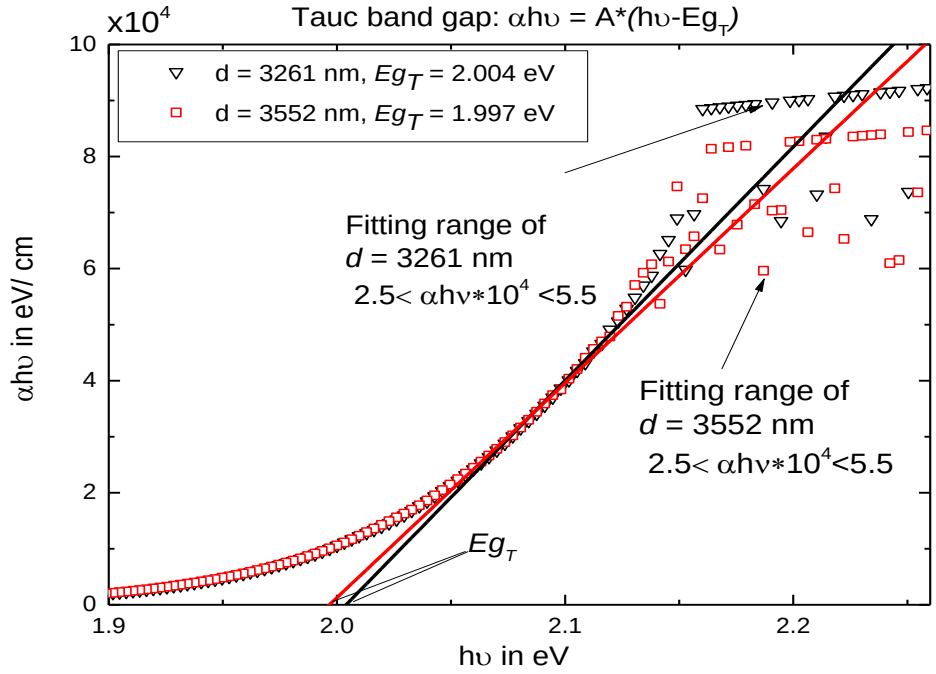


Figure 5. 6. The determination of $Eg_T$ in $\alpha > 10^4$ cm$^{-1}$ for two different thickness films of a-Se:6%As.

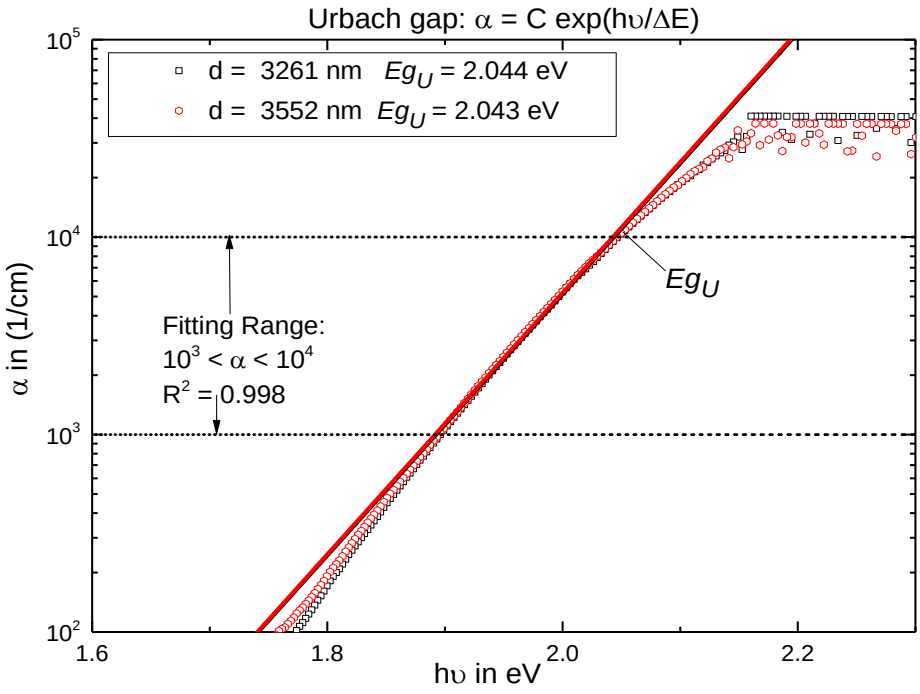


Figure 5. 7. The determination of $Eg_U$ in $\alpha < 10^4$ cm$^{-1}$ for two different thickness films of a-Se:6%As.

## 5.3 Influence of alloying As and doping Cs on optical constants of a-Se

This section describes optical properties affected by alloying with As and doping with Cs. The transmission spectra of samples with different composition a-Se samples were scanned three months period. In Table 5.6, the first three rows are properties due to alloying a-Se with As with concentrations, and the next two rows are properties due to Cs-doping. In Table 5.6, alloying with 6% As has increased *n* from 2.463 that of pure a-Se to 2.474 that of a-Se:6%As, a 0.435%, and decreased $Eg_T$ from 2.039 that of pure a-Se to 2.020eV of a-Se:6%As by 0.02 eV, a –0.94%. The Cs-doping on 140ppm has increased *n* further by 0.48% and decreases $Eg_T$ by 0.004 eV.

Table 5. 5. Optical properties of a-Se when alloying As and doping Cs on a-Se with different concentrations.

| Sample | Δ*d* nm | *d* nm | *n* at 2000nm (±0.0012) | $Eg_T$ eV ±0.0007eV | $Eg_U$ eV ±0.0007eV | Δ*E* meV ±0.5meV | *α* at 2.05 eV | Aged hours |
|---|---|---|---|---|---|---|---|---|
| a-Se | 0 | 1822.4 ±1.8 | 2.46316 | 2.0386 | 2.0451 | 65.39 | 10266 | 1917 |
| 0.5%As | 0 | 1858.7 ±1.8 | 2.46678 | 2.0321 | 2.0401 | 67.79 | 10721 | 1649 |
| 6% As | 18 | 2831.6 ±2.5 | 2.47387 | 2.0194 | 2.0424 | 66.43 | 10562 | 183 |
| %change | | | 0.435% | -0.94% | -0.132% | 1.59% | 2.9% | |
| 6% As | 18 | 2831.6 ±2.5 | 2.47387 | 2.0194 | 2.0425 | 66.43 | 10562 | 183 |
| 6%As +Cs 140ppm | 21 | 2488.8 ±2.2 | 2.48565 | 2.0169 | 2.0367 | 69.45 | 11260 | 570 |
| %change | | | 0.48% | -0.123% | -0.284% | 4.54% | 6.6% | |

The relation between an increase in *n* and a decrease in two optical gaps, $Eg_T$ and $Eg_U$, agrees with *Moss's rule* ($n^4E_g$ = constant) [59]. Also, this is similar to Jon Petursson et al [77] in that the $E_{gT}$ decreases with As alloying for the a-Se $_{1-x}$As$_x$ alloys.

We apply the Lorentz-Lorentz equation (2.20) below to examine the nature of refractive index increase (Δ*n*). Since atomic concentration *N* is not inversely proportional to thickness due to alloying As in a-Se, we need to consider equation (2.20) to examine the causes of changes in Δ*n*, whether it is change from polarizability *α* or atomic concentration *N*.

$$\frac{n^2-1}{n^2+2} = \sum_j \frac{N_j \alpha_j}{3\varepsilon_o} = \frac{1}{3\varepsilon_0}\sum_j \alpha_j \left(\frac{\rho_j N}{M_{at,j}}\right) \tag{2.20}$$

where $\varepsilon_o$ is the vacuum permittivity, and $N_j$ is the number of polarizable units of type j per

volume unit, given as $N_j = \frac{\rho_j N_A}{M_{at,j}}$, with its polarizability $\alpha_j$, its density $\rho_j$, its molar mass $M_{\text{at, j}}$ and Avogadro's number $N_A$.

The alloying in the Se-As system changes its mass density and atomic molar mass (atomic concentration) [78]. The polarizability in the Se-As system is not influenced since both Se and As have an approximately similar radii and the polarizability is proportional to the size of atom [76]. However, since Cs has much higher radius than Se, Cs doping in Se-As-Cs system would influence polarizability. For instance, using linear interpolation from Borisova table [78], alloying 6% As in pure a-Se in the first three rows in Table 5.5 has increased density $\rho$ from 4.29 g/cm$^2$ pure a-Se to 4.302 g/cm$^2$ a-Se:6% As, and decreases atomic molar mass $M_{\text{at}}$ from 78.96 g/mol to 78.718 g/mol, which results in an increase on $N$ from $N_{\text{Se}} = 3.27 \times 10^{22}$ atoms cm$^{-3}$ to $N_{\text{Se-As}} = 3.29 \times 10^{22}$ atoms cm$^{-3}$ , a 0.59 % increase.

The polarizability $\alpha$ is calculated to be $5.10\times10^{-40}$ F m$^2$, $5.09\times10^{-40}$ F m$^2$ and $5.11\times10^{-40}$ F m$^2$ for pure a-Se, a-Se:6% As and a-Se:6% As + Cs 140 ppm respectively. The polarizability $\alpha$ has increased 0.4% on Cs-doping and decreased -0.2% on As alloying. Therefore, the increase in refractive index $n$ with As alloying is due to an atomic concentration, and the increase in $n$ with Cs is not due to atomic concentration, but polarizability [58]. The a-Se charged defects (i.e. $Se_1^-$) might be associated with Cs ions, contributing to ionic polarizability [58]. Figure 5.8 below gives an illustration on the increases in $n$ with As alloying and further increase with Cs doping, and Figure 5.9 and 5.10 below show that As alloying and Cs doping shift the optical gaps to lower photon energy.

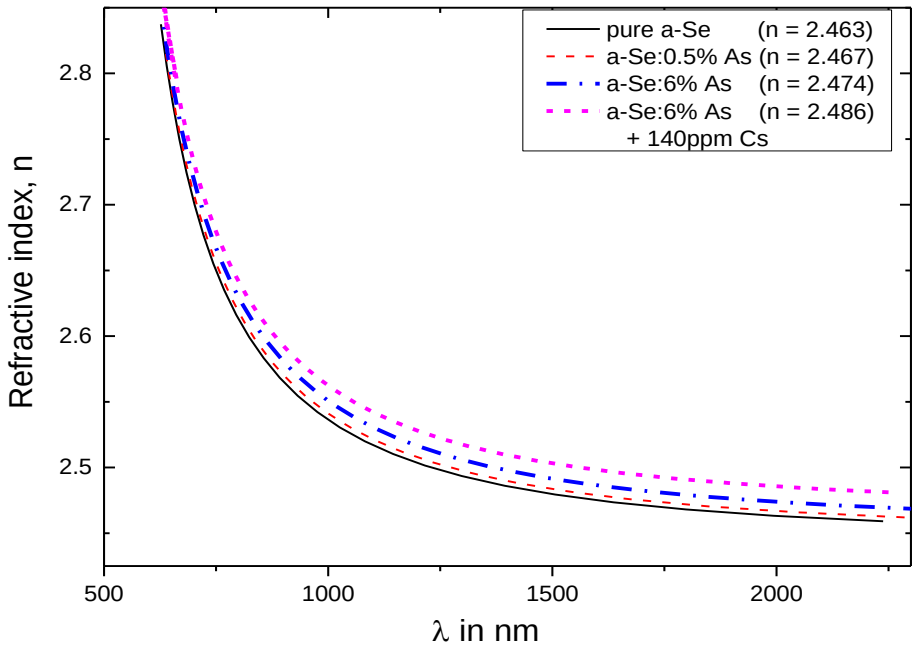


Figure 5. 8. The refractive index dispersion diagram for the various composition a-Se films.

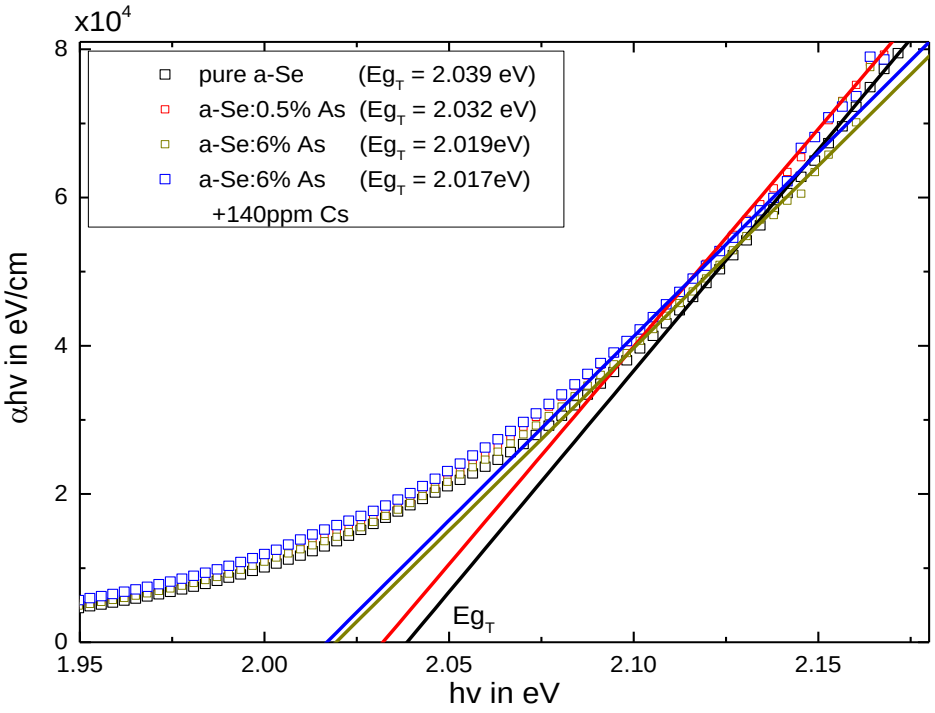


Figure 5. 9. The optical absorption coefficient (αhυ) vs photon energy (hυ) of the different composition a-Se films for the determination of $E_{gT}$ in $\alpha > 10^4$ cm$^{-1}$.

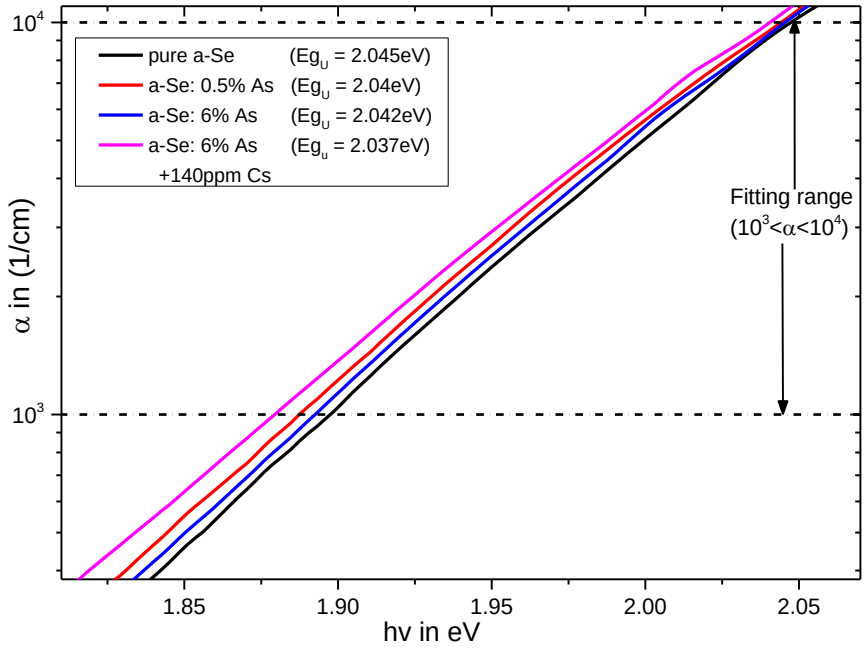


Figure 5. 10. The optical absorption coefficient (α) vs photon energy (hυ) of the different composition a-Se films for the determination of $E_{gU}$ in $\alpha < 10^4$ cm$^{-1}$.

## 5.4 X-ray induced effects

In this experiment, the transmission spectrum of films was scanned before and after irradiating X-rays for 20 minutes at the same spots. The reason for scanning the same spot of film twice is to observe a change in thickness associated to X-ray irradiation. Also, to avoid aging effects, the transmission spectrum was scanned right away once completing 20 minutes of exposure. The samples were kept in the dark at room temperature between measurements, to avoid other external stimuli.

We exposed different compositions of a-Se films (pure a-Se, a-Se:0.5% As, a-Se:6% As, and a-Se:6% As: ppm Cs) the same dose of X-rays to observe composition influence and we also irradiated each of the films under different dose of X-rays, a low dose at 30 kVp and a high dose at 70 kVp to observe dose influence. The total delivered doses were approximately 943 Gy and 3148 Gy at 30 and 70 kVp radiation respectively with the total incident doses being 15.9 Gy and 44.0 Gy in air respectively. The calculation of dose in Se and air followed the method described in Section 4.4, 4.5 and 4.6. The variation of density in As alloying or Cs doping was not taken in account to calculate dose. The deposited energy in either pure a-Se or 0.5% As-alloyed a-Se was assumed to be equivalent as long as the film thickness was the same, since alloy concentration is very small.

The key point is photo contraction which accompanies an increase in the refractive index. The photo-induced refractive index induced by a HeNe laser was also observed for a $As_2Se_3$ film [79] and for $As_2Se_3$ and $As_2S_3$ films by UV exposure [80]. Also, the photo-induced effects of a-Se turns out to be similar from aging effect in respect to optical changes. The aging effect gives a decrease in $d$ with an increase in $n$ resulting from the structural relaxation [81].

Tanaka [82] proposed that there is a metastable state in a-Se during irradiation with the excitation of lone-pair electrons from the VB to the CB. In this excited state, the dynamical interchain bonds form between chains, increasing an atomic coordination number. Since this bond is unstable, the bond breaking occurs, generating charged coordination defects (VAP) which have been proven by ESR measurements from Kolobov [83] and time-of-flight measurements from Walornyj [7]. It might be that there are some structural rearrangements

associated with defects generation, which is responsible for the thickness decrease.

Table 5.6 Optical properties of the four components of a-Se films (pure a-Se, a-Se:0.5% As, a-Se: 6% As, a-Se: 6% As 140ppm Cs) before and after X-ray irradiation at 30 and 70 kVp.

| Sample | Treatment | Dose (Gy) | Δ*d* (nm) | *d* (nm) | *n* (*λ*=2000nm) ±0.0012 | $Eg_T$ (eV) ±0.0007eV | $Eg_U$ (eV) ±0.0008eV | Δ*E* (meV) ±0.6meV |
|---|---|---|---|---|---|---|---|---|
| Pure a-Se | Unirradiated | | 0 | 1816.7 ± 0.8 | 2.4666 | 2.0391 | 2.0457 | 65.81 |
| | 30 kVp | 949 | 0 | 1815.2 ± 0.8 | 2.4684 | 2.0388 | 2.0461 | 65.73 |
| | % change | | | -0.082% | 0.071% | -0.014% | 0.019% | -0.114% |
| | Unirradiated | | 11 | 1755.7 ± 0.8 | 2.4924 | 2.0416 | 2.0444 | 68.11 |
| | 70 kVp | 3160 | 11 | 1754.0 ± 0.8 | 2.4953 | 2.0407 | 2.0451 | 68.20 |
| | % change | | | -0.101% | 0.115% | -0.043% | 0.034% | 0.135% |
| a-Se: 0.5% As | Unirradiated | | 0 | 1796.6 ± 0.8 | 2.4581 | 2.0370 | 2.0465 | 66.95 |
| | 30 kVp | 950 | 0 | 1794.5 ± 0.8 | 2.4613 | 2.0370 | 2.0467 | 66.89 |
| | % change | | | -0.120% | 0.129% | 0% | 0.013% | -0.097% |
| | Unirradiated | | 12 | 1495.5 ± 0.7 | 2.4753 | 2.051 | 2.0454 | 65.76 |
| | 70 kVp | 3164 | 13 | 1492.0 ± 0.7 | 2.4800 | 2.051 | 2.0458 | 66.25 |
| | % change | | | -0.234% | 0.188% | 0.045% | 0.016% | 0.74% |
| a-Se:6% As | Unirradiated | | 20 | 3397.6 ± 1.5 | 2.4624 | 2.0007 | 2.0397 | 66.48 |
| | 30 kVp | 934 | 20 | 3392.7 ± 1.5 | 2.4659 | 2.0014 | 2.0400 | 66.29 |
| | % change | | | -0.142% | 0.141% | 0.036% | 0.015% | -0.297% |
| | Unirradiated | | 5 | 3552.1 ± 1.6 | 2.4705 | 1.9966 | 2.0426 | 65.59 |
| | 70 kVp | 3133 | 7 | 3545.8 ± 1.6 | 2.4749 | 1.9967 | 2.0426 | 65.60 |
| | % change | | | -0.178% | 0.178% | -0.027% | 0.001% | 0.014% |
| a-Se:6% As +140 ppm Cs | Unirradiated | | 7 | 2993.6 ± 1.4 | 2.4541 | 1.9987 | 2.0387 | 67.20 |
| | 30 kVp | 938 | 8 | 2989.8 ± 1.4 | 2.4571 | 1.9984 | 2.0388 | 67.09 |
| | % change | | | -0.127% | 0.123% | -0.016% | 0.005% | -0.164% |
| | Unirradiated | | 14 | 3351.8 ± 1.5 | 2.4709 | 2.0042 | 2.0445 | 65.85 |
| | 70 kVp | 3136 | 15 | 3342.9 ± 1.5 | 2.4775 | 2.0034 | 2.0443 | 65.95 |
| | % change | | | -0.267% | 0.268% | -0.043% | -0.007% | 0.15% |

In Table 5.6, it was found that the refractive index *n* has increased and thickness *d* has decreased upon X-ray irradiation. At 30 kVp irradiation, increases in *n* go from 0.07% (+0.002) for pure a-Se up to 0.12% (+0.003) for a-Se 6% As + 140ppm Cs with decreases in *d* go from -0.08% (–1.5 nm) up to -0.13% (–3.8 nm). At 70 kVp irradiation, increases in *n* go from 0.12% (+0.003) for pure a-Se up to 0.27% (+0.007) for a-Se 6% As + 140ppm Cs, with decrease in *d* from -0.10% (–1.7 nm) up to -0.27% (–8.9 nm). It seems that 70 kVp has stronger X-ray effects than 30 kVp, and there are composition effects upon X-ray irradiation. Figure 5.11 shows that the refractive index was shifted up upon 70 kVp irradiation, and it was shifted further up with Cesium doping in a-Se.

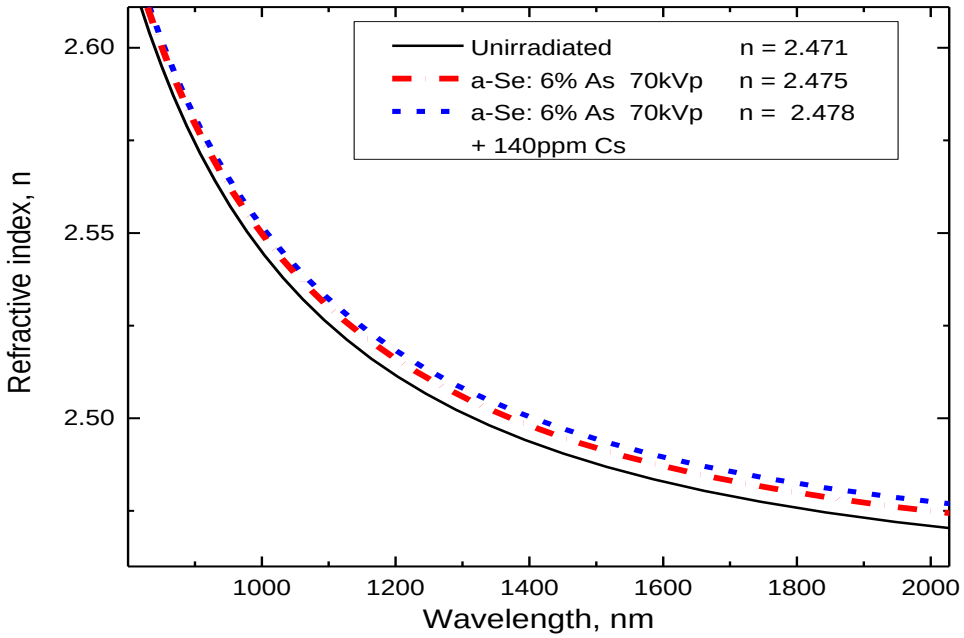


Figure 5. 11. Refractive index vs. wavelength for a-Se:6% As film (red curve) and a-Se:6% As +140ppm Cs doped films (blue curve) before (black curve) and after irradiation at 70 kVp.

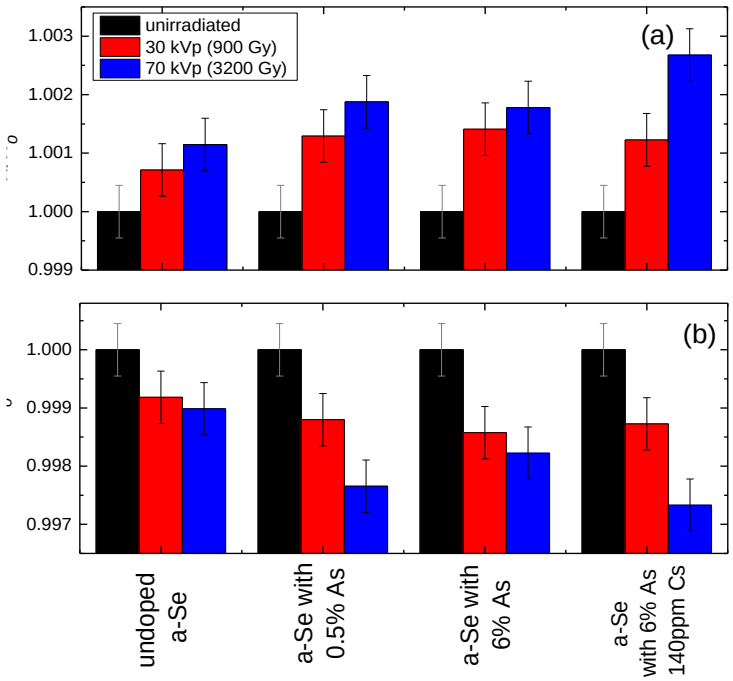


Figure 5. 12. The relative change of refractive index $\Delta n/n_o$, triangle symbols, and thickness $\Delta d/d_o$, square symbols as a function of compositions in a-Se: pure a-Se, a-Se 0.5% As, a-Se 6% As, a-Se 6% As + 140ppm Cs after irradiating at 30 kVp (red line) and 70 kVp (blue line). The shaded area corresponds to statistical errors in $\Delta d/d$ and $\Delta n/n$ determination and is based on assigning $2\sigma$ to the full width of error region.

The relative changes ($\Delta n/n_o$ and $\Delta d/d_o$) for the different composition of a-Se were plotted in a bar in Figure 5.12. It shows that X-ray effects for As alloying are weak, since the X-ray effects at 70 kVp go up with 0.5% As and down with 6% As, and the influence of Cs seems to be weak as well. The relative percent changes in $\Delta n/n_o$ and $\Delta d/d_o$ in Figure 5.12 were plotted as a function of the deposited dose in Figure 5.13. The 30 kVp in red bar and 70 kVp in blue bar correspond to 900 Gy and 3150 Gy in Figure 5.13. The X-ray effects increase gradually with increasing dose, which implies that X-ray effects depend on the dose.

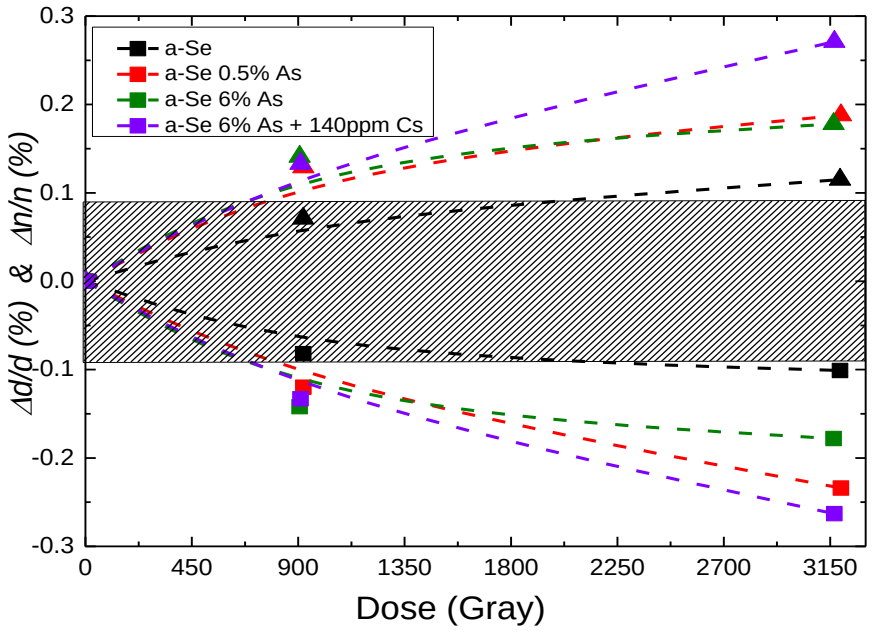


Figure 5. 13. The relative change of thickness ($\Delta d/d$), square symbols, and refractive index ($\Delta n/n$), triangle symbols, in a-Se samples with varying compositions (*dotted curves*) as a function of delivered (absorbed) dose in a-Se. a-Se, *black*; a-Se 0.5%, *red*; a-Se 6% As, *green*; a-Se 6% As +140 ppm Cs, *purple*; after irradiation with 30 kVp (900 Gy) and 70 kVp (3150 Gy). *Shaded area* corresponds to statistical errors in $\Delta d/d$ and $\Delta n/n$ determination and is based on assigning $2\sigma$ to the full width of error region.

The increase in refractive index upon irradiating with X-ray is due to a density increase, that is thickness decrease, possibly caused by structural re-arrangements. Using the Lorenz-Lorenz relation from equation (2.20) above, change of $\Delta n/n_o = +0.27\%$ predicts a change $(\Delta d/d_o)_{calc} = -0.24\%$, which is close to the experimental change $\Delta d/d_o = -0.27\%$ for a-Se 6% +140ppm Cs. This correlation does not dependent on doped or pure samples or deposited doses. Otherwise, Figure 5.12 and 5.13 would not show a symmetry between $\Delta n/n_o$ and $\Delta d/d_o$.

Table 5. 7. Optical band gaps and its fitting parameters of the X-ray irradiation.

| | | Tauc relation $\alpha h\upsilon = A\,(h\upsilon - Eg_T)$ | | Urbach relation $\alpha = C \exp(h\upsilon/\Delta E)$ | | | |
|---|---|---|---|---|---|---|---|
| Sample | Treatment | $A$ ($cm^{-1}$) | $Eg_T$ (eV) ±0.0007 eV | $Eg_U$ (eV) ±0.0008 eV | $C \times 10^{-10}$ ($cm^{-1}$) | $\Delta E$ (meV) ±0.6 meV | RMSE |
| Pure a-Se | Unirradiated | 600839 | 2.0391 | 2.0457 | 3.1576 | 65.81 | 0.47 |
| | 30 kVp | 596204 | 2.0388 | 2.0461 | 3.0300 | 65.73 | 0.53 |
| | % change | -0.77% | -0.014% | 0.019% | -4.04% | -0.114% | |
| | Unirradiated | 616197 | 2.0396 | 2.0444 | 9.1845 | 68.11 | 0.52 |
| | 70 kVp | 609600 | 2.0393 | 2.0451 | 9.4660 | 68.20 | 0.50 |
| | % change | -1.07% | -0.019% | 0.034% | 3.07% | 0.135% | |
| a-Se 0.5% As | Unirradiated | 587180 | 2.0370 | 2.0465 | 5.3137 | 66.95 | 0.56 |
| | 30 kVp | 585704 | 2.0370 | 2.0467 | 5.1369 | 66.89 | 0.54 |
| | % change | -0.25% | 0% | 0.013% | -3.33% | -0.097% | |
| | Unirradiated | 669907 | 2.0505 | 2.0454 | 3.1075 | 65.76 | 0.42 |
| | 70 kVp | 676277 | 2.0515 | 2.0458 | 3.8863 | 66.25 | 0.42 |
| | % change | 0.95% | 0.046% | 0.016% | 25.0% | 0.74% | |
| a-Se 6% As | Unirradiated | 414232 | 2.0007 | 2.0397 | 4.74118 | 66.48 | 0.69 |
| | 30 kVp | 416577 | 2.0014 | 2.0400 | 4.30631 | 66.29 | 0.69 |
| | % change | 0.57% | 0.036% | 0.015% | -9.2% | -0.297% | |
| | Unirradiated | 382857 | 1.9966 | 2.0426 | 2.98776 | 65.59 | 0.81 |
| | 70 kVp | 383114 | 1.9967 | 2.0426 | 3.00025 | 65.60 | 0.82 |
| | % change | 0.07% | -0.0027% | 0.001% | 0.42% | 0.014% | |
| a-Se:6% As +140ppm Cs | Unirradiated | 404384 | 1.9987 | 2.03867 | 6.67759 | 67.20 | 0.67 |
| | 30 kVp | 402327 | 1.9984 | 2.03878 | 6.34201 | 67.09 | 0.68 |
| | % change | -0.51% | -0.016% | 0.005% | -5.03% | -0.164% | |
| | Unirradiated | 415977 | 2.0042 | 2.04446 | 3.28331 | 65.85 | |
| | 70 kVp | 412087 | 2.0034 | 2.04431 | 3.44727 | 65.95 | |
| | % change | -0.94% | -0.043% | -0.007% | 5.00% | 0.15% | |

From Table 5.7 above, the changes in $Eg_T$ go from –0.043% to +0.046% within experimental errors (±0.064%) and changes in $Eg_U$ go from –0.007% to +0.034% within experimental errors (±0.078%). The increase in $n$ is supposed to accompany a decrease in $Eg_T$, known as the photo-darkening effect, from Moss's rule ($E_g n^4 \sim$ constant) [59]. The decrease in band gap also was observed from Tanaka, by illuminating under band-gap light [84]. However, the change could not be detected in this case and there was no clear pattern of decrease, as oppose to a gradual change in $n$ with respect to X-rays. There were lots of fluctuations in the extracted absorption coefficient before and after irradiation.

The failure to observe photodarkening may be that the effects are too small to see the changes, when considering that the maximum percent in $d$ (or $n$) is below 0.3%. Also, it might be that the

beam spot in our spectrophotometry (i.e. around 18 $mm^2$) is not too intense to produce detectable photodarkening effects, as Tonchev reported [79]. Hence, further experiment is required to see the photodarkening effects, such as using higher intensity of X-rays (i.e. 110 kVp) and a longer exposure of X-rays to increase the delivered dose.

Table 5. 8. Wemple Di-Dominicio model parameters of X-ray irradiation.

| | | $n_{wd}{}^2 = 1 + \frac{E_0 E_d}{E_0{}^2 - (hv)^2}$ | | | |
|---|---|---|---|---|---|
| | Treatment | $n_{wd}$ (at 2000nm) | $E_o$ (eV) ±0.005 eV | $E_d$ (eV) ±0.035 eV | RMSE of fit |
| Pure a-Se | Before #1 3rd | 2.4573 | 3.75802 | 18.3902 | 1.89 |
| | After 30 kVp 4th | 2.4589 | 3.75938 | 18.4249 | 1.91 |
| | % change | 0.065% | 0.036% | 0.189% | |
| | Before #3 11th | 2.4810 | 3.775 | 18.936 | 1.78 |
| | After 70 kVp 12th | 2.4846 | 3.786 | 19.060 | 1.77 |
| | % change | 0.148% | 0.284% | 0.651% | |
| a-Se 0.5% As | Before #2 17th | 2.4482 | 3.771 | 18.324 | 1.92 |
| | After 30 kVp 18th | 2.4510 | 3.773 | 18.381 | 1.92 |
| | % change | 0.115% | 0.034% | 0.313% | |
| | Before #3 1st | 2.4675 | 3.796 | 18.802 | 1.71 |
| | After 70 kVp 2nd | 2.4719 | 3.797 | 18.885 | 1.71 |
| | % change | 0.175% | 0.022% | 0.441% | |
| a-Se 6% As | Before #3 1st | 2.4537 | 3.768 | 18.404 | 2.24 |
| | After 30 kVp 2nd | 2.4567 | 3.770 | 18.469 | 2.22 |
| | % change | 0.125% | 0.047% | 0.350% | |
| | Before 15th | 2.4600 | 3.759 | 18.469 | 2.61 |
| | After 70 kVp 16th | 2.4643 | 3.760 | 18.553 | 2.63 |
| | % change | 0.177% | 0.027% | 0.453% | |
| a-Se 6% As + 140ppm Cs | Before 17th | 2.4454 | 3.768 | 18.255 | 2.37 |
| | After 18th30kVp | 2.4484 | 3.768 | 18.310 | 2.38 |
| | % change | 0.123% | 0.002% | 0.298% | |
| | Before #2 3rd | 2.4609 | 3.771 | 18.550 | 2.52 |
| | After 70kVp 4th | 2.4675 | 3.773 | 18.678 | 2.46 |
| | % change | 0.267% | 0.041% | 0.681% | |

Table 5.8 above shows dispersion energy $E_d$ and oscillator energy $E_o$ obtained from fitting $n$ to the *Wemple DiDominicio* model. $n_{wd}$, $E_o$ and $E_d$ are all increased after irradiation, but $E_o$ increases, which is within experimental errors (±0.180%), and $E_d$ increases by 0.441– 0.681%, which is beyond experimental errors (±0.384%) for 70 kVp radiation. At 30kVp, $E_d$ increases by 0.19– 0.35% within errors. The increase in $E_d$ is also affected by X-ray doses, as same as the $n$.

From equation $E_d = \beta N_c Z_a N_e$, where $N_c$ is the effective coordination number of the cation nearest-neighbor to the anion, increase in $E_d$ is attributed to the increase of positively charged defect $N_c$ of VAP ($Se_3^+$). Since the X-ray induced charged defects of a-Se, $Se_1^-$ and $Se_3^+$, were already proven from the time of flights measurements (i.e. X-ray induced defects increased the concentration of the deep traps) [7], we expected that the increase in $E_d$ is caused by an increase in charged defects of VAP, $Se^{3+}$. In addition, from the values of $E_o$ in Table 5.9 and the $Eg_T$ in Table 5.8, it was found that $E_o = 1.9 \times Eg_{T,.}$

## 5.5 X-ray relaxation effects

This section examines whether the irradiated a-Se films return to its original states prior to irradiation. After completing 20 minutes of 70 kVp X-ray irradiation, we let the films sit at room temperature inside the spectrophotometry for two to three days and scanned the transmission spectrum from 2 hours up to 3 days after irradiation to monitor its relaxation process. The relaxation times used were: 2 hours, 3 hours, 14 hours and 3 days after X-ray irradiation. The incident air doses for 70 kVp was 44 Gy and the deposited dose in a-Se 6% As was 3132 Gy. Table 5.9 summarizes all key optical parameters before and after X-ray irradiation (The first two rows list parameters before and right after X-ray irradiation, and the rest of the rows list those for X-ray relaxation with elapsed time after completing irradiation).

Table 5. 9. Optical properties of X-ray reversibility of a-Se:6% As

| Sample a-Se:6% As | Time (min) | $\Delta d$ nm | $d$ nm | $n$ λ = 2000 nm ±0.0012 | $Eg_T$ eV ±0.0007 eV | $Eg_U$ eV ±0.0008eV | $\Delta E$ meV ±0.6 meV | $\alpha$ $cm^{-1}$ 2.05 eV |
|---|---|---|---|---|---|---|---|---|
| Virgin | 0 | 13 | 3541.2±1.6 | 2.46227 | 1.9960 | 2.0430 | 66.36 | 10422 |
| 70 kVp | 25 min | 13 | 3536.3±2.5 | 2.46570 | 1.9960 | 2.0434 | 66.41 | 10376 |
| | % change | | -0.139% | 0.139% | 0.001% | 0.019% | 0.081% | -0.44% |
| 70 kVp | 25 min | 13 | 3536.3±2.5 | 2.46570 | 1.9960 | 2.0434 | 66.41 | 10376 |
| 2hrs after | 150 min | 13 | 3536.2±2.5 | 2.46574 | 1.9959 | 2.0430 | 66.45 | 10436 |
| 3hrs after | 210 min | 13 | 3537.0±2.5 | 2.46522 | 1.9952 | 2.0431 | 66.42 | 10427 |
| 14hrs after | 850 min | 13 | 3539.5±2.5 | 2.46345 | 1.9958 | 2.0433 | 66.43 | 10400 |
| 3days after | 4080 min | 13 | 3542.5±2.5 | 2.46139 | 1.9960 | 2.0430 | 66.42 | 10430 |
| | % change | | 0.175% | -0.175% | 0.001% | -0.021% | 0.013% | 0.52% |

In Table 5.9, there is a decrease in $d$ on –0.14% with a corresponding increase in $n$ on 0.14%, upon X-ray irradiation at 70 kVp, and these $d$ and $n$ are fully recovered (0.09% and -0.09% respectively) at least 14 hours after within the margin of error (±0.09%). It implies that the X-ray

induced optical properties are reversible and suggests that there are also structural rearrangements occurring with elapsed time [54]. In Figure 5.14 where X-ray effects were plotted as a function of logarithmic time, there is a consistent and gradual return of *d* and *n* to original values. It also shows that changes in *d* and *n* are co-related according to the Claudius-Mossotti relationship, which implies that there is no change in polarizability at all.

Moreover, two optical band gaps are changed with elapsed time after X-ray irradiation. The $Eg_U$ seems to increase 0.02% upon irradiation and reverse back as relaxing, but $Eg_T$ is not reversed back. However, both optical gaps are changed only within an experimental error unlike change in refractive index and thickness. Therefore, there is no change in band-gap on relaxation, in which same case as X-ray irradiation in Section 5.4.

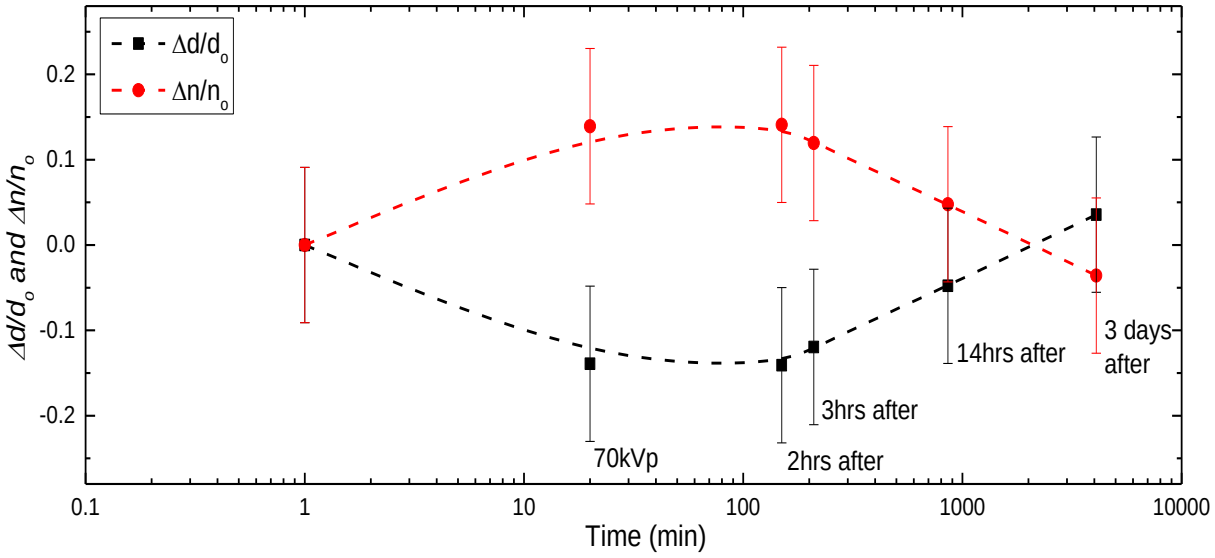


Figure 5. 14 The 70kVp irradiation and time evolution of the thickness $\Delta d/d_o$ and refractive index $\Delta n/n_o$, during and after X-ray irradiation, where $d_o$ and $n_o$ are the initial thickness and refractive index of a-Se:6% As virgin film. The 70kVp label refers to the end of irradiation (The error bars represent maximum possible error in here).

Table 5. 10. Wemple Di-Dominicio coefficients of X-ray relaxation.

$$n_{wd}{}^2 = 1 + \frac{E_0 E_d}{E_0{}^2 - (hv)^2}$$

| Sample<br>a-Se 6% As | Time | $n_{wd}$<br>(at 2000nm) | $E_o$<br>(eV)<br>±0.005 eV | $E_d$<br>(eV)<br>±0.035 eV | RMSE<br>of fit<br>(%) |
|---|---|---|---|---|---|
| Virgin | 21:00 Jan 6 | 2.4526 | 3.7615 | 18.351 | 2.45 |
| 70 kVp Irradiated | 21:25 Jan 6 | 2.4560 | 3.7623 | 18.417 | 2.47 |
| | % change | 0.139% | 0.021% | 0.360% | |
| 70 kVp Irradiated | 21:25 Jan 6 | 2.4560 | 3.7623 | 18.417 | 2.47 |
| 2hrs after | 23:30 Jan 6 | 2.4560 | 3.7623 | 18.418 | 2.48 |
| 3hrs after | 24:30 Jan 6 | 2.4555 | 3.7622 | 18.408 | 2.47 |
| 14hrs after | 11:19 Jan 7 | 2.4537 | 3.7618 | 18.374 | 2.46 |
| 3 days after | 17:14 Jan 9 | 2.4517 | 3.7613 | 18.335 | 2.47 |
| | % change | -0.175% | -0.027% | -0.445% | |

In Table 5.10, the Sellmeier dispersion relationship of refractive index was fitted in the Wemple Di-Dominicio dispersion to analyze the optical constants of $E_d$ and $E_o$ after completing X-ray irradiation. The increase in dispersion energy $E_d$ on X-ray irradiation is balanced by its decrease on X-ray relaxation. The increase in $E_d$ by 0.36% during irradiation decreases by –0.23% with relaxation. The increase in $E_d$ arises from the increase in $N_c$ of defects $Se_3^+$ upon 70 kVp irradiation from Section 5.4, and the decrease in $E_d$ is related to the decrease in $N_c$ of defects $Se_3^+$ during X-ray relaxation. So, it implies that X-ray induced defects are annealed over time as relaxing. This is agreement with Walornyj [7], in which defects creation upon X-ray irradiation is balanced by their removal from the X-ray recovery on studying electron lifetime during X-ray irradiation and recovery. Kolobov [85] also described that X-ray relaxation is a process of annihilation of defects. In addition, the oscillator energy $E_o$ is changed within experimental errors. In conclusion, the X-ray induced change in *d, n* and $E_d$ in a-Se is reversible.

# Chapter 6. Summary and Conclusion

In Section 5.1 upon heating an a-Se film (up to 6%As and with 140 ppm Cs) at $T_g$, we observed a decrease in $n$ due to the decrease in density (increase in $d$) arising from the structural expansion at the phase transition near $T_g$. The $n$ and $d$ changes could be explained by using the Clausis-Mossotti equation.

$$\frac{\Delta n}{n_o} = \frac{-(n_o^2 - 1)(n_o^2 + 2)}{(6n_o^2)} \frac{\Delta d}{d_0} \tag{6.1}$$

The observed ($\Delta d/d_o$) of 1.51 % calculates a drop of $(\Delta n/n_o)_{calc}$ of −1.72 %, which is close to the observed value ($\Delta n/n_o$) of −1.2 %, which implies that the 70% of ($\Delta n/n_o$) change can be attributed to the change in the density. The decrease in optical gap $E_{gT}$ correlates well with the decrease in the density.

It was also observed that heating results in a decrease in dispersion energy $E_d$, which can be attributed to the decrease in the effective coordination number $N_c$ of positively charged defects of $Se_3^+$ in VAP according to the relation: $E_d = \beta N_c Z_a N_e$. This change in $N_c$ was due to an increase in intermolecular distance at the phase transition near $T_g$. There was decrease in the oscillator energy $E_o$. It was found that $E_o \approx 1.89 \times Eg_T$.

It was shown in Section 5.3 that alloying with As and doping with Cs of a-Se films gave arise to an increase in $n$. The increase in $n$ by alloying with up to 6% As was due to an increase in the concentration of atoms, not polarizability, using the Clausius-Mossotti. In the case of Cs doping, however, the increase in $n$ is probably due to ionic polarizability or due to additional VAP dipoles that would be created by Cs in the structure. It was found out that the increase in $n$ from alloying and doping of a-Se also leads to the decrease in the Tauc band-gap, as expected from Moss's rule: $E_g n^4$ = constant.

In Section 5.4 and 5.5, X-ray irradiation increase leads to an increase in *n* with an increase in the density (decrease in thickness *d*) due to structural rearrangements. The changes were reversed back to the equilibrium values with relaxation over 16 hours, as a-Se films are structurally relaxing. The X-ray induced changes were affected by the deposited dose, that the x-ray induced refractive index on 70 kVp (3150 gray) was much stronger than 30 kVp (940 gray) radiation. The X-rays did not induce any changes in two the optical gaps $Eg_T$ and $Eg_U$ at all, in contrast to the gradual and clear changes in *n* and *d* beyond experimental errors. Although the changes in *n* and *d* were discernable, it turns out these changes were very small (maximum 0.27%) compared to the change induced by heating (maximum 2.2%).

The refractive index *n* was fitted into the Wemple-DiDominicio relationship to show the increase in the dispersion energy $E_d$ is related to the increase in the effective number of coordination number $N_c$ (defect creation) and to show the decrease in $E_d$ is related to the decrease in $N_c$ upon X-ray relaxation (defect annihilation). The defect creation and annihilation due to X-rays were in agreement with the experiments done by interrupted field time of flights measurements. The relationship between $E_o$ and $Eg_T$ was found out to be $E_o = 1.9 \times Eg_T$.

Table 6. 1. Summary of optical properties for a-Se films.

| Description | Sec | *d* (nm) | *n* (at $\lambda$ = 2000nm) | $Eg_T$ (eV) | $Eg_U$ (eV) |
|---|---|---|---|---|---|
| Heating to $T_g$ | 5.1 | increase | decrease | decrease | decrease |
| Increased thickness | 5.2 | n/a | -- | -- | -- |
| Alloying As | 5.3 | n/a | increase | decrease | decrease |
| Doping Cs | 5.3 | n/a | increase | decrease | decrease |
| X-ray irradiation | 5.4 | decrease | increase | no change | -- |
| X-ray relaxation | 5.5 | increase | decrease | no change | -- |

# References

[1] G. J. Bansal, “Review: Digital radiography: A comparison with modern conventional imaging”, Postgraduate Medical Journal, Vol 82, Issue 969, pp 425–428, 2006.

[2] M. Körner, C. H. Weber, S. Wirth, K. J. Pfeifer, M. F. Reiser, and M. Treitl, *Advances in Digital Radiography: Physical Principles and System Overview*, RadioGraphics Education Exhibit., Vol 27, Issue 3, pp 675 – 686, 2007.

[3] S.O. Kasap and J.A. Rowlands, “Direct-conversion flat-panel X-ray image detectors”, IEE Proceedings - Circuits, Devices and Systems, Vol 149, No 2, pp 85-96, April 2002.

[4] S.O. Kasap, M. Z. Kabir, J.A. Rowlands, “Recent advances in X-ray photoconductors for direct conversion X-ray image detectors”, In Current Applied Physics, Volume 6, Issue 3, pp 288-292, 2006.

[5] M. Spahn, “Flat detectors and their clinical applications”, European Radiology, Vol 15, Issue 9, pp 1934–1947, 2005.

[6] L. Bakueva, A. W. Rau, J. A. Rowlands and A. Shik, “X-ray-induced ghosting in amorphous selenium”, Journal of Physics D: Applied Physics, Vol 39, No 3, pp. 441- 448, January 2006.

[7] M. Walornyj and S. O. Kasap, “X-ray irradiation induced changes in electron transport in stabilized a-Se photoconductors”, Journal of Applied Physics, Vol 114, Issue 21, pp. 214505, 2013.

[8] S.O. Kasap and J.A. Rowlands, “Review: X-ray photoconductors and stabilized a-Se for direct conversion digital flat-panel x-ray image-detectors”. Journal of Materials Science: Materials in Electronics, Vol 11, Issue 3, pp 179–198, April 2000.

[9] P. Sprawls, "X-Ray Image Formation and Contrast", *The Physical Principles of Medical Imaging*, Medical Physics Publishing, 1995, Second edition, http://www.sprawls.org/ppmi2/XRAYCON/ (Accessed at Dec 2016).

[10] P. Sprawls, "X-ray Production", *The Physical Principles of Medical Imaging*, Medical Physics Publishing, 1995, Second edition, http://www.sprawls.org/ppmi2/XRAYPRO/ (Accessed at Dec 2016).

[11] A.C. Carl and A.C. Gudrun. *Basic physics of X-ray imaging*. Department of Medicine and Care Radio Physics, Faculty of Health Science, 2017.

[12] J.A. Seibert, "Digital radiography: The bottom line comparison of CR and DR technology", Applied Radiology, pp. 21- 28, 2009.

[13] B. J. Fogal, *Electronic Transport Properties of Stabilized Amorphous Selenium X-ray Photoconductors*, MSc thesis, University of Saskatchewan, 2005.

[14] L. Lanca and A. Silva, "Chapter 2: Digital Radiography Detectors: A Technical Overview" in *Digital Imaging Systems for Plain Radiography*, 2013, Springer New York.

[15] G. S. Ristić, "The digital flat-panel X-ray detectors", Proceedings of the third conference on medical physics and biomedical engineering, Association for medical physics and biomedical engineering in cooperation with the European federation of organisations for medical physics, page 65- 71, 2013 October.

[16] V. F. Andolina, S. Lile, *Mammographic imaging: A practical guide*, third edition, Philadelphia, Penn.: Wolters Kluwer/Lippincott Williams & Wilkins Health, c2011.

[17] S.O. Kasap, "X-ray sensitivity of photoconductors: application to stabilized a-Se", Journal of physics D: Applied physics, Vol 33, No 21, pp 2853–2865, 2000.

[18] V. I. Mikla and V. V. Mikla, *Amorphous Chalcogenides: The Past, Present, and Future*, Elsevier Inc. 2011.

[19] G. K. Ahluwalia, *Applications of Chalcogenides: S, Se, and T*e, Springer International Publishing, November 2016.

[20] J. Rowlands and S. O. Kasap, “Amorphous semiconductors usher in digital x-ray imaging”, Physics Today, pp 24- 30, 1997.

[21] M. A. Popescu, *Non-Crystalline Chalcogenides*, Solid state science and technology library, Kluwer Academic Publishers, 2006.

[22] Y. Sakaguchi and K. J. Tamura “Photodarkening process in amorphous chalcogenide; Measurements of transient photo-induced optical absorption”, Journal of Materials Science: Materials in Electronics, Vol 18, Supplement 1, pp 459–462, October 2007.

[23] F. Djefaflia, C. Mebarkia, A. Hafdallah, M.L. Benkhedir, A. Belfedal, “Photoinduced changes in amorphous selenium”, Canadian Journal of Physics, Vol 92, pp 663-666, 2014.

[24] J. Teteris, “Holographic recording in amorphous chalcogenide thin films, Current Opinion in Solid State and Materials Science”, Vol 7, Issue 2, pp 127–134, April 2003.

[25] C. Juhasz and V. Gembala, “Growth characteristics of vacuum coated thick a-Se films for device applications”, Journal of Vacuum Science & Technology A: Vacuum, Surfaces, and Films, Vol 18, 665, 2000.

[32] S. O. Kasap, *Principles of Electronic Materials and Devices*, McGraw-Hill Inc, Third Edition, 2006.

[33] W. H. Zachariasen, “The Atomic Arrangement in Glass”, Journal of the American Chemical Society, Vol 54, (10), pp 3841–3851, 1932.

[34] J. A. Woollam, K. R. Morasb, M. Kzlninsky, and B. L. Averbach, “Photoconductive and Optical Properties of Amorphous Selenium”, Lewis research center, National Aeronautics and Space Administration (NASA), Washington, D.C., 1971.

[35] T. Merdzhanova, “Chapter 2”, *Microcrystalline Silicon Films and Solar Cells Investigated by Photoluminescence*, Forschungszentrums Jülich in der Helmholtz-Gemeinschaft, Vol 41, 2005.

[36] M. L. Benkhedir, *Defect Levels in the Amorphous Selenium Bandgap*, PhD thesis, Katholieke Universiteit Leuven, 2006.

[37] K. Koughia, Z. Shakoor, S. O. Kasap, and J. M. Marshall, "Density of localized electronic states in a-Se from electron time-of-flight photocurrent measurements", Journal of Applied Physics, 97, 033706, 2005.

[38] C.K. Wong, G. Lucovsky, J. Bernholc, "Intrinsic localized defect states in a-Se associated with dihedral angle distortions", Journal of Non-Crystalline Solids, Vol 97–98, Part 2, pp. 1171-1174, 1987.

[39] G. Lucovsky and F. L. Galeener, "Intermediate ranger order in amorphous solids", Journal of Non-Crystalline Solids, Vol 35-36, part 2, pp. 1209- 1214, 1980.

[40] M. Kastner, D. Adler, H. Fritzsche, "Valence-Alternation Model for Localized Gap States in Lone-Pair Semiconductors", Physical Review Letters, Vol 37, No 22, pp. 1504- 1507, 1976.

[41] B.W. Corb, W.D. Wei and B.L. Averbach, "Atomic models of amorphous selenium", Journal of Non-Crystalline Solids, Vol 53, Issue 1-2, pp. 29-42, 1982.

[42] C. Koughia, A. Reznik, C. Allen, R. Johanson, and S. Kasap, "Density of localized state distribution near the valence band in stabilized a-Se using interrupted field time of flight measurements with long interruption times", Physica Status Solidi A, Vol 213, Issue 7, pp. 1856-1863, 2016.

[43] W. C. Tan, *Optical Properties of Amorphous Selenium Films*, MSc thesis, University of Saskatchewan, July 2006.

[44] M. Abkowitz and R. C. Enck, "Xerographic spectroscopy of gap states in amorphous semiconductors", Physical Review B, Vol 25, No 4, pp. 2567 – 2577, 1982.

[45] J. Berashevich, A. Mishchenko, and A. Reznik, "The two-step photoexcitation mechanism in amorphous Se", Physical Review Applied, Vol 1, Issue 3, pp. 34008, 2014.

[46] R. Swanepoel, "Determination of the thickness and optical constants of amorphous silicon", Journal of Physics E: Scientific Instruments, Vol 16, 1983, pp. 1214 – 1222.

[47] R. swanepoel, “Determination of surface roughness and optical constants of inhomogeneous amorphous silicon films”, Journal of Physics E: Scientific Instruments, Vol 17, 1984, pp. 896 – 903.

[48] S. Ahmad and M. Mohib-ul Haq, “A study of energy gap, refractive index and electronic polarizability of ternary chalcopyrite semiconductors”, Iranian Journal of Physics Research, Vol 14, No 3, pp. 89-93, 2014.

[49] M. H. Saleh, M. M. Abdul-Gader Jafar, B. N. Bulos, and T. M. F. Al-Daraghmeh, “Determination of Optical Properties of Undoped Amorphous Selenium (a-Se) Films by Dielectric Modeling of Their Normal-Incidence Transmittance Spectra”, Applied Physics Research, Vol 6, No 6, 2014, pp. 10- 44.

[50] S. Kugler and K. Shimakawa, *Amorphous Semiconductors*, Cambridge University Press, United Kingdom, 2015.

[51] S. Kasap, C. Koughia, J. Singh, H. Ruda, and S. O’ Leary, “Chapter 3: Optical properties of electronic materials: Fundamentals and characterization”, *Springer handbook of electronic and photonic materials*, edited by S. Kasap and P. Capper, springer US, 2007.

[52] M. Nessa, K. Shimakawa, A. Ganjoo, and J. Singh. “Fundamental optical absorption on fractals: A case example for amorphous chalcogenides*”*, Journal of Optoelectronics and Advanced Materials, Vol 2, No 2, pp. 133-138, June 2000.

[53] N.F. Mott and E.A. Davis, *Electronic processes in non-crystalline materials*, second edition, Oxford: clarendon press, p 272, 1905.

[54] K. Tanaka and K. Shimakawa, *Amorphous chalcogenide semiconductors and related materials*, Springer New York Dordrecht Heidelberg London, 2011.

[55] L. Tichy, H. Ticha, P. Nagels, E. Sleeckx and R. Callaerts, “Optical gap and Urbach edge slope in a-Se”, Materials Letters, Vol 26, Issue 6, pp. 279-283, 1996.

[56] K. Tanaka, T. Gotoh, N. Yoshida, S. Nonomura, “Photothermal deflection spectroscopy of chalcogenide glasses”, Journal of Applied Physics, Vol 91, pp. 125, 2002.

[57] J.M.González -Leal, Mir.Vlček, R.Prieto-Alcón, A.Stronski, T.Wágner, E.Márquez, "Thermal relaxation of the structural and optical properties of amorphous AsSSe films", Journal of Non-crystalline solids, Vol 326 & 327, 2003, pp. 146 – 153.

[58] Y.H. Jung, O. Güneş, G. Belev, C. Koughia, R. Johanson, S. Kasap, "X-ray induced effects in the optical and thermal properties of a-Se1−xAsx (x = 0, 0.005, 0.06) doped with 0–220 ppm Cs", Journal of Materials Science: Materials in Electronics, Vol 28, Issue 10, pp 7139–7150, 2017.

[59] T. S. Moss, "Relation between the refractive index and energy gap of semiconductors" Physica Status Solidi B, 131, pp. 415-427, 1985.

[60] P. Hervé and L. K. J. Vandamme, "General relation between refractive index and energy gap in semiconductors", Infrared Physics and Technology, Vol 35, Issue 4, pp. 609-615, 1994.

[61] OJL interband transition model for amorphous materials - a brief tutorial, Optical transitions in amorphous materials. http://www.mtheiss.com/ojl_optr.htm (Accessed at Dec 2016).

[62] D. Dorrania n, L. Dejam and G. Mosayebian, "Optical characterization of $Cu_3N$ thin film with Swanepoel method", Journal of Theoretical and Applied Physics, Vol 6, Issue 13, pp. 1-9, 2012.

[63] S. O. Kasap, "Chapter 1: Wave nature of light", *Optoelectronics and Photonics: principles and practices*, Second edition, Pearson Education, 2013.

[64] D. Poelman and P. F. Smet, "Methods for the determination of the optical constants of thin films from single transmission measurements: a critical review", Journal of Physics D: Applied Physics, Vol 36, No 15, pp, 1850-1857, 2003.

[65] P. Nagels, E. Sleeckx, R. Callaerts, E. Márquez, J.M. González, A.M. Bernal-Oliva, "Optical properties of amorphous Se films prepared by PECVD", In Solid State Communications, Vol 102, Issue 7, pp. 539-543, 1997.

[66] J. Yang, *X-ray Induced Changes in Electronic Properties of Stabilized Amorphous Selenium Based Photoconductors*, MSc, University of Saskatchewan, 2016.

[67] P. Sprawls Jr, "Interaction of radiation with matter", *The Physical Principles of Medical Imaging*, Medical Physics Publishing, 1995, Second edition, http://www.sprawls.org/ppmi2/INTERACT/ (Accessed at Dec 2016).

[68] https://www.oem-xray-components.siemens.com/x-ray-spectra-simulation (Accessed Jan 2017).

[69] P. Sprawls Jr, "Radiation quantities and units", *The Physical Principles of Medical Imaging*, Medical Physics Publishing, 1995, Second edition. http://www.sprawls.org/ppmi2/RADQU/ (Accessed at Dec 2016).

[70] http://physics.nist.gov/PhysRefData/XrayMassCoef/ElemTab/z34.html (Accessed Jan 2017)

[71] Instrumental specification for Lambda 900.

[72] G. Okada, *Development of a Large-Dose, High-Resolution Dosimetry Technique for Microbeam Radiation Therapy using Samarium-Doped Glasses and Glass-Ceramics*, PhD thesis, University of Saskatchewan, 2014.

[73] M. I. Ojovan, "Configurons: Thermodynamic Parameters and Symmetry Changes at Glass Transition", Entropy, Vol 10, Issue 3, pp 334-364, 2008.

[74] S.O. Kasap, "Photoreceptors: The Chalcogenides", Chapter 9 in *The Handbook of Imaging Material: Second Edition Revised and Expanded*, edited by Arthur S. Diamond and David S. Weiss, Marcel Dekker Inc., New York, pp. 343-346, 2002.

[75] R.K. Kirby and B.D. Rothrock, "Thermal expansion of vitreous selenium from -190 to 30° C", Journal of the American Ceramic Society- Discussion and notes, pp 535, 1968.

[76] E.R. Shaaban, "Calculation of the optical constants of amorphous semiconducting As40S60, As40S35Se25 and As40Se60 thin films from transmittance and reflectance measurements". Journal of Applied sciences, Vol 6, Issue 2, pp 340 – 346, 2006.

[77] J. Pétursson, J. M. Marshall and A. E. Owen, "Optical absorption in As-Se glasses", Philosophical Magazine B, Vol 63, Issue 1, pp 15-31, 1991.

[78] Z.U. Borisova, *Glasses in Binary Systems. In: Glassy Semiconductors*, pp 38-39, Springer, Boston, MA, 1981.

[79] A. C. van Popta, R. G. DeCorby, C. J. Haugen, T. Robinson, J. N. McMullin, D. Tonchev, and S. O. Kasap, "Photoinduced refractive index change in $As_2Se_3$ by 633nm illumination", Optics Express., Vol 10, Issue 15, pp 639-644, 2002.

[80] P. Bhardwaj, P. K. Shishodia, R. M. Mehra, "Photo-induced changes in optical properties of As2S3 and As2Se3 films deposited at normal and oblique incidence", Journal of Materials Science, Vol 38, Issue 5, pp 937–940, March 2003.

[81] W. C. Tan, G. Belev, K. Koughia, R. Johanson, S. K. O'Leary, S. Kasap, "Optical properties vacuum deposited and chlorine doped a-Se thin films: aging effects", Journal of materials science: Materials electronics, Vol 18, pp. S429–S433, 2007.

[82] A.V. Kolobov, H. Oyanagi, K. Tanaka, Ke Tanaka. "An in situ EXAFS study of amorphous selenium: The formation of dynamical bonds under light excitation", Journal of Luminescence, Vol 66 and 67, pp 174-178, 1995.

[83] A.V. Kolobov, M. Kondo, H. Oyanagi, R. Durny, A. Matsuda, K. Tanaka, "Experimental evidence for negative correlation energy and valence alternation in amorphous selenium", Physical review B, Vol 56, No 2, pp. R485 -R488, 1997.

[84] K. Tanaka and A. Odajima, "Photo darkening in amorphous selenium", Solid State Communications, Vol 43, No 12, pp. 961-964, 1982.

[85] A. V. Kolobov, *photo-induced metastability in amorphous semiconductors*, John Wiley & Sons, 2006.

[86] M. L. Trunov, P. M. Lytvyn, S. N. Yannopoulos, I. A. Szabo, and S. Kokenyesi, "Photoinduced mass-transport based holographic recording of surface relief gratings in amorphous selenium films", Applied Physics Letters, Vol 99, pp.51906, 2011.